Electron wave and quantum optics in graphene

Himadri Chakraborti, Cosimo Gorini, Angelika Knothe, Ming-Hao Liu, Péter Makk, François Parmentier, David Perconte, Klaus Richter, Preden Roulleau, Benjamin Sacépé, et al.

TOPICAL REVIEW • OPEN ACCESS

Electron wave and quantum optics in graphene

OPEN ACCESS
IOP Publishing
Journal of Physics: Condensed Matter
J. Phys.: Condens. Matter **36** (2024) 393001 (60pp)
https://doi.org/10.1088/1361-648X/ad46bc

Topical Review

Electron wave and quantum optics in graphene

Himadri Chakraborti[1], Cosimo Gorini[1], Angelika Knothe[2,*], Ming-Hao Liu[3], Péter Makk[4,5,*], François D Parmentier[1], David Perconte[6], Klaus Richter[2], Preden Roulleau[1,*], Benjamin Sacépé[6], Christian Schönenberger[7] and Wenmin Yang[6]

[1] Université Paris-Saclay, CEA, CNRS, SPEC, 91191 Gif-sur-Yvette, France
[2] Institut für Theoretische Physik, Universität Regensburg, D-93040 Regensburg, Germany
[3] Department of Physics and Center for Quantum Frontiers of Research and Technology (QFort), National Cheng Kung University, Tainan 70101, Taiwan
[4] Department of Physics, Institute of Physics, Budapest University of Technology and Economics, Műegyetem rkp. 3., Budapest H-1111, Hungary
[5] MTA-BME Correlated van der Waals Structures Momentum Research Group, Műegyetem rkp. 3., Budapest H-1111, Hungary
[6] Université Grenoble Alpes, CNRS, Grenoble INP, Institut Néel, 38000 Grenoble, France
[7] Nanoelectronics Group, Department of Physics, University of Basel, Basel, Switzerland

E-mail: angelika.knothe@physik.uni-regensburg.de, makk.peter@ttk.bme.hu and preden.roulleau@cea.fr

Received 4 November 2023, revised 24 February 2024
Accepted for publication 1 May 2024
Published 1 July 2024

Abstract

In the last decade, graphene has become an exciting platform for electron optical experiments, in some aspects superior to conventional two-dimensional electron gases (2DEGs). A major advantage, besides the ultra-large mobilities, is the fine control over the electrostatics, which gives the possibility of realising gap-less and compact p-n interfaces with high precision. The latter host non-trivial states, *e.g.* , snake states in moderate magnetic fields, and serve as building blocks of complex electron interferometers. Thanks to the Dirac spectrum and its non-trivial Berry phase, the internal (valley and sublattice) degrees of freedom, and the possibility to tailor the band structure using proximity effects, such interferometers open up a completely new playground based on novel device architectures. In this review, we introduce the theoretical background of graphene electron optics, fabrication methods used to realise electron-optical devices, and techniques for corresponding numerical simulations. Based on this, we give a comprehensive review of ballistic transport experiments and simple building blocks of electron optical devices both in single and bilayer graphene, highlighting the novel physics that is brought in compared to conventional 2DEGs. After describing the different magnetic field

* Authors to whom any correspondence should be addressed.

regimes in graphene p-n junctions and nanostructures, we conclude by discussing the state of the art in graphene-based Mach–Zender and Fabry–Perot interferometers.

Keywords: electron optics, graphene, quantum hall interferometer, magnetic focusing, p-n junctions, snake states

Contents

List of acronyms

1(2)D	One(two) dimensional
2DEG	Two dimensional electron gas
BZ	Brillouin zone
SQUID	Superconducting quantum interference device
ODE	Ordinary differential equation
PDE	Partial differential equation
SEM	Scanning electron microscope
AFM	Atomic force microscope
TEM	Transmission electron microscope
STM	Scanning tunnelling microscope
SET	Single electron transistor
SGM	Scanning gate microscope

TEF	Transverse electron focusing
h-BN	Hexagonal boron nitride
Gr	Graphene (usually monolayer)
BLG	Bilayer graphene
LOR	Lift off resist
PDMS	Polydiméthylsiloxane
PC	Polycarbonate (polymer)
PPC	Polypropylene carbonate (polymer)
CNP	Charge neutrality point of graphene
SdH	Shubnikov de Haas
WGM	Whispering gallery mode
TG	Top gate
BG	Back gate
p-n junction	Interface between positively (p) and negatively (n) charged graphene regions
FP(I)	Fabry-Pérot (Interferometer)
MZ(I)	Mach Zehnder (Interferometer)
QPC	Quantum point contact
AB	Aharonov Bohm
QH	Quantum Hall
FT	Fourier transform

1. Preface

1.1. Electron quantum optics; why graphene?

Since its discovery [1], graphene has emerged as a wonder material and as a playground of different fascinating condensed matter physics ideas. Due to its high electrical and thermal conductivity that comes together with an almost 100% optical transparency for the visible optical spectrum, monolayer and bilayer graphene, as well as the recently discovered twisted bilayer and multilayer graphene [2], are promising materials for various application areas including advanced electronics and novel solutions for sustainability. Advancement of nanofabrication techniques over the past twenty years led to the realization of several interesting concepts stemming from the linear energy-momentum relation near the Fermi energy of undoped graphene, where the two-dimensional Fermi surface shrinks to two Fermi points, known as Dirac points. The two separate Fermi surfaces are termed valleys (the K and K' points) and for low-energy, each valley hosts mass-less quasi-particles that are alike relativistic Dirac/Weyl fermions.

Electron quantum optics is a field of research where the focus is on the wave nature of electrons in solids. The goal is to explore fundamental properties of fermionic quasi-particles in solids by conducting prototypical experiments known from optics. A typical traditional free space quantum optics experiment is an interference experiment that converts the quantum nature into a measurable intensity pattern as a function of a control parameter. Examples are the text-book two-slit interference experiment, Fabry–Pérot, Mach–Zehnder and Michelson interferometers, and intensity-correlation experiments along the line of Hanbury-Brown and Twist [3, 4]. These experiments make use of the large velocity of photons given by the speed of light which transforms even a rather short temporal coherence of a light source of 1 ns into an appreciable coherence length of 0.3 m. Taking a laser source, some light apertures and mirrors, it is straightforward to construct such interference experiments on an optical table.

In a solid state, electrons move at much lower speeds. The velocity is an interesting parameter as it can be dressed by all interactions: it is usually enhanced by strong electron-electron repulsion, but it can also be lowered through strong coupling with lattice degrees of freedom, such as phonons. For a typical doping, the group velocity of quasi-particles in semiconductors is only of order $10^5\,\mathrm{m\,s^{-1}}$. Noting that relaxation times through electron-phonon interaction can easily be as short as 1 ps, one finds an electron mean-free path l_{mfp} of only $\approx 100\,\mathrm{nm}$. Hence, it seems impossible to perform free electron propagation (ballistic) electron optics experiments. First, one has to cool the solid state material to low enough temperatures that relaxation through the lattice is sufficiently suppressed. In the second place, one has to work with materials of very high quality, since also inherent disorder, such as atomic defects and grain boundaries, limit the mobility, and, hence, l_{mfp}. Electron optics experiments become feasible when the ballistic mean-free path l_{mfp} is larger or comparable to system sizes that can be patterned with current state-of-the-art micro and nano-fabrication technology. So samples are of size $L > 0.1\ \mu$m, and typically in the range of $L \simeq 1 - 10\ \mu$m.

A second requirement is that the de Broglie wavelength λ of the electrons (or holes) in the solid-state material should be $\lambda \ll l_{\mathrm{mfp}}$. This is the limit of quasi-classical quantum optics, where propagation along optical trajectories can be defined and engineered through smooth electrostatic profiles. Moreover, beyond conventional optical properties of light rays, trajectories of Dirac charge carriers can be additionally bent and controlled through magnetic fields, a hallmark and unique stronghold of Dirac electron quantum optics. We note here that the notion of quasi-classical electron propagation looses its meaning in the opposite limit $\lambda \simeq L$. Here, localized confined states appear, which are realized in quantum dots and cavities. Such structures will also be covered in this review.

The field for electron quantum optics widened to a great extent when graphene devices could be fabricated with high enough purity yielding large enough ballistic mean-free paths l_{mfp}. The large Fermi velocity of graphene of $v \simeq 10^6\,\mathrm{m\,s^{-1}}$ helped to move on from disordered graphene ribbons to graphene that is ballistic over macroscopic distances. Moreover the electric field controllable ambipolar nature of graphene [1] provides a pristine way to control the global carrier density over the ion-implantation method of doping in conventional semiconductors. Realization of junctions of opposite carrier densities (electron and hole-type) in a single graphene sheet through the local control of carrier density using electrostatic gates is a milestone in electron quantum optics in general [5–8]. The ability of fabricating p-n junctions gave rise to 'relativistic' condensed matter physics where relativistic quantum phenomena like Klein

tunneling [9], Veselago lensing [10], particle collimation [11], and quasibound states [12] were demonstrated on chip-size devices.

1.2. Traditional quantum optics in a 2DEG

Two-dimensional electron gases (2DEGs) confined in a GaAs quantum well in heterostructures of AlGaAs/GaAs-based semiconductors [13] have been the historically dominant material in which electron quantum optics experiments could be realized. This is due to various factors: among the technical ones, the use of microelectronics industry growth and processing techniques has allowed obtaining high quality 2DEGs on wafer scale, that can be electrically connected using highly transparent ohmic contacts [14]. Due to the low mass of the electrons in the conduction band, very high mobilities have been achieved [15]. Record electron mobilities are $\mu > 50 \cdot 10^6$ cm^2 (Vs)$^{-1}$ yielding macroscopic mean-free paths $l_{\mathrm{mfp}} > 250$ μm. Perhaps even more importantly, the semiconducting nature of AlGaAs/GaAs heterostructures permits the use of electrostatic depletion gates with which one can shape the potential landscape in the 2DEG. Thereby, one can gain control over electron wave trajectories. The most commonly used gating structure in electron quantum optics experiments with GaAs quantum wells is a split gate realising a quantum point contact (QPC) [16]: a saddle point-like constriction in the 2DEG through which the electrons are channeled.

For electron-transport experiments at low temperature, which are the focus in this review, only electrons (or holes) at low energies are considered. According to the de Broglie relation and parabolic energy dispersion of quasi-free electrons with mass m_e, the Fermi wavelength $\lambda_{\mathrm{F}} = h/\sqrt{2m_eE_{\mathrm{F}}}$, where E_{F} is the Fermi energy and h the Planck constant. For a low effective mass and Fermi energy, the Fermi wavelength can become large, reaching values $\lambda_{\mathrm{F}} > 100$ nm. Since structure on the 100 nm scale can easily be fabricated today, QPCs can be designed that can electrostatically be tuned to pass none, only one, or a few (transverse) channels through the constriction. This has led to the seminal work of quantized conductance in QPCs, first conducted by van Wees *et al* [16].

The most elementary electron optics experiment could start with a QPC that is tuned to transmit exactly one single channel. If the channel opens adiabatically on the exit side, a spherical electron wave would emerge. One could then place a gate electrode in the shape of a half circle some distance behind the QPC and applying a strongly negative voltage so that the gate acts as a mirror for electrons. If the mirror is smooth enough, it would reflect the electrons back to the QPC. Due to the wave nature, this arrangement will give rise to so-called Fabry-Pérot interferences, which, depending on the wavelength and the distance from the QPC to the mirror, can be constructive or destructive. This interference pattern can be made visible in three ways: (i) by changing the Fermi energy of the 2DEG with e.g. a global gate, (ii) by tuning the voltage that is applied over the QPC, or (iii) by changing the magnetic field. In case (i), one would measure the linear-response electrical conductance at small bias voltage as a function of gate voltage, and in case (ii), one would measure the differential conductance as a function of bias voltage. The (iii) way is by applying a tunable magnetic field B, which is also a very important tuning knob in quantum-interference experiment, and it will very often show up in this review.

1.3. Graphene for quantum electron optics

In recent years graphene devices with amazing qualities could be obtained, either by current-annealing suspended graphene [17, 18] or by encapsulation into single-crystalline hexagonal boron nitride (h-BN) [19–21] complemented with one-dimensional (1D) edge contacts [21] which improved the electronic performance of graphene-based devices drastically, as explained in detail in section 3. All these developments led to two-dimensional (2D) gate-tunable electrical conductors with mobilities that typically reach values $\mu_e > 10^5$ cm^2 (Vs)$^{-1}$, in some cases even above 10^6 cm^2 (Vs)$^{-1}$. Correspondingly, large mean-free paths l_{mfp} exceeding 1 μm could be established and ballistic transport became possible in samples of 'mesoscopic', and even macroscopic size [17, 18, 22–24]. If in addition the coherence length is sufficiently long, which requires low bias and low temperature experiments, quantum interference starts to play a decisive role. In graphene devices, all kind of quantum coherent interference effects have been observed in a surprisingly clean fashion.

Three generic electron-optical device concepts that very often appear in the literature are introduced in figure 1.

In a perpendicular magnetic field B the quantum effects are very different for zero, small, intermediate and large fields. For very small fields, the magnetic field adds a weak Lorentz force which bends semiclassical trajectories slightly [25]. This adds a small phase term in quantum interference as a correction to the zero-field case. Nonetheless, this has interesting consequences. At intermediate fields the bending can become significant, leading to the formation of new bounds states within a finite size graphene device [26]. If the magnetic field increases beyond a critical value B_c for which the cyclotron radius due to the ballistic motion shrinks below the sample size L, edges-states form at the boundary of the samples [27]. They can often still be treated in a semiclassical manner as so-called skipping orbits and they are crucial to understand transport in devices where p-n junctions are realized. But if the magnetic field is so large that Landau quantization becomes dominant, this is when the bulk of the sample becomes gapped, one is entering the quantum Hall regime [28, 29]. While the interior of the sample is gapped in the quantum Hall state, compressible conducting channels form along the edges of the crystal. These channels are known as edges states. In the integer quantum Hall regime the edge channels are chiral and the number of channels depends on the filling factor $\nu = nh/eB$ which depends on carrier density n and magnetic field strength B.

The edge channels of the quantum Hall state form ideal channels, since backscattering is absent in wide enough

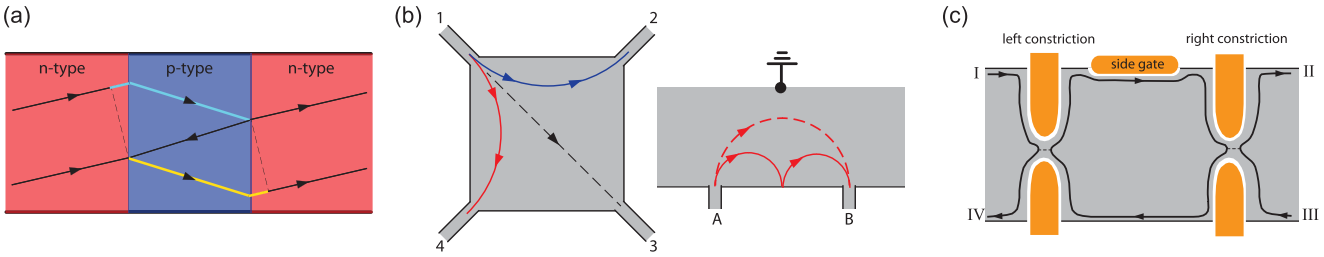

Figure 1. Examples of electron optical devices. (a) shows a *Fabry-Pérot interferometer* where the 'mirrors' are defined by the boundaries between two regions with different electron concentrations. Specific to graphene, the two regions can also have opposite doping, indicated here in red as n-type and in blue as p-type. In this bipolar case, electron refraction is negative at the interface, which is something quite peculiar. Constructive interference occurs when the phase acquired along the blue or yellow path is a multiple of 2π. The phase can be controlled through gates that tune the electron concentrations in, for example, the middle region. (b) shows another interesting device concept which is based on *transverse magnetic focusing*. The Lorentz force due to a magnetic field applied perpendicular to the graphene plane deflects the electron trajectories. In the red case, the electrons are deflected from the source contact 1 into drain contact 2. Changing either the direction of the magnetic field or the sign of the charge carrier type, flips the orientation of the circular motion from the red to the blue case. The right figure in (b) shows transverse magnetic focusing along one sample edge. The resonance condition for scattering from source contact A into drain contact B can be obtained for different strengths of magnetic fields. Finally, (c) shows a *quantum Hall interferometer* that makes use of edge states (dark black lines with arrows indicating propagation direction). One can measure, for example, the transmission probability from contact I to contact II or the reflection probability to IV. The edge state can be seen as a one-dimensional propagating electron wave that is scattered with some probabilities at the left and right constrictions. With the aid of the side gate in the interior region the path length can be adjusted resulting in Aharonov–Bohm oscillation in the measurements.

samples. The transport channels can be seen as analogs to single- or few-mode optical fibres. They are ballistic over lengths reaching the millimeter scale. In GaAs quantum wells they became the tool to explore a very large number of electron quantum optics experiments, such as Aharonov–Bohm oscillation in a ring [30], electronic quantum interferometers in Fabry-Pérot [31] and Mach–Zehnder [32] geometries, the realization of on-demand single electron sources [33, 34], Hanbury-Brown and Twiss correlations measurements in continuous [35–37] and single-excitations [38] electron beams, or Hong-Ou Mandel two-particle interferences [39]. Lately, the ability to combine these electron quantum optics schemes with the fractionally charged anyonic excitations of the fractional quantum Hall effect has further expanded the field [40, 41] with the perspective of developing yet another quantum information processing platform relying on non-abelian statistics [42]. A quantum Hall edge channel can be selectively transmitted with a probability between zero and unity, fully gate-tunable. As the edge channels form the electronic analogue of fiber optics, QPCs are the electronic equivalent of tunable beam-splitters, and are therefore ubiquitous in electron quantum optics experiments realized in AlGaAs/GaAs 2DEGs [43].

Transferring electron quantum optics experiments from GaAs 2DEGs to graphene has become an important task in the field in the past decade, as the quality and mobility of the available graphene samples increased dramatically. Indeed, the honeycomb lattice of graphene and its semi-metallic band structure give rise to extremely rich quantum Hall effects [44], which can be explored through electron quantum optics experiments. In particular, the ambipolarity of graphene, as well as the strong role of electronic interactions in the emergence of quantum Hall ferromagnetism where both spin and valley symmetries are broken [45–48], greatly expands the playground for electron quantum optics. Furthermore, the structural differences between AlGaAs/GaAs 2DEGs and graphene, particularly with respect to the electronic confinement at the edge of the sample, allows testing the hypotheses upon which our current understanding of edge channel transport is based.

Similar to monolayer graphene, electron quantum optics experiments were early on also conducted with bilayer graphene. In contrast to monolayer graphene, bilayer graphene has additionally to the valley degree also a layer degree of freedom. The layer degree can directly be accessed through the charge density in the two layers using a double gated stack, which today typically starts with a graphite bottom gate, followed by a h-BN gate dielectric, bilayer graphene, followed by the top h-BN gate dielectrics, and ending by a top graphite gate. A symmetric gate voltage will add the same amount of charge to the two layers. However, if gating is asymmetric one can induced opposite charge in the two layers. This gives rise to a so-called displacement field, which—crucially—opens a gap in bilayer graphene. In gapped bilayer graphene one can realize the exact analogue of the QPC that was/is used in GaAs quantum well structures. Gating allows to fully deplete a region. This has also allowed to define gate controlled channels where the channel width is not determined by the natural graphene edges or by etched edges, but rather by a smooth bounding potential defined by the global gate structure [49–52]. This has been an important milestone, since it allowed to engineer ballistic few-mode channels without a magnetic field, simply due to the presence of the gap in bilayer graphene with non-zero displacement field. In earlier etched graphene ribbons the edge roughness was too large and strongly limited to scattering mean-free path.

Finally, note that most of the physics discussed here is observed at cryogenic temperatures. In these conditions, lattice phonons become decoupled from the charge carriers, as exemplified by the fact that thermal conduction in graphene

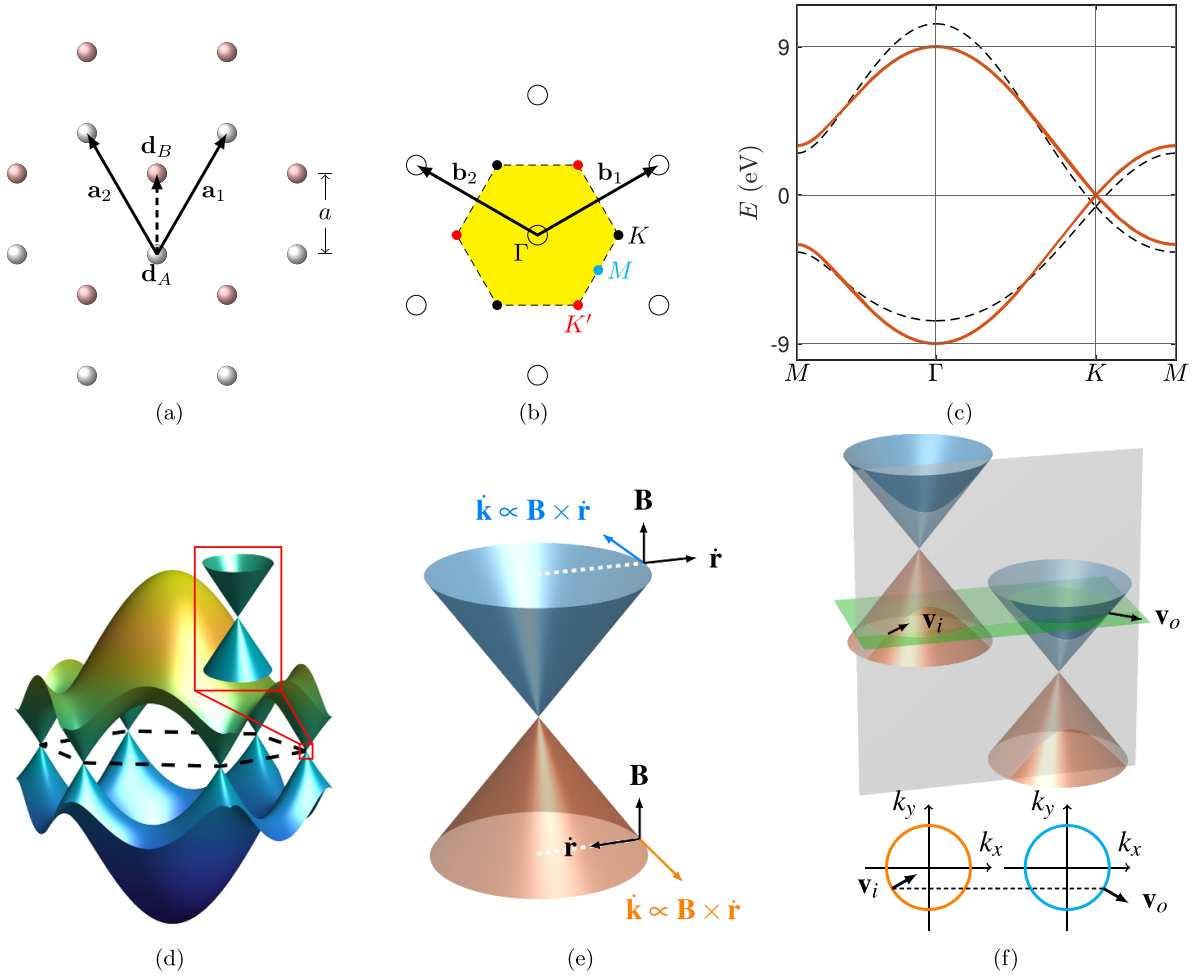

Figure 2. (a) Lattice structure of graphene which is composed of two hexagonal sublattices (gray and pink balls). (b) The corresponding reciprocal lattice (open circles) and the first Brillouin zone (yellow hexagon). (c) Band structures along k-path of $M\Gamma KM$ with $(t,t') = (-3, 0.23)$ eV (black dashed) and $(t,t') = (-3, 0)$ eV (red solid). (d) Surface plot of the band structure for the case of $t' = 0$. (e) The Dirac cone of graphene, i.e. its low energy band structure. (f) Schematics of shifted Dirac cones of a graphene p-n junction, assuming a Bloch electron incident from the p-region at velocity $\mathbf{v}_i$ and transmitted into the n-region at velocity $\mathbf{v}_o$.

is dominated by electron transport below 1 Kelvin [53]. The characteristic scales for electron-phonon dynamics in graphene nanostructures are typically an order of magnitude or more higher than the explored temperature ranges for electron quantum optics; e.g. the Bloch–Grüneisen temperature is in the few tens of Kelvin range in monolayer graphene [54], and the coupling to optical phonons is observed above a thousand Kelvin [55].

2. Introduction to graphene

2.1. Band structure

Graphene has a hexagonal lattice with a two-atom basis as depicted in figure 2(a), where $a \approx 0.142$ nm is the carbon-carbon bond length, $\mathbf{a}_1 = a_c(1/2, \sqrt{3}/2)$ and $\mathbf{a}_2 = a_c(-1/2, \sqrt{3}/2)$ are the primitive vectors, $a_c = \sqrt{3}a$ is the hexagonal lattice constant, and the basis vectors of the two atoms are $\mathbf{d}_A = (0,0), \mathbf{d}_B = (0,a)$. The corresponding reciprocal primitive vectors can be chosen as $\mathbf{b}_1 = 2\pi/\sqrt{3}a_c(\sqrt{3}, 1)$ and $\mathbf{b}_2 = 2\pi/\sqrt{3}a_c(-\sqrt{3}, 1)$ as shown in figure 2(b), where the empty dots are part of the hexagonal reciprocal lattice, and the yellow area bounded by a dashed hexagon is the (first) Brillouin zone (BZ), some symmetry points of which are marked.

2.1.1. Band structure of single layer graphene. Using a two-basis tight-binding model considering only p_z-orbitals up to second nearest neighbors, the energy bands of graphene within the entire BZ can be written as

$$E(\mathbf{k}) = \epsilon_p + t'F(\mathbf{k}) \pm t\sqrt{3 + F(\mathbf{k})} \tag{1}$$

where ϵ_p is the p_z-orbital energy (often set to zero), t and t' are the nearest and second-nearest neighbor hopping energy (equivalent to Slater–Koster parameter $V_{pp\pi}$ and $V'_{pp\pi}$), respectively, and the function $F(\mathbf{k})$ is defined by

$$F(\mathbf{k}) = 2\left(\cos k_x a + 2\cos\frac{k_x a}{2}\cos\frac{\sqrt{3}k_y a}{2}\right). \tag{2}$$

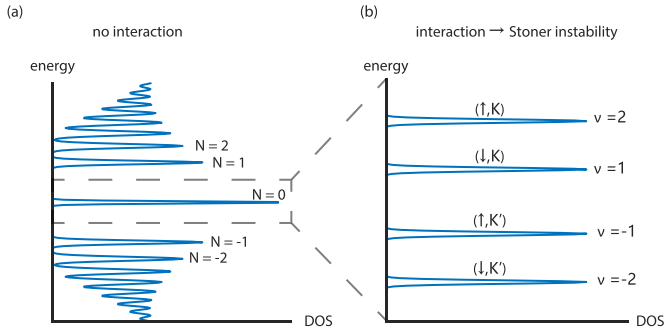

Figure 3. (a) In the absence of interaction, each graphene Landau level (denoted by the index N) is four time degenerate and each level energy is given by $E_N = \hbar\omega_C\sqrt{N+1/2}$. (b) Electron interactions lift up the spin and valley degeneracy through a Stoner instability, leading to broken symmetry states Landau level classified by the index ν.

The graphene band structure based on equations (1) and (2) along the k-path $M\Gamma KM$ points (marked on the BZ shown in figure 2(b)) is shown in figure 2(c), considering $t' \neq 0$ and $t' = 0$ cases. The surface plot of the band structure for the $t' = 0$ case is shown in figure 2(d), where the conic structure centered at K can be clearly seen. By Taylor expansion of equation (2) at $\mathbf{k} = K + \mathbf{q}$ with $|\mathbf{q}|a \ll 1$, it can be shown that up to terms quadratic in q, $F \approx -3 + 9q^2a^2/4$. Substituted into equation (1), we have $E(K_x + q_x, K_y + q_y) \approx \epsilon_p - 3t' \pm (3at/2)q$, which can be briefly written as

$$E_\sigma(k) \approx -3t' + \sigma\hbar v_{\mathrm{F}}k \tag{3}$$

where k is relative to K, $\sigma = \pm$ is the band index ($\sigma = +$ for the electron branch and $\sigma = -$ for the hole branch), $\epsilon_p = 0$ is chosen, and the Fermi velocity of graphene, v_{F}, is defined via

$$\hbar v_{\mathrm{F}} \equiv \frac{3}{2}|t|a \tag{4}$$

which is about 0.639 eV nm when using the commonly used approximate value of $t = -3$ eV. From this the value of v_{F} is about one nanometer per femtosecond, or $v_{\mathrm{F}} = 10^6\ \mathrm{m\,s^{-1}}$, which is $1/300$ of speed of light. Note that t' in equation (3) appears to be just a trivial band offset, but in the scope of strained graphene with nonuniform hopping, t' may play an interesting role of pseudoscalar potential [56–59].

2.1.2. Graphene Landau levels. Under high perpendicular magnetic field B, the band structure of graphene leads to a peculiar quantum Hall effect [44], characterized by an electron–hole symmetric spectrum of four-fold (spin and valley) degenerate Landau levels (see figure 3) with energies

$$E_N = \mathrm{sgn}(N)\sqrt{2e\hbar v_{\mathrm{F}}^2|NB|}\,, \tag{5}$$

with $-e$ the electron charge, $\hbar = h/2\pi$ the reduced Planck constant, N the Landau level index (positive for electron, negative for holes). For large magnetic fields, electron–electron interactions lift the spin and valley symmetries such that each Landau level splits into four sublevels that are fully spin and valley polarized [44, 45]. The 0th Landau level, pinned at zero energy, also splits into four sub-levels that reflect its half electron, half hole nature. If the Zeeman energy can be neglected with respect to interaction-driven spin and valley gaps (which generally occurs unless a strong in-plane magnetic field is applied [60], or a high-constant dielectric is used to screen interactions [61]), the 0-th Landau level splits into two electron-type sublevels with equal valley polarization (e.g. K) and opposite spins polarizations, and two hole-type sublevels with equal valley polarization (but opposite to that of the electron-type sublevels, e.g. K'), and opposite spin polarizations. Thus, at quarter filling, that is at filling factor $\nu = n_{\mathrm{e/h}}h/eB = \pm 1$ ($n_{\mathrm{e/h}}$ is the carrier density with respect to charge neutrality), both bulk and edge become fully spin and valley polarized [44, 45, 62]. At filling factor $\nu = 0$, the spin and valley symmetry breakings lead to a fully insulating state with no edge channels, the gap of which is about 150 K at $B = 10$ T, ten times larger than the Zeeman gap [45]. This insulating $\nu = 0$ state is crucial in many electron quantum optics experiments, as it allows to locally deplete the electron gas using electrostatic gates, in a manner similar to experiments realized in AlGaAs/GaAs heterostructures. Thus, the experiments described in this section mostly rely on locally changing the filling factor using gates to control the trajectories of edge channels, as well as their coupling.

2.1.3. Band structure of bilayer graphene. Similar to the tight-binding description of monolayer graphene, cf section 2.1.1, one can obtain the band structure of Bernal stacked bilayer graphene [63–65], taking into account intra-layer and inter-layer hoppings and inter-layer asymmetry, see figure 4. One finds four bands, two valence bands, and two conduction bands, see figure 4(b). In the low-energy expansion around the K-points (cf the discussion around equation (3)), bilayer graphene's bands can be described by

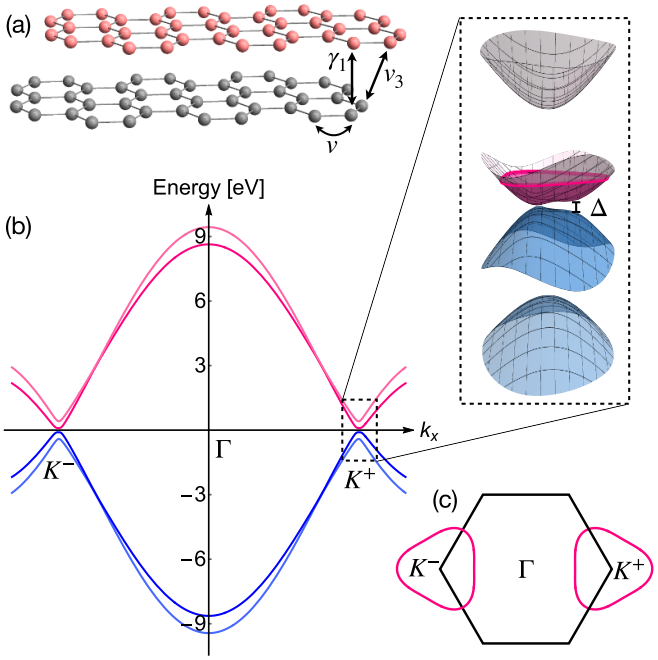

Figure 4. Lattice and electronic structure of bilayer graphene. (a) Lattice structure of Bernal stacked bilayer graphene. We indicate nearest neighbour intra-layer hopping (v), vertical inter-layer coupling (γ_1), and skew inter-layer coupling (γ_3). (b) Cut through the bilayer graphene band structure tracing the corners $K^{\pm}$ and the centre Γ of the Brillouin zone. There are four bands, two valence bands, and two conduction bands. Near the K points, one conduction band and one valence band are split from zero by an energy of the order of γ_1, while the remaining two bands constitute the low-energy bands. These low-energy bands touch at the K-points for zero inter-layer asymmetry (with an approximately parabolic dispersion), while finite inter-layer asymmetry opens a gap Δ. The inset shows the bands around the Brillouin zone corners as described by equation (6). (c) The skew hopping breaks rotational symmetry, leading to trigonally warped bands where the Fermi lines are of valley-dependent, triangular shape.

$$E^2 = \frac{\gamma_1^2}{2} + \frac{\Delta^2}{4} + \left(v^2 + \frac{v_3^2}{2}\right)k^2 + (-1)^{\alpha}\sqrt{\frac{\left(\gamma_1^2 - v_3^2k^2\right)^2}{4} + v^2k^2\left(\gamma_1^2 + \Delta^2 + v_3^2k^2\right) + 2\xi\gamma_1 v_3 v^2 k^3 \cos 3\varphi}, \tag{6}$$

where $\alpha = 1$ ($\alpha = 2$) yields the low-energy (split) bands, $\xi = \pm 1$ indexes the two valleys $K^{\pm}$, $\varphi = \arctan[k_x/k_y]$ is the polar angle of the momentum, and Δ is the interlayer asymmetry gap. Equation (6) captures vertical inter-layer coupling of the dimer sites (γ_1), in-plane nearest-neighbour intra-layer hopping (v), and skew inter-layer coupling between non-dimer orbitals (v_3).

The latter skew hopping parameter breaks rotational symmetry and induces trigonal warping to the parabolic bands, leading to triangularly deformed Fermi surfaces with opposing orientation in the $K^{\pm}$ valleys, see figure 4(c).

2.1.4. Density of states. Given the energy band of a certain material, the corresponding density of states $\rho(E)$, i.e. the density of the number of states at energy E, is generally given by the sum of contributions from all bands: $\rho(E) = \sum_{\sigma}\rho_{\sigma}(E)$ where

$$\rho_{\sigma}(E) = \frac{gA}{(2\pi)^2}\oint_{E_{\sigma}(\mathbf{k})=E}\frac{\mathrm{d}\ell_k}{|\nabla_k E_{\sigma}(\mathbf{k})|} \tag{7}$$

is the density of states of the σth band. Here, g is the degeneracy factor and A is the area of the 2D material. The above closed contour integral generally needs to be done numerically, but can be greatly simplified when the energy band is isotropic: $E_{\sigma}(\mathbf{k}) = E_{\sigma}(k)$, such as graphene at low energy. For bilayer graphene, on the other hand, the low-energy bands given by equation (6) are isotropic only when the skew inter-layer hopping $v_3 = 0$.

For graphene, we need to sum up all contributions from the six Dirac cones within the first BZ, with each cone described by equation (3) and shared by three BZs. A factor of $6/3 = 2$, also called the valley degeneracy $g_v = 2$, should be therefore taken into account. Together with the spin degeneracy $g_s = 2$, the total degeneracy factor in equation (7) for low-energy

graphene should be set to $g = g_s g_v = 4$. Since there is no overlap of energy bands, the contribution to the density of states is from either the electron branch ($\sigma = +$) or the hole branch ($\sigma = -$). Using $|\nabla_k E_\sigma(\mathbf{k})| = \hbar v_\mathrm{F}$ from equation (3), the density of states per unit area, $D(E) = \rho(E)/A$, is given by

$$D(E) = \frac{2|E|}{\pi(\hbar v_\mathrm{F})^2} \tag{8}$$

for the case of $t' = 0$ with the Dirac point at $E = 0$. For the case of $t' \neq 0$ with the Dirac point shifted to $-3t'$, as indicated by equation (3) and seen in figure 2(c), the density of states equation (8) should be modified with $|E| \to |E + 3t'|$. For BLG the quasi-quadratic dispersion relation leads to enhanced DOS close to CNP, leading to better screening of disorder and also to the enhancement of correlation effects.

2.1.5. Energy carrier density relation. At zero temperature, the carrier density n as a function of energy E can be obtained via

$$n(E) = \int_{E_0}^{E} D(E')\,\mathrm{d}E' \tag{9}$$

where E_0 is the charge neutrality energy which is zero for graphene with $t' = 0$. By inverting the relation, the Fermi energy as a function carrier density, $E(n)$, can be obtained. When energy bands are analytically available and are isotropic in $\mathbf{k}$, i.e. $E(\mathbf{k}) = E(k)$, the result from the above described approach is equivalent to replacing k in the energy dispersion with $n = gk^2/4\pi$, which gives

$$k = \sqrt{\pi|n|} \tag{10}$$

for graphene with $g = 4$. Substituting (10) into (3) for the case of $t' = 0$, we have

$$E(n) = \mathrm{sgn}(n)\,\hbar v_\mathrm{F}\sqrt{\pi|n|}\,, \tag{11}$$

where $n > 0$ and $n < 0$ correspond to n- and p-type graphene, respectively.

2.2. Semiclassical description for motion of carriers

In solids, the semiclassical dynamics of Bloch electrons (without the correction from the Berry curvature [66]) is governed by [67]

$$\dot{\mathbf{r}} = \frac{1}{\hbar}\nabla_k E_\sigma(\mathbf{k}) \tag{12}$$

$$\dot{\mathbf{k}} = -\frac{e}{\hbar}(\mathbf{E}_e + \dot{\mathbf{r}} \times \mathbf{B}) \tag{13}$$

where ∇_k is the gradient operator with respect to $\mathbf{k}$, $E_\sigma(\mathbf{k})$ is the energy band, σ is the band index, $\hbar$ is the reduced Planck constant, $-e$ is the electron charge, $\mathbf{E}_e$ is the electric field, and $\mathbf{B}$ is the magnetic field. For two-dimensional materials arranged in the x-y plane, the position vector is $\mathbf{r} = (x, y)$, and the wave vector is also two-dimensional, $\mathbf{k} = (k_x, k_y)$. Given an energy band $E_\sigma(\mathbf{k})$, equation (12) stands for two first-order ordinary differential equations (ODEs) for $\dot{x}$ and $\dot{y}$. Together with equation (13) that describes another two first-order ODEs, one for $\dot{k}_x$ and the other for $\dot{k}_y$, equations (12) and (13) represent four first-order coupled ODEs that can be numerically solved to describe the semiclassical dynamics of Bloch electrons in 2D. Without having to bother with such numerics, however, the following section provides a simple understanding of the basic properties of Dirac electrons in graphene based on equations (12) and (13).

2.2.1. Cyclotron motion. To describe the semiclassical motion of the Bloch electron in the present focus of graphene, it is sufficient to adopt the low-energy dispersion equation (3), which exhibits a conic band structure, known as the Dirac cone, already shown in the inset of figure 2(d) and now elaborated in figure 2(e), where carriers occupying the upper branch ($\sigma = +$) behave like negatively charged electrons and those occupying the lower branch ($\sigma = -$) behave like positively charged holes. The behaviors of electron-like and hole-like carriers can be understood by considering Bloch electrons in graphene applied with only $\mathbf{B} = (0, 0, B) = B\hat{\mathbf{e}}_z$ where B is constant and $\hat{\mathbf{e}}_z$ is the unit vector along the z axis. The absence of $\mathbf{E}_e$ simplifies equation (13) to

$$\dot{\mathbf{k}} = -\frac{e}{\hbar}\dot{\mathbf{r}} \times \mathbf{B}\,. \tag{14}$$

By a bit of mathematical processing [67], the above equation (14) leads to the following geometric relation:

$$\mathbf{r}(t) - \mathbf{r}(0) = \frac{\hbar}{eB}[\mathbf{k}(t) - \mathbf{k}(0)] \times \hat{\mathbf{e}}_z, \tag{15}$$

which indicates that the real-space trajectory of a Bloch electron is just its reciprocal-space trajectory scaled by $\hbar/eB$ and rotated about the z-axis by 90 degrees clockwise.

Since the magnetic force is perpendicular to the group velocity $\dot{\mathbf{r}}$ and does not alter the kinetic energy, the motion of a Bloch electron in a constant magnetic field is a constant-energy motion. Put in another way, its reciprocal-space trajectory is a constant-energy contour, i.e. the Fermi contour for Bloch electrons at the Fermi energy. At sufficiently low energies, the Fermi contour is a circle of radius k, with which equation (15) indicates that the corresponding real-space trajectory is a circle of radius

$$r_c = \frac{\hbar k}{eB}\,, \tag{16}$$

called cyclotron radius. Whereas the above discussion is valid independent of the band structure, the cyclotron radius formula equation (16) is applicable also for other 2D materials with isotropic dispersion relation.

2.2.2. Electron and hole orbits. Equation (14), together with the group velocity $\dot{\mathbf{r}}$ given by equation (12), allows us to distinguish between electron and hole orbits. Since the group velocity $\dot{\mathbf{r}}$ is directed along the energy gradient, which is radially

outward for the electron branch and inward for the hole branch (see figure 2(e)), how $\dot{\mathbf{k}}$ evolves with time follows the direction of $\mathbf{B}\times\dot{\mathbf{r}}$, leading to counterclockwise and clockwise orbits for electrons and holes, respectively; see figure 2(e).

Note that the above argument is valid not only for graphene. What makes graphene different from its linear energy dispersion equation (3) is that the group velocity equation (12) explicitly reads

$$\mathbf{v} = \sigma v_{\mathrm{F}} \frac{\mathbf{k}}{|\mathbf{k}|} , \tag{17}$$

whose magnitude is always v_{F}, independent of energy.

2.2.3. Cyclotron frequency. The energy-independent magnitude of the group velocity equation (17) leads to distinct behaviors of electrons in graphene compared to non-Dirac materials where the energy dispersion is not linear in k. Take the cyclotron motion for example. Because of the constant $|\mathbf{v}| = v_{\mathrm{F}}$, the smaller the cyclotron radius, the shorter the time needed for the electron to complete a cycle, which is in sharp contrast with electrons in usual two-dimensional electron gas (2DEG) where $E(k) = \hbar^2k^2/2m^*$, the magnitude of group velocity then clearly depends on energy: $|\mathbf{v}| = \hbar k/m^* = \sqrt{2E/m^*}$, leading to energy-independent cyclotron frequency $|\mathbf{v}|/r_c = eB/m^*$. Using the effective mass of GaAs, $m^* = 0.067m_e$, m_e the bare electron mass, the cyclotron frequency in 2DEG confined in GaAs is about 2.63 THz under $B = 1$ T. On the other hand, the cyclotron frequency in graphene is energy-dependent:

$$\omega_c = \frac{eBv_{\mathrm{F}}^2}{E} , \tag{18}$$

which ranges between a few THz ($E > 100$ meV) to about one hundred THz ($E \lesssim 10$ meV) under the same magnetic field of $B = 1$ T.

2.2.4. Negative refraction. Although the problem of transmission across a graphene p-n junction will be elaborated in more details in section 2.3, the above semiclassical description allows us to easily understand the origin of negative refraction in graphene.

Suppose a graphene sheet is subject to an on-site energy band offset arranged in a way that the Dirac cone in the left (right) region is shifted upward (downward) in energy, forming a graphene p-n junction; see figure 2(f), where the horizontal green plane is the global Fermi energy, and the circles in the bottom part of the figure are the Fermi circles in the corresponding regions. Because the left region is p-type, the group velocity points radially inward as explained above, and a possible incoming state with positive x-component of the group velocity vector $\mathbf{v}_i$ is shown in figure 2(f). After transmission across the p-n junction with the k_y component conserved, the Bloch electron occupies a state in the n-region at the Fermi energy with the resulting group velocity $\mathbf{v}_o$ which points radially outward of the Dirac cone (see figure 2(f)), leading naturally to the negative refraction of the Bloch electron because $\mathbf{v}_i$ and $\mathbf{v}_o$ lie on opposite side of the incidence normal (dashed line in figure 2(f)).

The above explanation considers the special case of a symmetric p-n junction where the Fermi energies in the p and n regions are equal in magnitude and opposite in signs. Whereas more general cases will be elaborated in section 2.3.1, from the simple picture based on the semiclassical description here, it can be seen that the origin of the negative refraction for electrons traversing p-n junctions in graphene arises from the opposite energy gradient of the conductance and valence bands.

2.3. Graphene junctions

If one uses two gates, for example, one bottom and one top-gate, one can define regions of different doping and gate-controlled p-n devices. If the doping has the same sign on the two sides (n-n' or p-p') it is called a unipolar junction, if it changes sign it is a bipolar (p-n or n-p) junction. The sharpness of the change in potential profile can also vary: the carrier density can switch sharply or smoothly, depending on the geometrical parameters and on screening properties in general. If the gate electrodes are very close to the graphene layer, the potential step is more abrupt as compared to the case when thicker insulating barrier layers are employed. The sharpness of the potential affects how electrons traverse the p-n region. In the 'abrupt' case, the p-n junction can be seen as a 'thin' scattering region.

2.3.1. Snell's law. Consider an infinitely extending graphene sheet arranged in the x-y plane, subject to a potential profile $V(x)$ causing an interface along the y direction. Let the left (right) region be the incoming (outgoing) region labeled by i (o). The local Fermi energy, i.e. the highest filled energy relative to the Dirac point, is E_i in the incoming region and E_o in the outgoing region. We consider an incoming state occupying a wave vector $\mathbf{k}_i$ corresponding to E_i and a positive x-component of the group velocity $\mathbf{v}_i$. The outgoing wave vector $\mathbf{k}_o$ corresponding to energy E_o also has positive x-component of the group velocity $\mathbf{v}_o$, as shown figure 5.

Regardless of the sign of E_i and E_o, Snell's law for electrons in graphene is simply the conservation of the y-component of the wave vector,

$$k_{y,i} = k_{y,o} , \tag{19}$$

due to the translational invariance along y. Without loss of generality, we fix $E_o > 0$ and consider two cases of $E_i > 0$ and $E_i < 0$, the former corresponding to a unipolar nn junction and the latter a bipolar p-n junction.

2.3.1.1. Unipolar nn junction. When both of E_i and E_o are positive, the band offset profile and the local energy bands are schematically shown in figure 5(a). Since the group velocity is parallel to the wave vector for n-type graphene, as indicated by equation (17), both of $\mathbf{k}_i$ and $\mathbf{k}_o$ have positive components along k_x, as shown in figure 5(b). Since the angle of incident

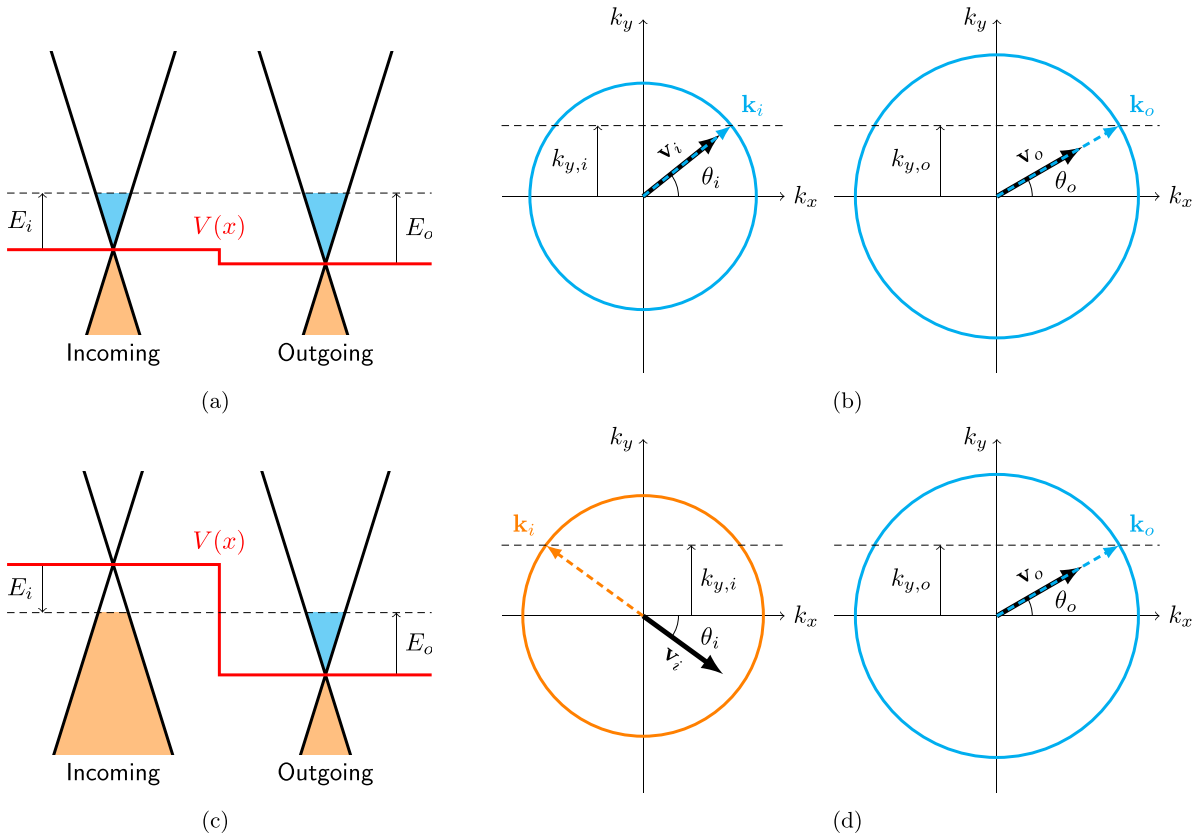

Figure 5. Band offset profiles $V(x)$ and local energy band diagrams of (a) a unipolar nn junction, whose corresponding Fermi circles are shown in (b), and (c) a bipolar p-n junction, whose corresponding Fermi circles are shown in (d).

(refraction), θ_i (θ_o), defined as the angle between the incoming (outgoing) velocity and the normal of the interface (i.e. the x- or equivalently the k_x-axis), is the same as the azimuthal angle of $\mathbf{k}_i$ ($\mathbf{k}_o$), the conservation of k_y equation (19) reads $k_i \sin\theta_i = k_o \sin\theta_o$, where $k_i = |\mathbf{k}_i|$ and $k_o = |\mathbf{k}_o|$. Multiplying the equation by $\hbar v_\mathrm{F}$, we have $E_i \sin\theta_i = E_o \sin\theta_o$.

We note, that for unipolar junctions it is even possible to achieve total internal reflection if the incident angle is large enough.

2.3.1.2. Bipolar p-n junction. For a p-n junction with $E_i < 0$ and $E_o > 0$ (figure 5(c)), we consider $\mathbf{k}_i$ with a negative k_x-component in order to have a positive x-component of the group velocity $\mathbf{v}_i$, as shown in figure 5(d). Because of equation (17), $\mathbf{v}_i$ is now antiparallel to $\mathbf{k}_i$, and the angle of $\mathbf{k}_i$ is not just the angle of incidence θ_i, but $\theta_i + \pi$. Therefore, the conservation of k_y equation (19) reads $k_i \sin(\theta_i + \pi) = k_o \sin\theta_o$. Multiplying the equation by $\hbar v_\mathrm{F}$, we have $-\hbar v_\mathrm{F} k_i \sin\theta_i = \hbar v_\mathrm{F} k_o \sin\theta_o$. Since $k_i = |\mathbf{k}_i|$ and $k_o = |\mathbf{k}_o|$ are both positive, we have $E_i = -\hbar v_\mathrm{F} k_i$, and the resulting Snell's law

$$E_i \sin\theta_i = E_o \sin\theta_o \tag{20}$$

remains the same form as that in the previous case of the nn junction. Equation (20) is valid for both unipolar and bipolar junctions, with none of $\theta_i, \theta_o, E_i, E_o$ restricted to positive. In the case of bipolar junctions with $E_i E_o < 0$, the angles of incidence and refraction must, in view of equation (20), be of opposite signs: $\theta_i \theta_o < 0$, consistent with the negative refraction described in section 2.2.4.

2.3.2. Transmission across graphene junctions. The Snell's law equation (20) discussed above indicates that the role of refraction index in ray optics is played by Fermi energy in electron optics of graphene. The equation gives a constraint for the angles of incidence and refraction, but says nothing about the quantum-mechanical transmission yet.

In the literature, two main approaches are adopted in solving the problem of transmission across graphene junctions: analytical Dirac equation and numerical tight-binding model. The former leads to useful formulas but is restricted to simple potential profiles. The latter is not restricted to any potential profile but provides only numerical results without any neat formulas. At low-energy, the tight-binding approach agrees with the analytical formulas obtained from solving the Dirac equation, as was shown in [68] for the case of sharp p-n junctions [11], linearly smooth p-n junctions [11], and sharp n-p-n junctions [9] for graphene. The case of gapless bilayer graphene n-p-n junctions discussed in [9] was also reproduced by the numerical tight-binding method [68] but below we briefly review only the cases of single layer graphene junctions.

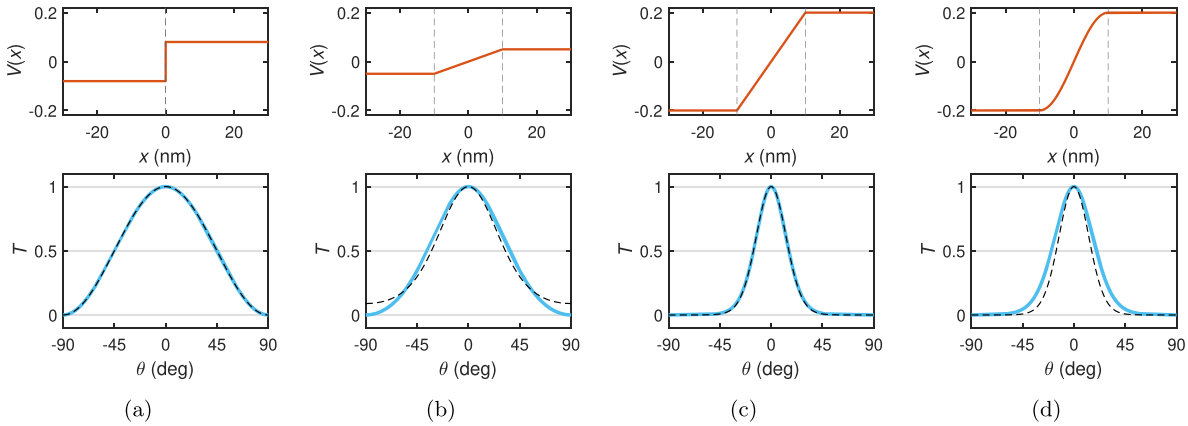

Figure 6. Angle-resolved transmission of symmetric graphene p-n junctions considering (a) a sharp (abrupt) junction of potential difference 0.16 eV and (b) a linearly smooth junction of potential difference of 0.1 eV and smoothing thickness $d = 20$ nm. Diagrams of (c) are similar to (b) with the only difference being the potential difference increased to 0.4 eV. (d) considers a nonlinear smooth p-n junction. Upper panels of each subfigure show the onsite-energy profile $V(x)$ and the lower panels show the angle-resolved transmission $T(\phi)$ based on the numerical tight-binding model (thick solid cyan curves) and analytical formulas (dashed black curves). (a)–(c) are modified and reproduced from [68].

2.3.2.1. Sharp p-n junctions. Graphene subject to a potential profile $V(x)$ shown in figure 5(c) is the case of an asymmetric sharp p-n junction. The upper panel of figure 6(a) is a case of a symmetric p-n junction, across which the transmission as a function of the angle of incidence, denoted as θ for brevity, has a neat expression first derived based on the Dirac equation in [11]:

$$T(\theta) = \cos^2\theta\,, \tag{21}$$

which is shown in the lower panel of figure 6(a) by the black dashed curve. The result is independent of the potential height and can be reproduced by using the numerical tight-binding approach (thick solid cyan curve in figure 6(a) [68]. The transmission at all angles is non-zero, but most strikingly, for $\theta = 0$ transmission probability approaches one! This surprising effect is known as Klein tunneling [25].

2.3.2.2. Smooth p-n junctions. If the potential varies smoothly on the scale of the Fermi wavelength λ_F, electrons incident from the left with an angle $\theta > 0$ relative to the normal of the scattering region are smoothly bent within the scattering region. If the carrier density now truly crosses from n-type to p-type, the electrons are bent off the scattering region, never reaching the other side. This is schematically shown in figure 7(a). One would therefore predict a transmission probability of zero in case of a p-n junction with a smooth 'soft' potential change.

As shown in [11] based on the Dirac equation, the angle-resolved transmission $T(\theta)$ for a linearly smooth p-n junction such as those considered in figure 6(b) or 6(c), can be described by

$$T(\theta) = \exp\left(-\pi\frac{k_F d}{2}\sin^2\theta\right)\,, \tag{22}$$

when the product of the Fermi wave vector[8] k_F and the smoothness d fulfills $k_F d \gg 1$. Two examples for such linearly smooth p-n junctions are shown in figure 6(b) with $k_F d \approx 1.54$ and figure 6(c) with $k_F d \approx 6.16$.

The simulation also shows that the situation is again angle dependent. For incident electron trajectories that are nearly perpendicular to the scattering region with the line of zero density located at position x_0, the probability for transmission $T(\theta)$ gets appreciable. The angle dependence shown in figures 7(a) and 6(b)–(d) can be understood in a qualitative manner as follows: appreciable transmission sets in when the classical electron trajectory approaches x_0 at a distance l_{min} with the condition that the Fermi wavelength at this position exceeds l_{min}. In this case, there is appreciable wavefunction overlap between the two sides.

We note, that the analytical formula of equation (22) does not match the numerical tight-binding results for the case of figure 6(b) because $k_F d \gg 1$ is not fulfilled, while the agreement for the case of figure 6(c) can be seen. Figures 6(a)–(c) have been shown in [68]. For completeness, we show another p-n junction in figure 6(d) which is the same as figure 6(c) except that the junction profile is not linear but modeled by a sine function; see the upper panel of figure 6(d). The $T(\theta)$ is analytically difficult to solve but remains numerically straightforward. Nevertheless, because of $k_F d \gg 1$, the difference between the two approaches is not drastic, as seen in the lower panel of figure 6(d). We conclude that the exponential form of equation (22) can always serve as a good approximation for smooth n-p and p-n junctions.

[8] Note that the Fermi wave vector is temporarily denoted as k_F here in order to be consistent with the literature, but is mostly denoted simply as k in the rest of our discussions.

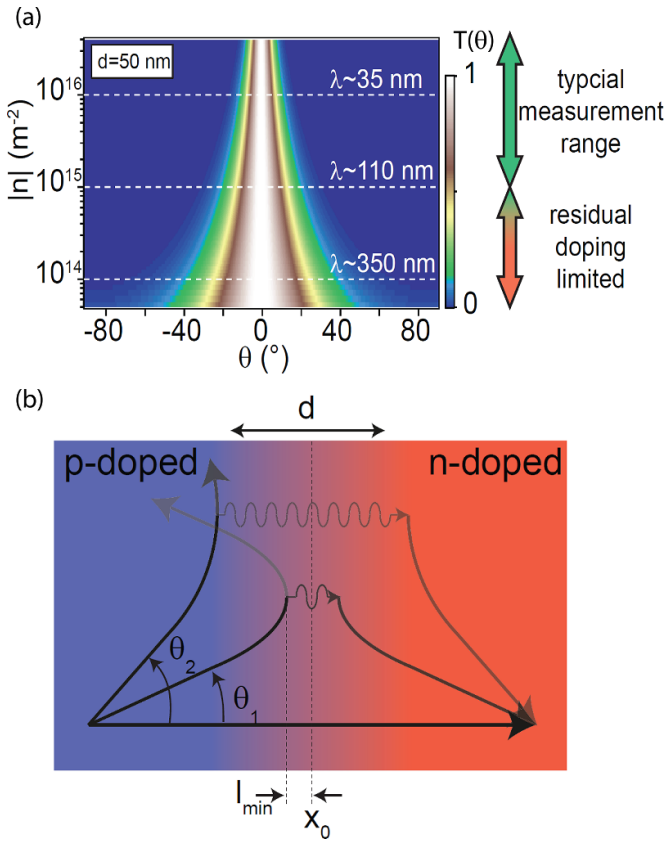

Figure 7. Electron transmission at a p-n junction. The graph in (a) shows the expected transmission probability color coded as a function of incident angle θ and carrier density n. Here, an equation for a smooth potential change has been used according to [9]: $t(\theta) = \exp(-\pi k_F d \sin(\theta)^2)$. Reproduced with permission from [69]. The semiclassical particle trajectories illustrate in (b) how they are repelled from the region of zero carrier density which is located at position x_0. The smaller the incident angle θ, the closer the trajectories approach x_0. If the remaining classical distance l_{min} gets shorter than the Fermi wavelength λ_F, the wavefunction will have an appreciable overlap on the other side leading to an increase in transmission probability. Quite remarkably, for $\theta = 0$ transmission probability approaches unity. This is known as Klein tunneling.

2.3.2.3. Klein tunneling. Whether sharp (equation (21)) or smooth (equation (22)), the transmission probability across a graphene p-n junction at normal incidence is always perfect: $T(0) = 1$, which resembles the original Klein paradox in relativistic quantum electrodynamics [70], and is often referred to as the Klein tunneling [71–73].

2.3.2.4. Interfaces at contact electrodes. In experiments mostly soft p-n interfaces are often reported. Suspended graphene devices have typically a soft p-n junction, while encapsulated devices can have sharper potential steps approaching the 10 nm range, determined by the thickness of the gate insulator. However, there are inherent potential steps at the contacts themselves. This has two reasons: a) depending on the contact material, the workfunction difference between the metal and graphene results in an exchange of carriers, hence, to a region of contact doping; b), due to screening properties, the metal contacts can also be seen as an effective capacitor. Together with the gate capacitor(s), this changes the so-called gate-lever arms in the vicinity of the contact region. Again, one expects a change in carrier density in the vicinity of contacts. Since the metal electrode is in direct contact with the graphene sheet, this potential change can be rather steep. Consequently, as long as diffusive scattering can be disregarded, a normal metal contacts can also be seen as a (partially) reflecting mirror as will be seen e.g. in figure 24.

2.4. Ballistic conductance

For a two-dimensional material of width W at energy E corresponding to the magnitude of the wave vector k, the number of modes is given by

$$M = \frac{kW}{\pi}\,, \tag{23}$$

which is obtained from $2k/(2\pi/W)$ and is just the number of k_y points (assuming the transport direction is along x). This estimation arises from the assumption of applying the periodic boundary condition along the y dimension, and becomes exceptionally precise whenever W is sufficiently large, or in simpler terms it counts how many times the half wavelength of electrons' fits into the transport channel. Taking into account the degeneracy factor g, the ballistic conductance of the material in the absence of any potential, defect, and disorder, is given by

$$G = \frac{e^2}{h} g M\,, \tag{24}$$

according to the Landauer formula [74].

2.4.1. Pristine graphene. Using $g = 4$ for graphene (section 2.1.4) and substituting equation (23) into equation (24), we have the ballistic conductance for pristine graphene:

$$G = \frac{e^2}{h}\frac{4W}{\pi}k\,, \tag{25}$$

which is plotted in figure 8(a) (solid cyan curve), considering an example of $W = 1$ μm. Note that from the above equations (23) and (24), the ballistic conductance of all 2D materials exhibit such a linear-in-k dependence, or square-root-in-n dependence when using $k = \sqrt{\pi|n|}$ (section 2.1.5), up to a different degeneracy factor g.

2.4.2. Ballistic graphene p-n junctions. When the pristine graphene is subject to a potential $V(x)$ without breaking the translation symmetry along y, the contribution of each k_y mode to the conductance is generally limited by the transmission probability $0 \leqslant T(k_y) \leqslant 1$. By summing over contributions from all modes, the ballistic conductance is given by

$$G = \frac{e^2}{h}\frac{2W}{\pi}\int_{-k}^{k} T(k_y)\,\mathrm{d}k_y\,, \tag{26}$$

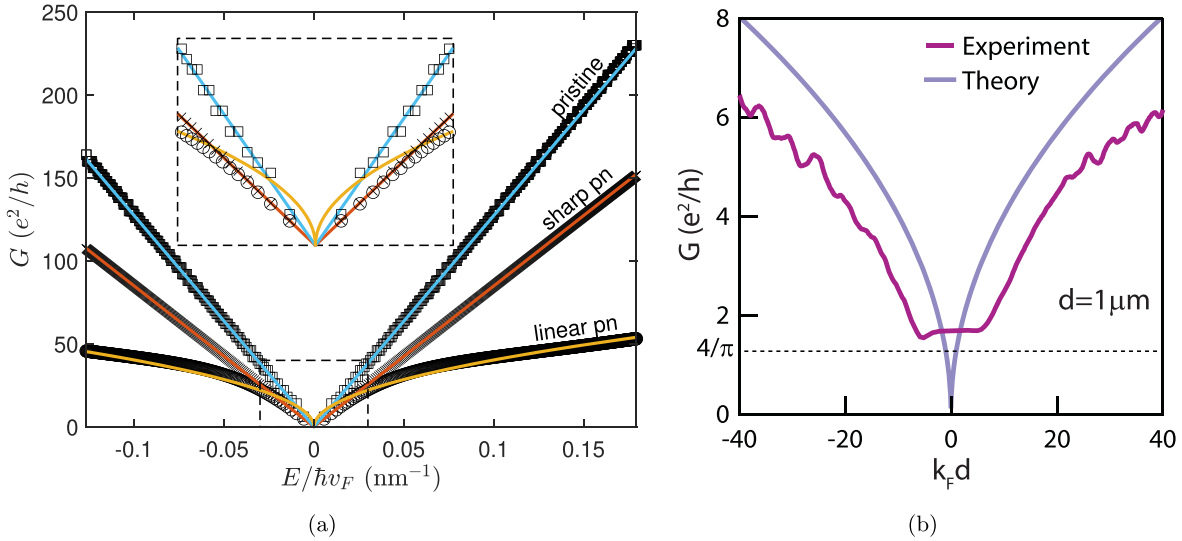

Figure 8. Energy (and hence wave vector) dependence of graphene conductance in the clean limit. (a) Ballistic conductance as a function of $E/\hbar v_{\rm F}$ based on analytical formulas (colorful solid lines) and numerical quantum transport simulations (black markers), considering a pristine graphene sheet (cyan curve and black squares), a sharp graphene pn junction (red curve and black crosses), and a linearly smooth ($d = 50$ nm) graphene pn junction (orange curve and black circles), all with width $W = 1$ μm. The inset shows the range of $E/\hbar v_{\rm F} \in [-0.03, 0.03]$ nm^{-1} and $G \in [0, 40]$ e^2/h. (b) Ballistic conductance of a suspended graphene pn junction: experiment vs theory; taken from [75]. The smoothness of the junction and the width of the graphene sample are assumed to be $d = 1$ μm and $W = 2$ μm, respectively.

which recovers equation (25) when $V(x) = 0$ such that $T(k_y) = 1$ for all $-k \leqslant k_y \leqslant k$. For arbitrary $V(x)$, the transmission $T(k_y)$ can be numerically computed, but no neat formulas for the resulting conductance equation (26) can be obtained in general, except the two special cases reviewed in section 2.3.2.

For symmetric sharp p-n and n-p junctions, using equation (21) we have $\int_{-k}^{k} T(k_y) {\rm d}k_y = 4k/3$, and the conductance is precisely given by

$$G = \frac{e^2}{h}\frac{8W}{3\pi}k\,, \tag{27}$$

which differs from equation (25) only by a factor of $2/3$, indicating that an ideally sharp graphene p-n junction is rather transparent (highly conductive); see the red solid curve in figure 8(a).

For linearly smooth p-n and n-p junctions, the $\int_{-k}^{k} T(k_y) {\rm d}k_y$ integral is not analytically solvable even using equation (22) when $kd \gg 1$ is fulfilled. However, as we have seen in figure 6(c), $T(\theta)$ decays to zero well before $\theta = \pm\pi/2$, which means that approximating the integral as $\int_{-\infty}^{\infty} T(k_y) {\rm d}k_y = \int_{-\infty}^{\infty} \exp\left(-\pi\, {\rm d}k_y^2/2k\right) {\rm d}k_y = \sqrt{2k/d}$ is quite fine. Substituted into equation (26), the final result is [11]

$$G \approx \frac{e^2}{h}\frac{2W}{\pi}\sqrt{\frac{2k}{d}}\,, \tag{28}$$

which has a square-root-in-k dependence, contrary to equations (25) and (27), as shown by the solid orange curve in figure 8(a).

Note that the horizontal axis of figure 8(a) summarizing the k dependence of the ballistic conductance for a pristine graphene sheet, equation (25), a sharp graphene p-n junction, equation (27), and a linearly smooth graphene p-n junction, equation (28), is $E/\hbar v_{\rm F}$ instead of k, because k is defined positive in our discussions while E can be negative. All of the three cases well agree with the numerical results (black markers) based on quantum transport simulations, to be briefly reviewed in the following section 2.5.

It is also nice to illustrate how close experimental graphene p-n junctions come to theoretical prediction for a clean device with soft potential. Figure 8(b) shows a comparison of an actual measurement with the theoretical prediction. The measured dependence does indeed follow a square-root dependence $G \propto \sqrt{k_{\rm F}}$, proving that the potential barrier is smooth and varies in this example on a length scale of $d = 1$ μm. The comparison also reveals that there is an additional contact resistance of order $2e^2/h$ in series to the junction resistance. Finally, the conductance G does not approach zero at the Dirac point, as there should be a cut-off which theory predicts to be $G_{\rm min} = 4e^2/\pi h$ [9]. That the experimentally measured minimal conductance is close to the ideal ballistic limit illustrates the cleanliness of this device [75].

2.5. Quantum transport simulation for clean graphene

Quantum transport in the framework of Landauer-Büttiker formalism [74] is an exceptionally useful and powerful tool, especially for low-bias, low-temperature transport in the clean limit. To focus on clean graphene devices, let us summarize the formalism by considering an exemplary two-terminal suspended graphene device.

2.5.1. Real-space Green's function method. As shown in figure 9(a), the system we are interested in is composed of a

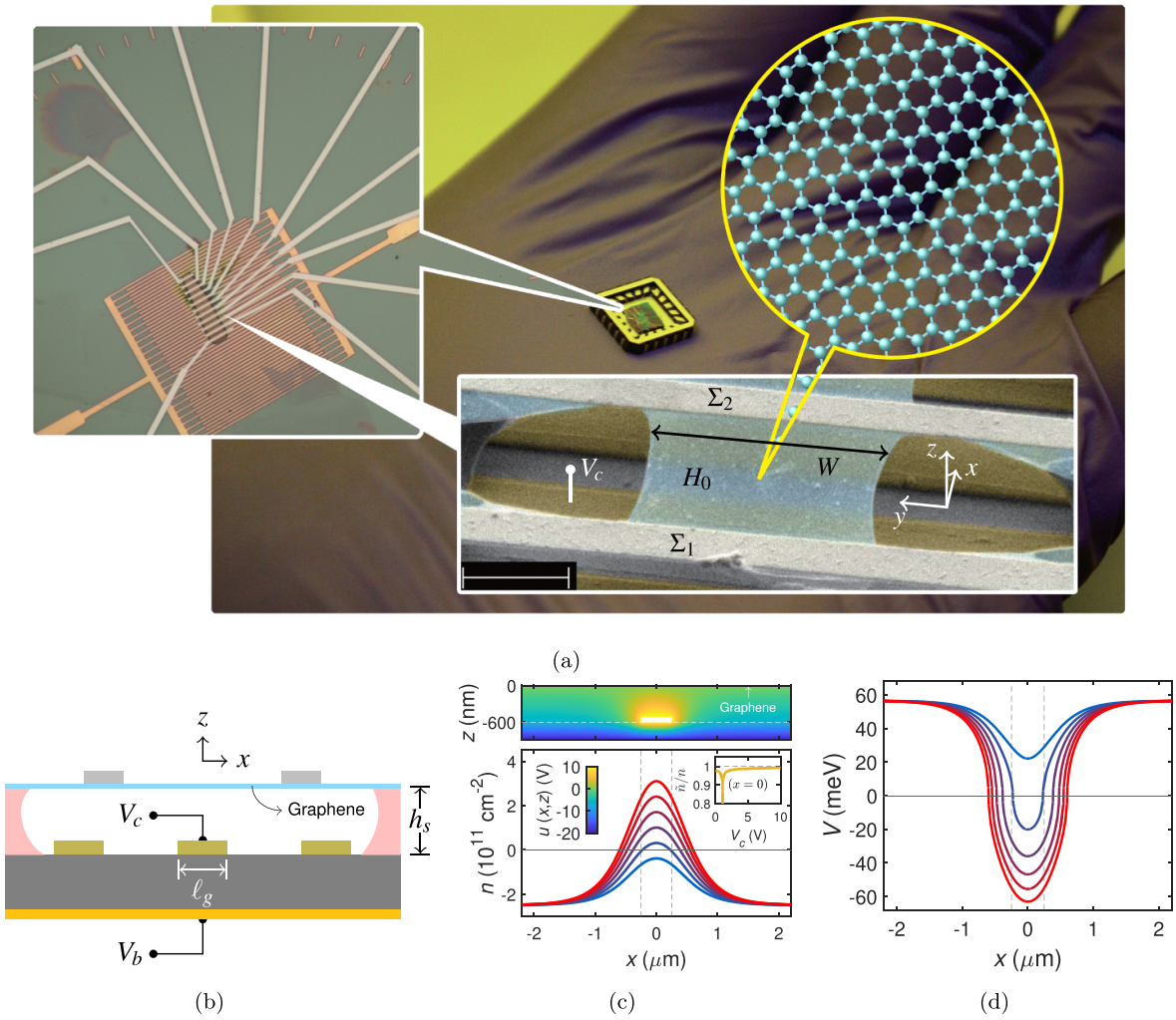

Figure 9. (a) Optical images (background and left) of exemplary suspended graphene devices. Lower right: An SEM image of a two-terminal device made of a suspended graphene sample (described by a tight-binding Hamiltonian H_0) attached to two contacts (described by Σ_1 and Σ_2) and tuned by a central gate at voltage V_c (marked on the figure) and a global backgate at voltage V_b which is not shown in (a) but sketched in (b). (b) Schematics of the side view of the device shown in the SEM image of (a). Considering $(\ell_g, h_s) = (500, 600)$ nm and $V_b = -20$ V, (c) shows carrier density profiles $n(x)$ of graphene at $V_c = 0$ V (blue), 2 V, $\cdots$, 10 V (red), and their corresponding on-site energy profiles $V(x)$ are shown in (d). The upper part of (c) shows an example of the electrostatic potential $u(x,z)$ at $(V_c, V_b) = (10, -20)$ V, and the inset shows $\tilde{n}/n$ vs V_c at $x = 0$ with the same fixed $V_b = -20$ V.

scattering region described by a clean Hamiltonian H_0 and the attaching electrical contacts described by Σ_1 and Σ_2, i.e. the so-called lead self-energies. To model and simulate electronic devices in real space, the local orbitals of the atoms composing the lattice may be chosen as the basis to represent H_0. Considering only the p_z orbital of the carbon atoms, the real-space tight-binding Hamiltonian can be written as

$$H_0 = t \sum_{\langle i,j \rangle} c_i^\dagger c_j + t' \sum_{\langle\langle i,j \rangle\rangle} c_i^\dagger c_j \,, \tag{29}$$

where $c_i^\dagger$ (c_i) creates (annihilates) an electron on site i located at position $\mathbf{r}_i$, so that $c_i^\dagger c_j$ stands for an electron hopping from $\mathbf{r}_j$ to $\mathbf{r}_i$, and $\sum_{\langle i,j \rangle}$ ($\sum_{\langle\langle i,j \rangle\rangle}$) means that the sum runs over all nearest (second nearest) neighboring site pairs fulfilling $|\mathbf{r}_i - \mathbf{r}_j| = a$ ($|\mathbf{r}_i - \mathbf{r}_j| = \sqrt{3}a$); see figure 2(a) for the definition of a. Despite that equation (29) describes a finite-sized graphene without translational invariance, the hopping parameters t and t' are often assumed to be the same as those for the energy bands introduced in section 2.1.1 where translational invariance is the basic requirement.

Apart from the clean part of the graphene Hamiltonian, H_0, the on-site energy term appearing as a diagonal matrix,

$$U = \sum_i V(\mathbf{r}_i)\, c_i^\dagger c_i \,, \tag{30}$$

takes into account electrons' potential energy from all different sources, such as electrical gating, chemical doping, contact doping, disorder, atomic orbital energy, and so on. In the clean limit, equation (30) mainly describes the electrical gating, which will be explained in the following section 2.5.2.

Together with the lead self-energies Σ_1 and Σ_2 describing the electrical contacts which serve as electron reservoirs,

the effective Hamiltonian describing the contact-graphene-contact system can be written as

$$H(E) = H_0 + U + \Sigma_1(E) + \Sigma_2(E) \ , \tag{31}$$

which is a function of energy E because the lead self-energies depend on E. Commonly adopted methods for calculating the lead self-energies include eigenfunction expansion [74], eigendecomposition and Schur decomposition [76], and recursive Green's function [77], but are beyond the scope of this review.

Once equation (31) is built, the retarded Green's function at energy E is by definition given by

$$G_R(E) = [E - H(E)]^{-1} \ . \tag{32}$$

Since all terms in equation (31) are $N_s \times N_s$ square matrices, N_s being the total number of lattice sites, the above equation (32) stands for a matrix inversion, which is computationally heavy unless N_s is small. For graphene, it is possible to rescale the lattice to reduce N_s, to be explained in the following section 2.5.3. Note, however, that even N_s is not too large, inverting the entire matrix $[E - H(E)]$ is not necessary, because not all elements of $G_R(E)$ are needed. Technical details are crucial at this point but are also beyond the scope of this review.

With the retarded Green's function obtained, together with the broadening matrices

$$\Gamma_p(E) = -2\mathrm{Im}\Sigma_p(E) \tag{33}$$

corresponding to the pth lead self-energy, the transmission function from lead q to lead p at energy E can be obtained:

$$T_{p\leftarrow q}(E) = \mathrm{Tr}\left[\Gamma_p(E) G_R(E) \Gamma_q(E) G_A(E)\right] \tag{34}$$

where $G_A(E) = G_R^\dagger(E)$ is the advanced Green's function matrix.

2.5.2. Realistic on-site energy. When tuning the carrier density of graphene by electrical gating, what does the gate do? To a simple picture, when a positive gate voltage is applied, negative charges are induced on the surface of graphene, causing the raise of Fermi level, and vice versa. The change of the Fermi level can also be understood as the change of the entire energy bands with the Fermi level fixed. This picture is more useful when the carrier density is not uniform, corresponding to a spatially varying energy band offset, which is exactly the $V(\mathbf{r})$ in equation (30).

Without taking into account the correction due to quantum capacitance [78–81] and assuming no intrinsic doping, $n_0 = 0$, the carrier density profile of graphene is given by the following linear superposition of the classical contribution,

$$n(\mathbf{r}) = \sum_j \frac{C_j(\mathbf{r})}{e} V_j \ , \tag{35}$$

where $C_j(\mathbf{r})$ is the capacitance profile of the jth gate which can be either analytically described by a proper model function or numerically obtained by solving the Poisson equation [81] using commercial software such as COMSOL [82] or finite-element-based partial differential equation (PDE) solvers such as FENICS in PYTHON [83] or PDEMODELER (PDETOOL in older versions) of MATLAB [84].

To continue with the example of suspended graphene, consider the scanning electron microscopy (SEM) image of figure 9(a)(lower right), whose side view is schematically shown in figure 9(b). The carrier density of the graphene sample placed at $z = 0$ is tuned by a central gate at voltage V_c and a back gate at voltage V_b. Since the width of the graphene sample W is sufficiently large and the geometry of the metal contacts and gates does not depend on y, we may consider the two-dimensional Laplace equation $\nabla^2 u = 0$ to solve for the electrostatic potential $u(x,z)$, subject to properly assigned boundary conditions. The suspension height h_s is typically several hundreds of nanometers and is roughly the smoothness of gate capacitance profiles. This means that the resulting carrier density and onsite energy profiles are completely smoothed (exhibiting no plateaus) whenever the gate length $\ell_g \lesssim h_s$, which is the case in the example shown here.

An exemplary solution of $u(x,z)$ subject to $(V_c, V_b) = (10, -20)$ V is shown in the top panel of figure 9(c), considering $(\ell_g, h_s) = (500, 600)$ nm. From the surface gradient of u at $z = 0^-$, the corresponding surface charge density (and hence the carrier density in graphene) can be obtained [81]. Because the Laplace equation is linear, it is more convenient to first obtain the central gate capacitance, $C_c(x)$, by considering $(V_c, V_b) = (1, 0)$ V, and back gate capacitance, $C_b(x)$, by considering $(V_c, V_b) = (0, 1)$ V. For arbitrary gate voltages, the calculated $C_c(x)$ and $C_b(x)$ allow us to obtain the carrier density profile, $n(x)$, using equation (35), which explicitly reads

$$n(x) = \frac{C_c(x)}{e} V_c + \frac{C_b(x)}{e} V_b \tag{36}$$

here. When the quantum correction is considered, the net carrier density for the present example is, based on the formulas in [81] as well as [85], given by

$$\tilde{n}(x) = n(x) + \Delta n(x) \tag{37}$$

where $n(x)$ is the classical contribution, equation (36), and

$$\Delta n(x) = \mathrm{sgn}(n(x)) n_Q(x) \left(1 - \sqrt{1 + 2\frac{|n(x)|}{n_Q(x)}}\right) \tag{38}$$

is the quantum correction. The term n_Q in the above equation (38) given by

$$n_Q(x) = \frac{\pi}{2}\left(\frac{\hbar v_\mathrm{F}}{e} \frac{C_c(x) + C_b(x)}{e}\right)^2 \tag{39}$$

arises due to quantum capacitance and is generalization of the uniformly single-gated case of [79]. From equations (37)–(39), it can be seen that $\tilde{n}(x)$ differs significantly from $n(x)$ either when $n(x)$ is small or when $n_Q(x)$ is large. The former generally occurs whenever the carrier density in graphene is low, and the latter corresponds to large gate capacitance due

to, for example, thin dielectric layers. The carrier density correction based on the quantum capacitance model has been shown in [81] to be equivalent to that by self-consistently solving the Poisson equation with graphene's density of states (equation (8)) taken into account; see also [86].

The bottom panel of figure 9(c) shows spatial profiles of the classical carrier density $n(x)$, equation (36), considering various V_c at a fixed V_b (values specified in the caption of figure 9(c)). Curves of $\tilde{n}(x)$ based on equations (37)–(39) appear almost the same as $n(x)$ and are not shown here. The inset of figure 9(c) shows $\tilde{n}(x=0)/n(x=0)$. As expected, the quantum correction is negligible in this example of suspended graphene whose gate capacitances are generally small, except for central gate voltage values around $V_c \approx 1.09$ V which makes $n(x=0)$ close to zero.

Because of the negligible Δn in the present example, the following discussion about the onsite energy profile considers only $n(x)$. Since the length scale of the variation of the carrier density is much larger than the atomic scale as seen in the examples shown in figure 9(c), it is legitimate to assume that the energy-carrier relation equation (11) is locally fulfilled. Therefore, considering the local energy band offset defined as

$$V(x) = -E(n(x)) = -\mathrm{sgn}(n(x))\,\hbar v_\mathrm{F}\sqrt{\pi|n(x)|}\,, \qquad (40)$$

which is the onsite energy term in equation (30), the global Fermi energy for the entire graphene sample is expected to be fixed at zero. In short, using equation (40) in the above introduced quantum transport, the transmission equation (34) should be evaluated at $E=0$.

2.5.3. Scalable tight-binding model. From section 2.5.1, we have seen that the matrix size of equation (29) mainly depends on the number of atoms (or the lattice sites) composing the lattice under consideration. In the present spinless case of equation (29) with only one p_z orbital per atom considered, the H_0 thus represented is an $N_s \times N_s$ square matrix. Using the unit cell area $|\mathbf{a}_1 \times \mathbf{a}_2| = \sqrt{3}a_c^2/2$, it can be shown that the number of carbon atoms is about 38 millions per $\mu\mathrm{m}^2$, which is the typical order of magnitude of the sample area used in transport experiments. Dealing with $N_s \times N_s$ matrices with $N_s \sim 10^7$ is not a simple task. When the spin degree of freedom or other orbitals are taken into account, the size of H_0 may be further doubled, tripled, or even more.

For graphene, luckily the lattice spacing a and the nearest-neighboring hopping t appear in the low energy dispersion equation (3) simply as a product; see equation (4). Therefore, by considering a honeycomb lattice of lattice spacing $\tilde{a} = s_f a$ and nearest neighbor hopping energy $\tilde{t} = t/s_f$, its low-energy dispersion proportional to $\tilde{t}\tilde{a} = ta$ is guaranteed to be the same as that of real graphene. This scaling approach first introduced for spinless monolayer graphene in [87] led to the possibility of simulating micron-sized graphene samples [27, 75, 85, 88–105] and therefore made quantum transport simulations for ballistic graphene a very powerful tool. Moreover, the approach is compatible with spin–orbit coupling [106] as applied in a recent work on spin-dependent transport in graphene on WSe_2 [107], and can also be applied to bilayer graphene as was remarked in [87] and applied in [105, 108].

2.5.4. Periodic boundary hopping. Previously, in section 2.3.2 we have mentioned that the angle-resolved transmission can be numerically computed by the tight-binding approach. For such calculations, the real-space Green's function method described in the above section 2.5.1 remains the same, except that equation (29) for H_0 needs to be modified, in a way to allow hopping between, for example, upper and lower edge sites, modulated by the Bloch phase. Such so-called periodic boundary hopping terms arise from the Bloch theorem [68, 76, 109] because of the assumed translational invariance along the lateral dimension, as briefly explained below.

Consider a graphene lattice arranged with the zigzag direction along the x-axis and assumed to be infinitely extending along the $\pm y$ direction, as sketched in figure 10(a), where a minimal supercell with periodicity $w = 3a$ is highlighted in black. Let the y coordinate of the bottom edge sites within the supercell be y_b and top edge sites be y_t. Now, consider a certain x coordinate, say x', which aligns with a pair of bottom and top edge sites of the supercell, one at (x', y_b) and one at (x', y_t). At $(x', y_t + a)$, there is another lattice point which is a nearest neighbor to (x', y_t); see figure 10(a). If the wave function at (x', y_b) is $\langle x', y_b|\psi\rangle$, then according to the Bloch theorem, $\langle x', y_t + a|\psi\rangle = \mathrm{e}^{\mathrm{i}k_y w}\langle x', y_b|\psi\rangle$, because $y_t + a - y_b = w$ is exactly one period. Multiplying both sides of the equation by $|x', y_t\rangle$ from the left, canceling $|\psi\rangle$, and moving the phase factor to the other side, we have

$$|x', y_t\rangle\langle x', y_b| = \mathrm{e}^{-\mathrm{i}k_y w}|x', y_t\rangle\langle x', y_t + a|\,. \qquad (41)$$

Since $|x', y_t\rangle\langle x', y_t + a|$ on the right-hand side represents the nearest neighbor hopping, the above equation (41) indicates that the hopping from the bottom edge to top edge site can be described by t multiplied by the Bloch phase $\mathrm{e}^{-\mathrm{i}k_y w}$. From the Hermitian conjugate of equation (41),

$$|x', y_b\rangle\langle x', y_t| = \mathrm{e}^{+\mathrm{i}k_y w}|x', y_t + a\rangle\langle x', y_t|\,, \qquad (42)$$

we see that the hopping from the top edge to bottom edge site can be described by t multiplied by the Bloch phase $\mathrm{e}^{+\mathrm{i}k_y w}$. Equations (41) and (42) illustrated by figure 10(b) are what we call periodic boundary hopping, which greatly reduces the size of a tight-binding model Hamiltonian for an infinitely extending graphene from $(\infty \times \infty)$ down to $(4N_x \times 4N_x)$ where N_x ($= 11$ in the exemplary sketch of figure 10(b)) is the periodicity along the x axis.

Now that the periodic boundary hopping terms contain k_y, the tight-binding Hamiltonian becomes k_y-dependent, i.e. $H_0 = H_0(k_y)$. Because of the k_y dependence of the H_0, the lead self-energies, the effective Hamiltonian equation (31), retarded Green's function equation (32), the broadening matrices equation (33), and the transmission function equation (34) all contain the k_y dependence. In terms of the incidence angle, $\theta = \arcsin(k_y/k)$, the numerically computed

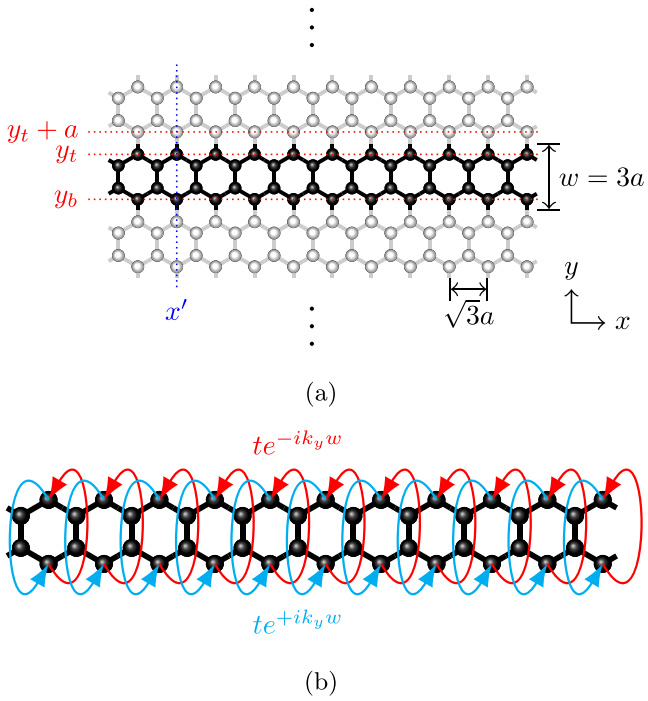

Figure 10. (a) Schematics of a graphene lattice, which is oriented with the zigzag along the x-axis and assumed to be infinitely extending along the $\pm y$ direction. (b) The equivalence of (a) but restricted to a minimal zigzag graphene ribbon with periodic boundary hopping arising from the Bloch theorem.

$T(k_y)$ can be plotted as $T(\theta)$ as shown in figure 6. Note that despite the different primitive description of the graphene lattice here (figure 10(a)) compared to the standard hexagonal lattice (figure 2(a)), the k_y introduced in the Bloch phase $\exp(\pm i k_y \cdot 3a)$ is the same as that in, for example, figure 2(f)[9].

In addition to the angle-resolved transmission, the method of periodic boundary hopping is also very useful for quasi-one-dimensional two-terminal graphene device, such as the example of figure 9(a) where W is sufficiently large. In such cases, the onsite energy $V(x)$ is one-dimensional, and $T(k_y)$ can be numerically computed. Integrating over k_y and using equation (26), the conductance thus obtained is consistent with the one computed using a finite-width ribbon, but the computation is much lighter and faster. In the recent work about gate-controlled one-dimensional superlattice in graphene, the two kinds of computations were explicitly compared [100], and the results are hardly distinguishable.

In the literature, the first work applying this method to reproduce the features of the experimentally measured conductance was [109], revisiting the experiment [22] showing the phase shift of Fabry–Pérot interference due to the Berry phase [25]. Subsequent applications include p-n junctions of suspended graphene [23], multiple p-n junctions of graphene on substrate [110], p-n-p junctions of bilayer graphene [108, 111], and large-angle decoupled twisted bilayer graphene [85, 112].

[9] When arranging the graphene lattice in the way that the armchair direction is parallel to the x-axis, the periodicity for the Bloch phase becomes $w = \sqrt{3}a$, the Dirac cones will not be centered at $k_y = 0$, and the relation between k_y and the incidence angle θ will be different.

2.6. Summary of useful formulas

Table 1 summarizes useful formulas for single-layer graphene, assuming uniform distribution of carrier density n. For symmetric graphene p-n junctions, useful formulas are summarized in table 2.

3. Fabricating clean graphene devices

The observation of electron optical phenomena requires high quality devices with ballistic transport where electrons can travel large distances without scattering processes. In 2DEGs buried below the surface record high mobilities were achieved, which allowed to perform electron optical experiments like magnetic focussing [113–116]. The special Dirac spectrum of graphene leads to protection against back-scattering events which promises large electron mobilities. However, in the first transport experiments rather low quality devices (at least compared to 2DEGs) have been realized with a mean free path on the order of 100 nm and mobilities on the order of few 1000 $\mathrm{cm}^2\,(\mathrm{Vs})^{-1}$ [1, 29]. It was soon realised that in these devices the mobility was limited by the charge traps in the SiO_2 that was used as a gate dielectric on silicon wafers [117] and by contamination of the graphene surface mostly originating from the fabrication process. Whereas the latter can be partially eliminated by cleaning the graphene surface with forming gas (or other gases) or by AFM cleaning [118, 119], for the former, separation of the graphene flake from the surface was required.

3.1. Suspended graphene

To achieve separation from the substrate the graphene flakes were suspended above the SiO_2 wafer. This was in the beginning done by etching away the SiO_2 with buffered HF solution, followed by a critical point drying step [17, 18]. First devices fabricated using this method reported mobilities on the order of 200'000 $\mathrm{cm}^2\,(\mathrm{Vs})^{-1}$. Later on the fabrication of top gates to suspended devices was achieved [114], which together with a doped Si substrate allowed the realisation of double gated high quality devices. Later, another method was developed by Tombros *et al* [120] and further extended by Maurand *et al* [121], where instead of etching away the SiO_2 below graphene, the flakes were transferred onto a sacrificial layer that was spin-coated on top of the Si/SiO_2 wafer. This sacrificial layer could be locally removed by electron beam lithography and liftoff without the need for critical point drying, and the contact material was not limited by the HF etching. This method could also be extended with top-gates, but was better suited for local-bottom gated structures. The fabrication method and examples of suspended devices are shown in figures 11(a)–(c).

The drawback of both methods was that after fabrication the graphene flakes were covered by resist residues and other contaminants, which had to be removed at low-temperature

Table 1. Useful formulas for single-layer graphene of uniform carrier density n and Fermi energy E, without and with the applied external magnetic field B perpendicular to the graphene sample.

Physical quantity	Formula	Equation number
Group (Fermi) velocity	$v = \frac{1}{\hbar}\frac{\partial E}{\partial k} = v_{\mathrm{F}} \approx 10^6\ \mathrm{m\,s^{-1}}$	
Wave vector	$k = \sqrt{\pi\lvert n\rvert}$	(10)
Energy	$E = \mathrm{sgn}(n)\hbar v_{\mathrm{F}}\sqrt{\pi\lvert n\rvert}$	(11)
Density of states per unit area	$D = \frac{2\lvert E\rvert}{\pi(\hbar v_{\mathrm{F}})^2}$	(8)
Cyclotron radius[a]	$r_c = \frac{\hbar k}{eB}$	(16)
Cyclotron frequency	$\omega_c = \frac{eBv_{\mathrm{F}}^2}{E}$	(18)
Magnetic length[a]	$l_B = \sqrt{\frac{\hbar}{e\lvert B\rvert}}$	
Nth Landau level energy	$E_N = \mathrm{sgn}(N)\sqrt{2e\hbar v_{\mathrm{F}}^2\lvert N\rvert B}$	(5)
Filling factor[a]	$\nu = \frac{nh}{eB}$	
Ballistic conductance of pristine graphene of width W	$G = \frac{e^2}{h}\frac{4W}{\pi}k = \frac{4e^2}{h}W\sqrt{\frac{\lvert n\rvert}{\pi}}$	(25)

[a] Valid also for other 2D materials.

Table 2. Useful formulas for symmetric p-n junctions of single-layer graphene.

Physical quantity	Junction type	Formula	Equation number
Angle-resolved transmission[a]	Abrupt	$T(\theta) = \cos^2\theta$	(21)
Ballistic conductance[b]	Abrupt	$G = \frac{e^2}{h}\frac{8W}{3\pi}k = \frac{e^2}{h}\frac{8W}{3}\sqrt{\frac{\lvert n\rvert}{\pi}}$	(27)
Angle-resolved transmission[a]	Linear[c]	$T(\theta) = \exp\left(-\pi\frac{kd}{2}\sin^2\theta\right)$	(22)
Ballistic conductance[b]	Linear[c]	$G \approx \frac{e^2}{h}\frac{2W}{\pi}\sqrt{\frac{2k}{d}}$	(28)

[a] Of incidence angle θ.
[b] Of graphene sample width W.
[c] Of smoothness d; see figure 6.

by passing a large current through the device (current annealing). This process allowed the realization of ultra-high quality devices, however led to a substantial decrease of fabrication yield. For complicated devices with multiple contacts and graphene flakes that are shaped to a certain form, the yield became extremely low. Moreover, these devices were hard to clean homogeneously and residues could accumulate close to the contact or at the samples edges [122]. It was also shown, that substantial strain can be accumulated in suspended graphene structures (also from the current annealing), which was demonstrated via mechanical oscillation measurements [123].

3.2. Graphene-hBN heterostructures

The next breakthrough came when Dean *et al* demonstrated that another 2D crystal, hBN, could be an ideal substrate for graphene devices [19]. First of all, hBN could be exfoliated similarly to graphene, and due to the 2D nature of the crystal an atomically smooth interface could be achieved between graphene and hBN, as demonstrated by TEM studies [124]. Second, hBN is an insulator with a large bandgap and can be used as a gate dielectric. The high quality hBN crystals separated the flakes from the SiO_2 substrates and allowed the formation of high quality devices with mobilities similar to the suspended ones. The hBN crystals grown by T. Tanaguchi and K. Watanabe led to a revolution in the field and now they are central building blocks of 2D heterostructures. In these heterostructures, where graphene was placed on top of an hBN flake, the top surface was usually cleaned with forming gas or AFM [19]. In a next step it was also shown that the graphene devices can be fully encapsulated between hBN flakes [21], where the devices were made with the pick-up method shown on figure 11(d). The method relies on van der Waals interaction between 2d crystals and allows to pick up flakes from a substrate using another one, leading to the fabrication of not only hBN/Gr/hBN, but more complex heterostructures. The atomically clean interfaces were once again demonstrated by TEM measurements [21] and also signalled by the high-quality transport experiments. Since the graphene is encapsulated between hBN crystals prior to fabrication, in order to fabricate electrical contacts, an etching step was performed which exposed the edge of the device and allowed the fabrication of 1D edge contacts which worked surprisingly

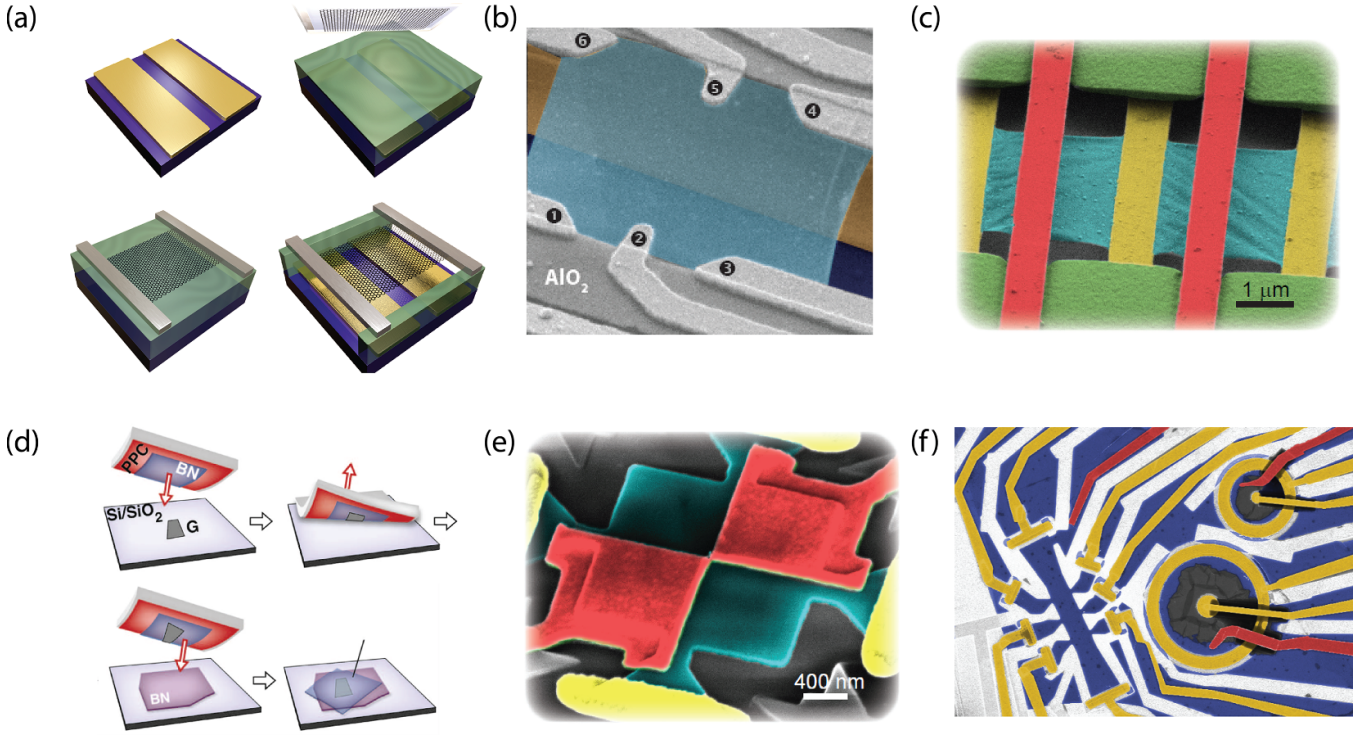

Figure 11. High mobility graphene devices. (a) Suspended graphene devices realised by selective removal of a sacrificial LOR polymer layer. (b)–(c) Graphene suspended devices with complicated structure were demonstrated, with several contacts and bottom gates (b) or even with suspended topgates. Images (a) and (b) are from [121], (c) from [69]. (d) Encapsulating graphene with h-BN lead to high mobility devices and allowed a higher yield in fabrication [21]. Using these methods complicated gate structures and device architectures can be realized. Figure (e) shows a graphene heterostructure with local top-gates allowing the formation of a beam-splitter in magnetic field based on classical snake states, whereas panel (f) shows a Hall-bar and Corbino geometry from encapsulated bilayer graphene. Image (e) is from [69], (f) is from C. Schönenberger, S. Zihlmann and coworkers. (a) and (b) Reprinted from [121], Copyright (2014), with permission from Elsevier. (d) From [21]. Reprinted with permission from AAAS. (c) and (e) Reproduced with permission from [69].

well, with low contact resistance. This method was further extended/altered by later works [125–130] and is the standard fabrication technique for most research groups.

An important advancement in reaching high quality devices was the introduction of graphite gate electrodes. It was found that in this case potential fluctuation from the substrates was further removed in graphite/hBN/Gr/hBN/graphite devices [131–133]. The decrease of potential fluctuations was confirmed in scanning SET measurements as discussed in more detail e.g. in [134]. Finally, very recently a novel transfer method based on silicon cantilevers has been developed for the fabrication of vdW heterostructures [135]. This allows polymer-free transfer and a compatibility with UHV based fabrication for extremely air-sensitive materials. This methods leads to ultra-clean devices and a very fast fabrication procedure.

The advent of encapsulated devices gave a new boost for electron optical experiments, since the device architectures could become much more versatile compared to suspended devices, as shown by examples in figures 11(e)–(f).

3.3. Device characterization

The quality of graphene devices is usually characterised by field effect mobility. This is extracted from conductance vs. density plots, often by dividing or by derivating the conductance by density. Other methods rely on fitting the conductance vs. density dependence with a formula taking into account contact resistance as well (for two terminal measurements), short range scattering, residual doping around the CNP and a given form of density dependent mobility (often constant). Some typical results are demonstrated on figure 12. The fitting procedure with the equation $\sigma^{-1} = \rho_c + (\mu e\sqrt{n_*^2 + n^2})^{-1}$ for an encapsulated device is shown in figure 12(a), where a doping independent mobility μ is supposed originating from scattering either on charged impurities or from strain fluctuations. ρ_c is the contact resistance and n_* is the residual doping. The field effect mobility can be converted into a mean free path, which determines the length-scale on which electron-optical experiments can be performed. Though this depends on the density, in high quality devices this can reach from a few micrometres up to 20-30 micrometres by now [24, 135, 136].

For low energy experiments performed close to the CNP, another quantity, the residual doping n_* is important. This quantifies the cut-off lowest density that can be achieved in the device, below which an inhomogenous doping profile forms with electron–hole puddles. The lowest values that can be reached were around below $10^9\,\mathrm{cm}^{-2}$ demonstrated in suspended devices [75, 137, 138]. This is often extracted from log-log conductance-density plots, see also figure 12(b) for an

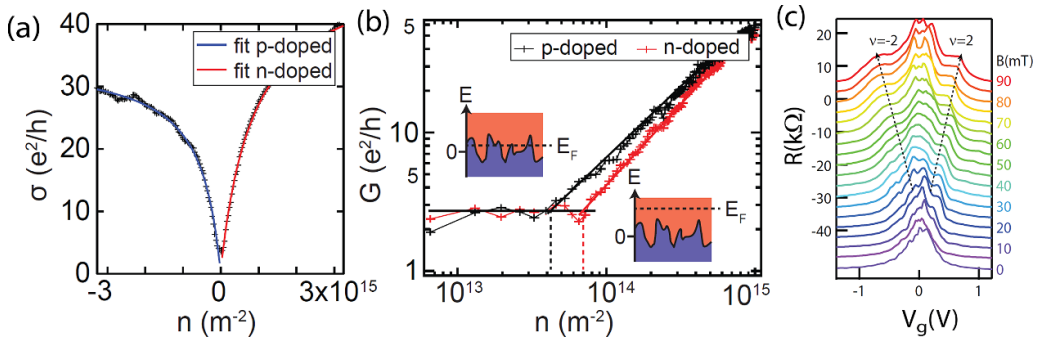

Figure 12. Standard characterization of high mobility samples. (a) Conductivity versus carrier density (with fitting procedure described in the text). (b) Conductivity versus carrier density in a log log plot shows a saturation corresponding to a residual doping at charge neutrality of about 5×10^9 cm^{-2} (c) Resistance versus back-gate voltage at finite field showing quantum Hall plateau emerging at field as low as 50 mT which demonstrates the high quality of the device. (a)–(c) Reproduced with permission from [69].

example. Finally device quality can also be inferred from the magnetic field at which Shubnikov de Haas (SdH) oscillations appear. This leads to another lifetime, the quantum lifetime, which is susceptible to small angle scattering as well. This contrasts with the momentum scattering time, which is more sensitive to backscattering events involving large momentum changes. The SdH oscillations can appear in a few tens of milliTeslas, and in figure 12(c) a well-developed quantum Hall plateau is observed already at 50 mT. The splitting of Landau level degeneracy also signifies high quality devices, however the strength of the electronic interactions also matter, which could also depend on the device architecture, e.g. on the distance of screening gate electrodes [112, 139–142]. Finally, other time-scales that are usually longer than the momentum scattering time are intervalley-scattering, phase coherence or spin-relaxation time can also be important for certain set of experiments.

We note, that device quality prior to experiments is often characterized by Raman mapping, where the distribution of peak width can give information of strain and doping variation within the sample [143].

To sum up, since the invent of graphene the device quality has evolved immensely. From 100 nm of mean free path and close to 1000 cm^2 (Vs)$^{-1}$ mobilities now 10^6 cm^2 (Vs)$^{-1}$ mobilities can be reached. In state-of-the art devices, one limiting factor for the mobility could arise from strain fluctuations, but for the best devices scattering on the edges of the device limit the mobility [128, 136, 144, 145] (seen as saturation of mobility at large densities). In [135] it was shown that mobilities close to 3×10^6 cm^2 (Vs)$^{-1}$ and mean free path corresponding to 18 μm is reached. More importantly, the mobility does not saturate at large densities, therefore the authors suggest, that in their case not the sample size is the limiting, but, carbon and oxygen substitutional impurities intrinsically present in the hBN. At higher temperatures phonons start to limit the mobility (for suspended devices out-of plane phonons become important). However, since most experiments we report on are carried out at low temperatures, the detailed analysis of this goes beyond the scope of our review.

An amazing advancement in device quality was also achieved in CVD and epitaxial graphene systems. For CVD graphene ballistic transport via magnetic focusing [146] and bend resistance measurements have been shown up to 28 μm [24], see section 4.1 in detail. Besides obtaining large single crystal domains it was also important to use an hBN substrate [147] or full encapsulation [148, 149] to reach high mobilites, and even a pickup technique from growth Cu substrate was demonstrated [150]. In epitaxial graphene nanoribbons ballistic transport was reported [151] even up to 16 μm [152] and in annealed edges of epigaphene up to 50 μm [153].

4. Electron optics experimental toolbox

4.1. Magnetic focussing

4.1.1. Bend resistance. One of the first signatures of ballistic transport on the micron-scale came from Hall crosses in hBN encapsulated devices [113], as shown in figure 13(a). In the experiment, a voltage is measured between terminal 3 and 4, the current is injected at contact 2, while contact 1 is grounded. The voltage–current ratio yields the bend resistance. In zero magnetic field a large negative resistance was observed originating from straight trajectories from contact 2 and 4. In perpendicular magnetic fields, however the trajectories start to bend, as described in section 2.2.1 and electrons are guided towards contact 3 leading to a crossover to positive bend resistances. These measurements suggested ballistic transport up to 3 μm. With the development of device quality similar negative bend was observed but now on the 30 μm length scale [24].

4.1.2. Focussing experiments. Similar physics arises in Hall-bars in magnetic focusing experiments, as shown in graphene for the first time by Taychatanapat *et al* in [114]. As shown on figure 13(b), one of the side electrodes of the Hall-bars are used as electrons injectors, whereas on a neighbouring electrode the increase of the electrochemical potential is measured as a result of electron trajectories hitting the electrode. In magnetic fields the electrons follow circular trajectories, and if twice the cyclotron radius matches the distance of the con-

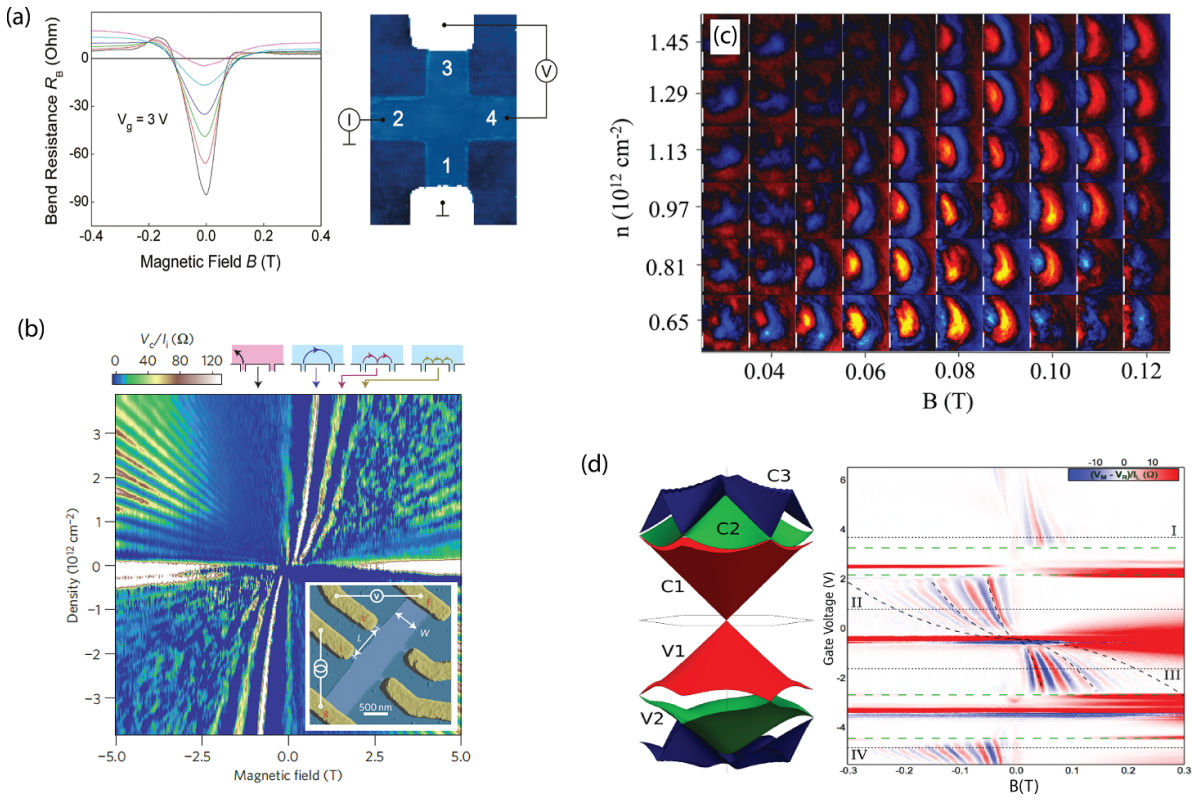

Figure 13. Ballistic electron propagation in high mobility devices. (a) Mayorov *et al* demonstrated in [113] negative resistance vanishing with magnetic field in a non-local measurement, consistently with a device size limited mean free path. (b) Selective focusing of electron trajectories with up to three specular reflections on the sample edge was demonstrated soon after [114]. (c) The cyclotron orbits were directly imaged in [115] with a scanning gate microscope. (d) Lee and coworker were able to observe magnetic focusing originating both from the usual graphene bands (main panel) as well as the magnetic focusing of the mini bands originating from the moire potential between graphene and h-BN. The band structure modification is shown on the left [116]. (a) Reprinted with permission from [113]. Copyright (2011) American Chemical Society. (b) Reproduced from [114], with permission from Springer Nature. (c) Reprinted with permission from [115]. Copyright (2016) American Chemical Society. (d) From [116]. Reprinted with permission from AAAS.

tacts, an increased voltage is observed. The cyclotron radius given in equation (16) can be rewritten as

$$r_c = \hbar k/eB = \hbar\sqrt{n\pi}/eB, \tag{43}$$

therefore both magnetic field and the electron density tunes the resonance condition. As a result these focusing resonances show up as dispersing lines in the measured voltage in gate-B-field maps, as shown in figure 13(b) for positive gate voltages and magnetic fields. The focusing peaks also show up at negative gate voltages (for holes), however for opposite magnetic fields compared to positive densities. This is the result of opposite group velocity and hence chirality in the electron and hole band for given momentum. The dashed line shows the focusing conditions based on equation (43), which matches quite well the measurements. Note that for the correct peak positions the valley degeneracy has to be taken into account. In the real experiments the electrons are injected under an angular distribution, however their majority will still focus to the same position along caustics. The focusing trajectories have been imaged using scanning gate microscopy [115, 154, 155] and an example is shown in figure 13(c), which nicely demonstrates their tunability using magnetic fields and gate voltage.

4.1.3. Higher order focussing. A focusing condition can also be reached if the electrons bounce on the side of the sample. These account for higher focusing peaks, whenever $2r_c \times j = L$, where j is an integer. The visibility of higher order peaks depends on the sample quality (mean-free path) and on the specularity of the interface on which the trajectories are scattered. A disordered edge leads to the randomization of reflection angles and to the loss of visibility for higher order focusing peaks. This has been very recently investigated in BLG [156], where the edge was realised by electrostatic gating opposite to etched single layer devices, see in more detail figure 19(b) in section 4.4.1. It was found that in this case the smoother edge potential leads to a specular reflection demonstrated by the high visibility of higher order focusing peaks. We note here that the magnetic focusing has also been applied in a special setting [155], where the edge of the graphene, on which the charge carriers bounce, was replaced by a superconducting electrode. In this case due to Andreev reflection,

instead of electrons, holes can reach the detector leading to a reversed sign for the second focusing peak. In general, by investigation of the temperature dependence of the focusing signal (the weight of the focusing peak) it was found that it cannot be explained by thermal broadening of the injected electrons' momenta. It was found from these experiments that at low temperature electron-electron interaction dominates the momentum scattering time with T^{-2} dependence.

We note that the magnetic focusing/bend resistance experiments only give indications for partial ballistic transport. E.g. if one detects a negative bending resistance it indeed indicates that there is a fraction of electrons with a large mean-free path on the length scale of the trajectory. However, if this bending signal is small, it could still mean that most electrons have suffered an elastic scattering event before. So alone a negative bend resistance does not prove a ballistic mean-free path that equals the size of the sample. The mean-free path has a distribution which could be quite wide. In order to quantitatively give a number, one needs a particular model that yields a forecast to the distribution. Only with such a model is it possible to make a connection between the observed magnitude of the negative bending signal and the mean elastic scattering length.

4.1.4. Revealing the band structure. Finally, magnetic focusing is a sensitive tool to probe modification of the band structure and the Fermi surface. In a recent example the splitting of the graphene Fermi surface was realized by inducing spin-orbit interaction in graphene that is placed on a WSe_2 substrate [107]. This led to a splitting of the Fermi surface and to signatures of splitting in the focusing peaks. Another example is coming from graphene/hBN structures, where hBN is aligned with the graphene lattice which imposes a superlattice on graphene and leads to strong modification of the band structure, as shown in figure 13(d). As a result of the band structure modification mini-bands with secondary CNPs appear. The focusing peak position will be sensitive to the band structure and in this case several transitions between electron and hole-like carriers have been observed [116], as shown in figure 13(f). These measurements therefore give an important tool in the mapping of the band-structure modifications of graphene heterostructures. Another work investigated the case of twisted bilayer graphene where similar transitions from electron to hole Fermi surfaces have been found [158]. Moreover, in [159] ballistic valleycurrents have been reported in SLG/hBN superlattice, whereas in [136] negative bend resistance measurements of Brown-Zak fermions have been shown.

4.1.5. Focussing in p-n junctions. Chen *et al* used a transverse focusing setting through a p-n junction to verify Snell's-law both in the unipolar (n-n') and the bipolar (p-n) regime. This is shown in figure 14(a), where the doping on the left and right side of the junction can be tuned using two separate gates. These allow to generate a homogeneous doping with circular trajectories (panel (c), top cartoon) or distorted trajectories by having different dopings (but with the same carrier type) on the two sides (middle cartoon), and even situations when the doping is opposite on the two sides (bottom sketch). In this case, the trajectories on the p-side bend in the opposite direction due to the opposite group velocity (see section 2.2 or [71]), and the carriers are focused to an opposite terminal leading to a sign change in the voltage. The measurements are shown in panel (b) for fixed doping on the left side, as a function of right doping and magnetic field. For negative gate voltages the focusing signal can be well fitted (see dashed lines) by trajectories similar to the one shown in panel (b)). Moreover, for positive gate voltages the focusing through a p-n junction is observed. By tuning the magnetic field and the gate voltage on the left side the incidence angle of the carriers to the p-n junction can be set. To achieve the focusing condition the gate voltage on the right side is tuned, which also determines the angle of the electrons refracted through the junction. The refracted angle multiplied with the momentum as a function of the same quantity on the left side is plotted in figure 14(d), verifying Snell's law given in equation (20). Finally, the intensity of the focusing peaks can also be used to determine the angle dependent transmission through a p-n junction, which is shown in panel (e). The measurements can be well reproduced with a model of a graded p-n junction with a width of 70 nm.

4.2. Electron optical elements

4.2.1. Electron guiding. In section 2.3 we have seen that the reflection and refraction properties of n-n' and p-n junctions depend on the densities, hence are gate tunable. Using this with local gating different electron optical devices can be engineered. The critical angle of reflection is used to keep photons inside optical fibres and a similar guiding experiment has been engineered also in multiterminal suspended devices [88]. A false-colored SEM image of the device is shown in figure 15, where the local gates below the graphene allow to tune the electron density in the outer regions and in the central channel, marked with dashed lines, separately. This allows the formation of n-n'-n, n-p-n junctions. The injectors and detectors of the channel are the suspended narrow electrodes, whereas the large electrodes are used to measure the loss. In panel (b), we show by red the density regions where optical fiber guiding originating from total internal reflection is expected. Moreover, as soon as a p-n junction is formed (marked by the striped region), the guiding is expected to become more effective due to the larger reflection probability in smooth p-n junctions if the electrons do not arrive close to perpendicular to the junction. Finally for narrow channels, the appearance of mode-by-mode filling is possible, as shown by the blue regions. The experiment shown in panel (c) shows strong resemblance to the expectation with guiding efficiencies close to 50%. The experiments were reproduced by tight-binding based calculations and even signatures of mode filling were observed. The guiding efficiency was

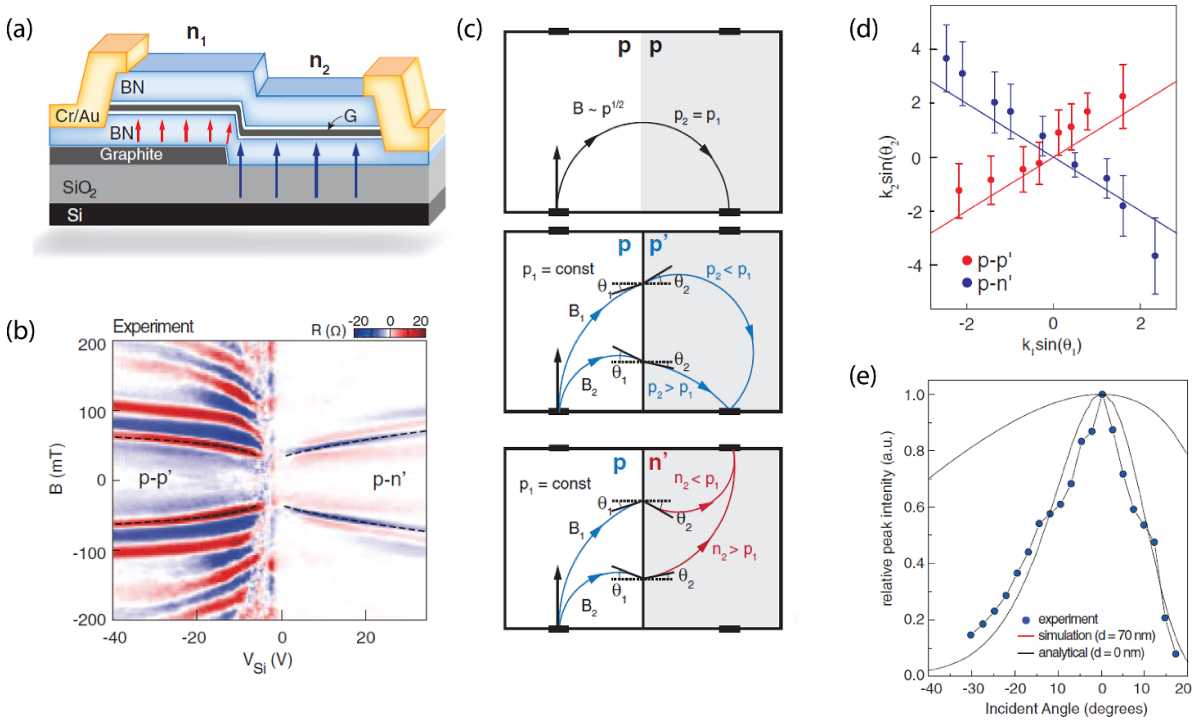

Figure 14. Snell's law across p-n junction in ballistic graphene device. (a) Schematic of the h-BN encapsulated graphene device: a local graphite gate below half of the device is used to create a p-n junction, the carrier density in the rest of the device is controlled by the Si backgate. (b) Non-local resistance shows focusing peak similar to the one in figure 13, instead of being reflected on the sample edge as in figure 13, the charge carriers are here deflected by the p-n junction. (c) schematic of electrons trajectories for different carrier densities. (d) The estimated outgoing angle versus incident angle (dots) follow the Snell's law (blue and red lines). (f) Focusing peak signal versus incidence angle (dots), fitted by a simulation for a 70 nm wide p-n junction. From [157]. Reprinted with permission from AAAS.

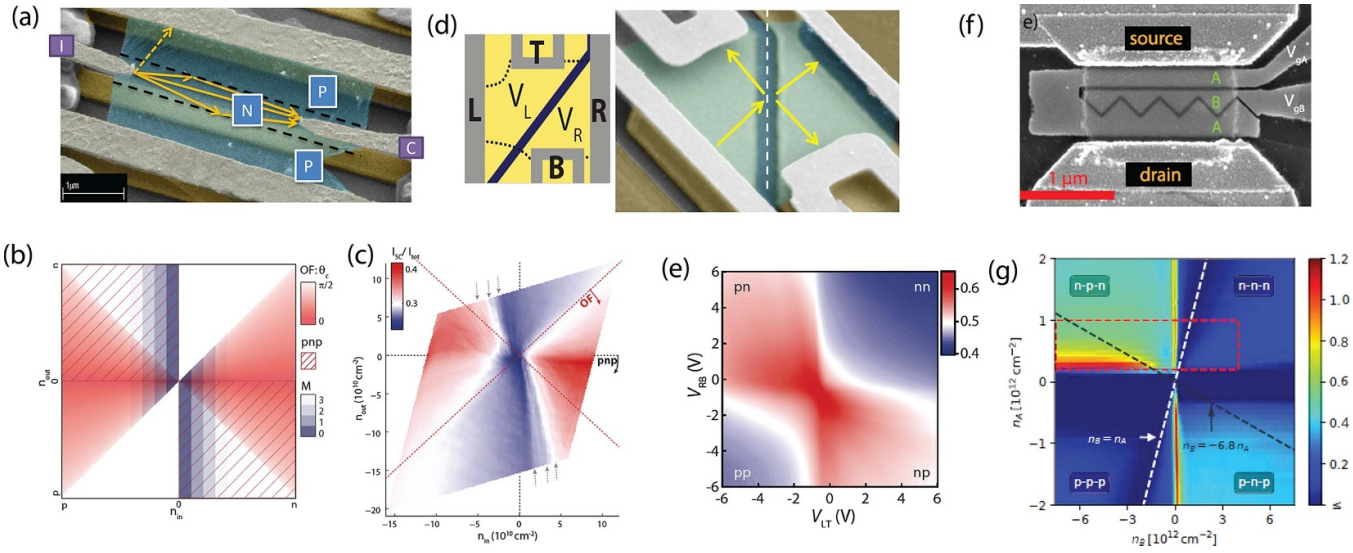

Figure 15. Electron-optics building blocs. (a) False colored electron optical image of a suspended graphene sheet where carrier density is tuned locally such to mimic the behavior of an optical fiber. (b) Different regions for device operation as function of channel and bulk carrier densities, marking regions of optical fiber guiding, p-n guiding and mode filling. (c) Measured transmission reproducing well the expectations shown in panel (b). (d) False colored electron optical image of a suspended graphene devices with local gates splitting the graphene sheet into two regions and effectively creating an electronic beam splitter between different contacts. (e) Current reflected from the beam splitter towards terminal T (normalised to the injected current) as a function of both local carrier densities. The reflection efficiency increases as the p-n junction is formed. (f) corner reflector, (g) resistance of the corner reflector as a function of carrier densities in the B (horizontal axis) and A regions (vertical axis). (a)–(c) Reprinted with permission from [88]. Copyright (2015) American Chemical Society. (d) and (e) Reprinted from [89], with the permission of AIP Publishing. (f) and (g) Reproduced from [160]. CC BY 4.0.

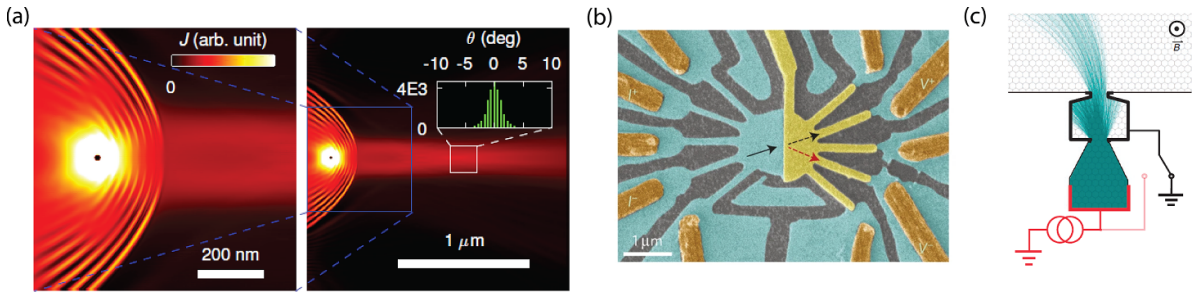

Figure 16. Electronic flow collimation. (a) Electron collimation based on a pointlike source at the focal point of a parabolic interface separating two regions with opposite charge carrier densities. Calculation shows small scale and large scale current distributions. In the inset this current density analyzed for the white box area. The beam is collimated on the scale of the electronic wavelength. Reprinted (figure) with permission from [92], Copyright (2017) by the American Physical Society. (b) Electron collimation based on etching the graphene to specific shape [164]. (c) Pinhole configuration used to generate a directional beam in [165]. (b) Reproduced from [164], with permission from Springer Nature. (c) Reproduced from [165]. CC BY 4.0.

limited by electrons injected perpendicularly from the side of the contact to the interface (see dashed arrow), which could then easily reach the large electrodes via Klein tunnelling. With proper shaping of the devices and the versatility of hBN encapsulated device architectures higher efficiencies could be reached now.

4.2.2. Tunable-beam splitters and reflectors. The angle-dependent transmission was also used to make a gate tunable beam-splitter [89]. The device architecture is shown in figure 15(d). The electrons are injected from electrode L, the current is measured on the rest of the terminals and tilted gates are used to realise a junction tilted with respect to the injected current. The percentage of the current measured at the top contact in the bipolar region (p-n, n-p) clearly increases compared to the unipolar region (n-n or p-p) case, as demonstrated in panel (e). It was found that most of the current is diverted to the top contact when a p-n junction is formed. This study was followed by studies on similar architectures, where even higher tunability was demonstrated [161, 162]. The geometry shown on figure 15(f) relies on similar principles [160, 163]. In the corner-reflector devices the source and the drain is connected by two gates: gate A used for collimation and gate B used as the reflector. The principle is similar to that of a prism, however here the refractive index of the inner and outer region are gate tunable. The measurements from [160] are shown in panel (f). The reflector works in the n-p-n regime, for large densities within region B. In this case, resistance larger than in the CNP region can be reached. Limitations on the visibility come from residual scattering mechanism (here phonons), since electrons which do not arrive perpendicularly to the interface need to traverse several times within the prism, which leads to enhanced scattering probability.

4.3. Collimation and lensing

4.3.1. Collimation using p-n junctions. For the experiments above the collimation effect of a p-n junctions was important. As shown in section 2.3.2 and demonstrated on figure 14(a) smooth p-n junction only transmits electrons under small incidence angles. Smooth p-n junctions are easy to realize in suspended samples, where the gate distance is large. However, for several experiments, this has to be combined with sharp p-n interfaces, which poses technical challenges. An improved version of p/n collimation have been suggested by Liu and coworkers in [92]. Specifically, by combining negative refraction and Klein collimation at a parabolic p-n interface, highly collimated, non-dispersive electron beams can be engineered, which stay focused over scales of several microns, as shown in figure 16(a). Such 'beams of electron waves' can be bent and steered by a magnetic field without losing collimation, see figure 20. This provides a setup for observing high-resolution angle-dependent Klein tunneling and high-fidelity transverse magnetic focusing [166].

This setting is based on feeding charge carriers through a point-like source (vertically) into the system. Indeed, such sub-100 nm point contacts have already been experimentally realized in graphene [167]. However, the intensity of the created beams suffers from the fact that only an angular segment of the isotropically emitted wave is collimated. Enclosing the point source by a cavity to collect such losses should, in principle, allow for strongly enhancing the beam intensity.

4.3.2. Geometrical collimation. Other methods to generate collimated beams are shown in panels b and c of figure 16. In panel (b) the geometrical shaping of the devices is used to make narrow injector contacts [164]. This allows a well-defined injection angle to the central region and the p-n junction that is realized at the boundary of the yellow gate. In such architecture the injector part has to be ballistic as well, which puts more serious constrains on the device quality. Moreover, the edge of the injector part of the devices often suffer from edge roughness due to the etching procedure used to define them, which leads to random scattering and hence can randomize the outgoing electron trajectories close to the injection point. A solution for this problem is shown in figure 16(c),

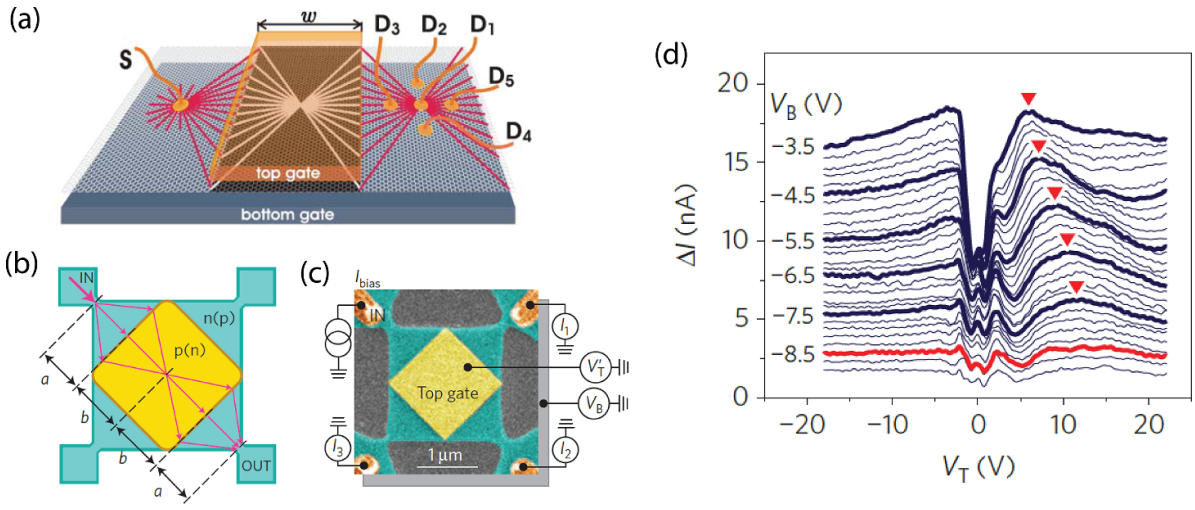

Figure 17. Negative refraction and Veselago lensing. (a) Theoretical concept of a graphene based Veselago lens using negative refraction. (b) Experimental design with electron trajectories traced in red. (c) False colored scanning electron microscope of the device. (d) Constant current is injected from top left contact and the collected current at bottom left contact is measured. Background (taken at $V_b = -9.5\,\mathrm{V}$) is substracted. Red triangles indicate current enhancement. (a) From [10]. Reprinted with permission from AAAS. (b)–(d) Reproduced from [164], with permission from Springer Nature.

where the side of the injector contact is used to drain the electrons that are not injected under a narrow angular distribution [165]. Here the injection is done from the bottom of the injector-collimator element (shown in red), and after the constriction the black contact can be used to drain the uncollimated electrons. The viability of this method was tested using magnetic focusing experiments [165].

4.3.3. The Veselago lens. A very peculiar negative refraction property of p-n junction can also be used to make a 'perfect lens', called Veselago lens. In their early work Cheinaov and coworkers have suggested [10] that a flat p-n surface can be used to focus the trajectories originating from a point like source to a point like detector. This is shown in figure 17(a) where the trajectories originating from S source electrode are refocused to D1 after two reflection through the p-n junction. The experimental challenge lies in the formation of point like sources [167] and in the realization of sharp p-n interfaces. This is important, since as described in section 2.3.2.2, for smoother junctions only trajectories that are close to perpendicular to the junction are transmitted. The first signatures of the lensing was shown in [164] in a geometry shown in figure 17(b). The trajectories are injected through a constriction, which similarly to the proposal are twice refracted through a p-n junction. The SEM image of the device is shown in panel (c). The geometrical parameters of the device, a and b determines the density ratio at which the focusing to the drain ('OUT') electrode should happen. Weak signatures of this focusing effect were observed in the measurements shown in figure 17(d), the position where a weak enhancement is observed is marked by red arrows. The different curves correspond to different doping in the green region of the device, and for the position of the arrows the doping in the yellow region is set to the focusing condition. Later work have shown signatures of this lensing effect in interference experiments [169]. Other theory works considered focusing using circular p-n junctions and analyzed the appearing caustics and the viability of semi-considerations [170–172].

4.4. Anisotropic Fermi surfaces

4.4.1. Gate-defined electron guiding in ballistic bilayer graphene. Early designs of quantum nanostructures in mono- and bilayer graphene confined the charge carriers by physically etching the graphene sheet [173–175]. This method allowed to observe some quantum confinement effects in graphene, but introducing hard wall boundaries by etching is intrinsically flawed. Edge disorder and, consequently, randomly localised states along the sample edges are inevitable, leading to a loss of coherence and control of the charge carriers' degrees of freedom.

An alternative for confinement in bilayer 2D materials uses electrostatic gating [49–52]. In a bilayer lattice, an external electric field breaks the inversion symmetry and opens a band gap. Then, in the gapped device, e.g. two split gates may define a channel: adjusting the potentials of the gates tunes the Fermi energy into the conduction band within the channel region but into the band gap underneath the split gates, as shown in figure 18(a). This method of electrostatic confinement introduces smoother confinement potentials and avoids edge-induced device perturbations. Over the recent years, such gate-defined soft electrostatic potentials have developed into a formidable tool for electron confinement, steering, and control in bilayer graphene. Immense progress in sample quality and gating has enabled the demonstration of electron confinement and control in a series of gate-defined quantum

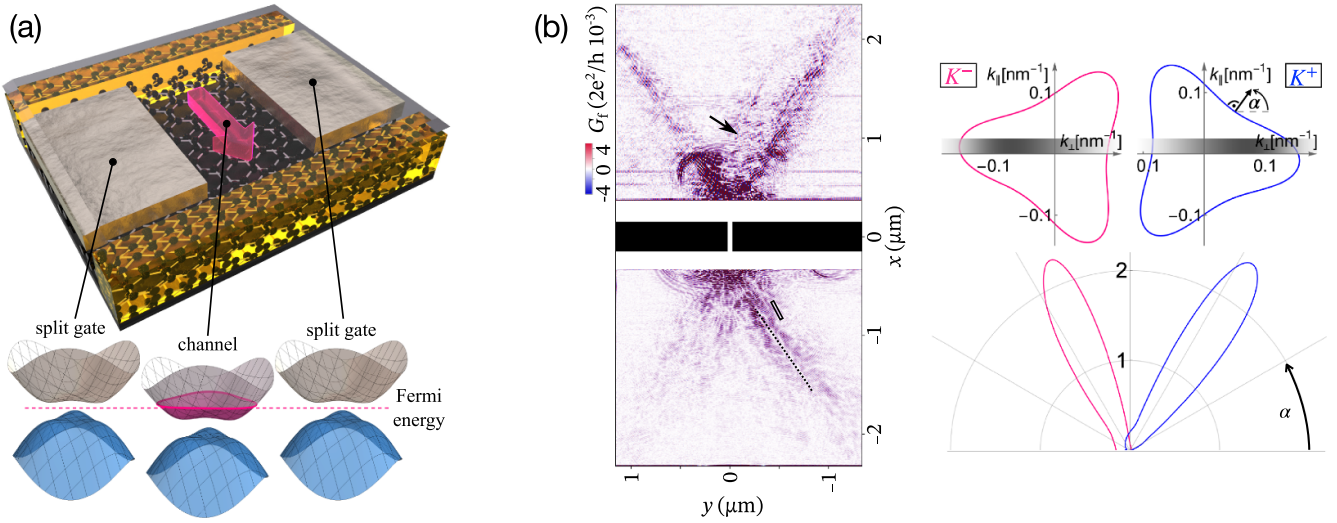

Figure 18. Electron guiding and anisotropic propagation in bilayer graphene. (a) Device schematic for electrostatic soft confinement and guiding in gapped bilayer graphene: Multiple gates locally modulate both the gap and the charge carrier density such that, e.g. the Fermi energy is within the band gap underneath the split gates, but in the conduction band in the centre, defining a 1D channel. (b) Collimated electron jets behind a gate-defined channel in gapped bilayer graphene. Left: spatial structure of electron flow in the bilayer graphene bulk on both sides of the channel measured by SGM. Right: the trigonally warped Fermi lines in bilayer graphene are anisotropic in both $K^{\pm}$ valleys, entailing an anisotropic, valley dependent velocity distribution of the charge carriers. The angle-dependent propagation probability is calculated here from the velocity distribution of the anisotropic dispersion weighted by the confined channel states within the four-band continuum model of bilayer graphene. Reprinted (figure) with permission from [168], Copyright (2021) by the American Physical Society.

nanostructures, including quantum wires [98, 156, 168, 176–180], quantum dots [181–196], and electron interferometers [197–199].

Due to the high quality of the gate-induced electrostatic confinement and the hBN-encapsulated bilayer graphene samples [24, 116, 158, 168] charge carriers in such confined structures often propagate in a largely ballistic manner and can be guided and controlled by virtue of the external gates.

4.4.2. Lowered rotational symmetry of the electronic structure and anisotropic charge carrier dynamics. The tunable band gap and the anisotropic, trigonally warped low-energy dispersion are the key factors for unusual ballistic electron optics in bilayer graphene (BLG) different from the standard Dirac case. The low-energy band-structure of BLG is given by equation (6). The presence of v_3 skew hopping parameter breaks rotational symmetry and induces trigonal warping, leading to triangularly deformed Fermi surfaces with opposing orientation in the $K^{\pm}$ valleys, as can be seen in figure 19(b). Since an anisotropic dispersion entails a corresponding anisotropy in the charge carriers' velocity distribution, $\mathbf{v} = \frac{1}{\hbar}\nabla_{\mathbf{k}}E$, the trigonally warped dispersion of the bilayer graphene leads to directional and valley dependence of the ballistic electronic transport.

Anisotropic ballistic charge carrier dynamics in bilayer graphene has been observed directly in scanning gate microscopy (SGM) experiments: In [168], they raster-scan the bilayer graphene areas behind a gate-defined channel with an SGM tip and measure the linear conductance between source and drain as a function of the tip position. The resulting conductance map in figure 18(b) shows two narrow jets emanating from a gate-defined bilayer graphene channel predominantly at an angle of 60° with respect to each other. These collimated jets at this specific angle directly result from the reduced symmetry of bilayer graphene's trigonally warped dispersion, equation (6). For charge carriers at a given Fermi energy, the triangular Fermi line gives rise to three distinct preferred directions per valley (normals to the triangle's flat legs). The electronic states emerging from the channel populate these directional states according to the distribution of the occupied channel mode. As a result, there are two jets behind the channel corresponding to one of the preferred directions per valley. The right panel of figure 18(b) depicts the calculated angle-dependent propagation probability that one obtains when weighting the propagation directions prescribed by equation (6) by the distribution of the lowest confined channel mode. The calculations were carried out in the frame of the four-band continuum model of bilayer graphene [63–65, 168] valid at the relevant low energies. For recent additional evidence for the anisotropic transport, see [200]).

The charge carriers' anisotropic velocity distribution is an intrinsic material property of bilayer graphene and its trigonally warped dispersion impacts different aspects of ballistic propagation.

For one, the real-space anisotropy translates into the Fresnel and Snell laws for diffraction and reflection at p/n-junctions in bilayer graphene. The discussion is similar to that of monolayer graphene laid out in section 2.3.1, but for bilayer graphene, the non-isotropic Fermi lines and opening of a gap must be taken into account [201, 202]. The unique interplay between anisotropic scattering and anisotropic ballistic propagation in bilayer graphene has prompted investigations into the potential for intraband electron focusing and

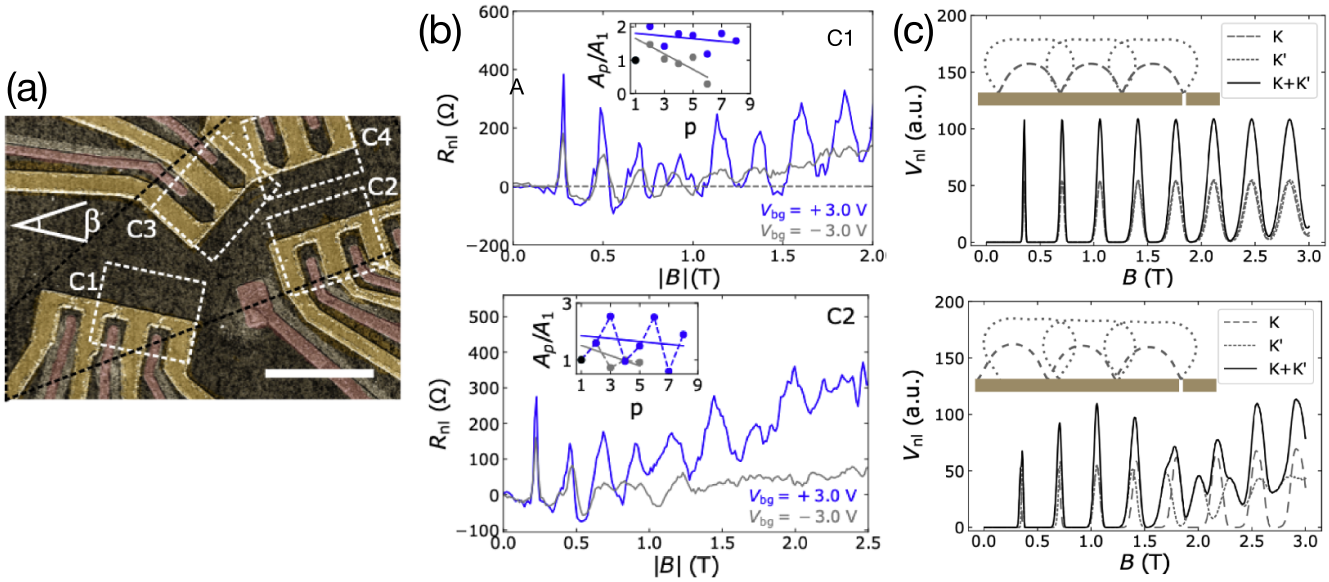

Figure 19. Anisotropic magnetic trajectories in bilayer graphene. Due to the C_3 symmetry of the trigonally warped Fermi lines, transverse electron focusing in bilayer graphene depends on the orientation of emission and detection with respect to the lattice (a). (b) TEF resonances for two differently oriented devices. (c) Simulated TEF signal for perfectly aligned (top) and 3° misaligned (bottom) quantum point contacts with respect to bilayer graphene's armchair crystallographic direction taking into account the trigonally warped and valley dependent Fermi lines. Reproduced from [156]. CC BY 4.0.

valley-selective electronic Veselago lenses in bilayer graphene [202]. These concepts allow for manipulating and controlling electron motion based on a material's properties and symmetries. Further research has explored the motion of electrons in gate-defined bilayer graphene cavities, revealing unusual regular and chaotic trajectory dynamics due to the anisotropies and nonlinearities induced by the trigonally warped Fermi lines [103, 201]. We discuss electronic cavities in detail in section 4.5.

Moreover, the deformation of the Fermi lines in bilayer graphene has consequences for the trajectories of charge carriers when exposed to weak magnetic fields. Sections 4.1 and 5.2 describe how the combined influence of the magnetic field and the charge carrier density on the radius of circular cyclotron orbits of circularly symmetric dispersions leads to transport resonances in transverse magnetic focusing experiments. Specifically, the deformation of the Fermi lines and the corresponding cyclotron orbits changes these caustics of transverse electron focusing resonances. For example, in bilayer graphene, the valley dependence and deformation of the Fermi lines change the position and shape of these caustics depending on the orientation of the device with respect to the lattice, and hence the positions where the charge carriers are focused and defocused as they move through the material. These deformations have implications for how to steer and confine bilayer graphene's charge carriers in magnetotransport, cf figure 19 from [156]: Here, the authors study magnetic focussing between gate-defined bilayer graphene channels along different crystallographic directions, demonstrating the effect of the non-rotationally symmetric, trigonally warped cyclotron orbits.

The discussion above about anisotropic electron optics in ballistics bilayer graphene relies on the anisotropic band structure and resulting velocity distribution. This line of argumentation is not limited to Bernal stacked bilayer graphene but applies to any material with an anisotropic dispersion. Further common examples of materials with anisotropic Fermi lines include heterostructures of graphene and hBN, twisted multilayer graphene structures, and graphene with gate-defined superlattices. In the former instance, the moiré superlattice potential induced by the adjacent hBN leads to reconstructed spectra with circular, trigonal, or hexagonal symmetry as a function of doping, cf figure 20 on transport studies of anomalous cyclotron motion in hBN/graphene/hBN) [99] and figure 13 ([116]).

In the left panel of figure 20(a) the computed modified band structure is shown, which exhibits strong electron–hole asymmetry. As visible in the left inset, the Fermi surface can assume both isotropic or hexagonal textures, depending on the energy regime. This leads to distinctly different electron propagation in magnetic field as shown for two different doping situations: The lower sequence of panels shows for the circular Fermi surface the magnetic-field dependent propagation of bended electron waves along usual cyclotron orbit segments. In contrast to that, at an energy corresponding to the hexagonal Fermi contour, electron waves stay straight and nearly B-field unaffected at weaker fields and follow peculiar hexagonal-shaped orbits for stronger fields [99].

In the case of graphitic multilayers, e.g. large angle twisted bilayer graphene [158] and twisted monolayer-bilayer graphene [203] show trigonally distorted Fermi lines with various shapes at different Fermi energies. Gate-defined

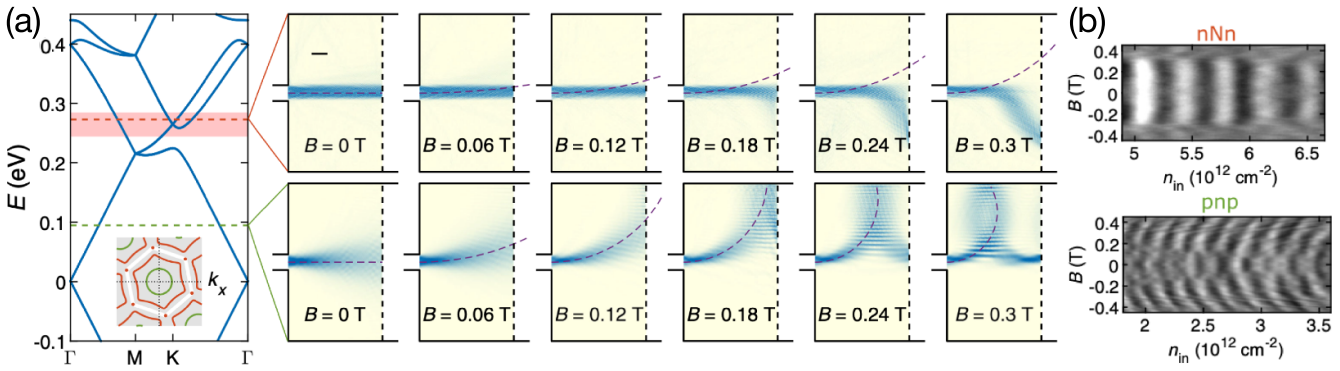

Figure 20. Magnetotransport in graphene/hBN superlattices depending on the Fermi line shape. (a) Left: the band structure of a graphene/hBN moiré superlattice exhibits hexagonal (red) or circular (green) Fermi lines at the K point of the mini-Brillouin zone depending on doping. Right: charge carrier beams from simulations in the two different regimes show bending or no bending in a magnetic field depending on the possible directions prescribed by the Fermi line symmetry. (b) Bending or no bending of the ballistic charge carrier trajectories was evidenced in dispersive or nondispersive interference fringes in graphene/hBN Fabry–Pérot cavities reprinted (figure) with permission from [99], Copyright (2020) by the American Physical Society, (see section 5.1 and section 5.2 for a detailed discussion about interferences in Fabry–Pérot cavities).

superlattices allow inducing diverse and variable potential modulations by virtue of patterned gates [110, 204–206], entailing Fermi surfaces of various shapes and symmetries [207]. Furthermore, external perturbations such as mechanical strain and shear can lower spatial symmetries and induce anisotropies in a material's electronic dispersion [208, 209]. Generally, the discussion of anisotropic ballistic electron optics highlights the complex nature of electron motion in materials with anisotropic dispersions.

4.5. Directed emission from single- and bilayer graphene cavities

4.5.1. Tailoring charge carrier emission from graphene disks. There are different ways to tailor graphene-based cavity regions. Complementary to gates, as used in several of the charge carrier guiding and steering experiments reviewed in section 4.4.1, disk-like cavities have been created by employing a scanning tunneling setting, see figure 21(a). Within such circular p-n junctions, whispering-gallery type resonant states that are confined through the ring-shaped p-n junction have been probed experimentally [210], see also [104, 211]. Such resonant states are exceptionally long-lived and stable against decay from the cavity due to Klein tunneling suppressing the tunneling of waves with grazing incidence. In figure 21(b), such whispering-gallery modes are depicted for different angular momenta, respectively. Panels (c) and (d) display corresponding observed and calculated $\mathrm{d}I/\mathrm{d}V$ spectra of the whispering-gallery resonant states. Subsequently, non-reciprocity of such whispering gallery modes was theoretically predicted [212]. Earlier theoretical works had addressed the influence of the classical charge carrier dynamics' character (integrable versus chaotic) on transport through open cavities [213–218] and spectra of closed cavities [219–221] of different shapes. Recently, in [222] ballistic graphene disks with spin-orbit interaction have been shown to host chiral spin channels with the spin fully in-plane and radially polarized upon tuning certain parameters.

The experimental realization of disk-like cavities has opened up several intriguing directions, arising from the fact that the physics of resonant states in single-layer graphene cavities has much in common with the field of mesoscopic optics: there, corresponding settings for electromagnetic radiation have been devised for controlling highly directional emission from asymmetrically shaped, lasing cavities [223]. In these dielectric microcavities, total internal reflection partially confines light in whispering-gallery type modes [224]. Breaking of the rotational symmetry was found [223, 225] to lead to directional light emission of decaying resonant states. These emission characteristics were understood by invoking optical ray-wave correspondence. The cavity geometry determines the phase space structure of the rays inside the cavity in the classical ray limit of optics. Controlling the ray phase space structure by deforming the cavity allowed one to steer directional emission and lasing in the optics context.

Based on a corresponding ray-wave correspondence approach for electrons in graphene, such mesoscopic optics concepts have recently been transferred to specific graphene cavity setups. These cavities are defined by the p-n interface geometry that, in turn, is determined by the gate voltage step from the inner to the outer region, i.e. V_{in} to V_{out} where V_{in} is related to V_{out} by an effective index n of refraction, $V_{\mathrm{in}} = nV_{\mathrm{out}}$, as explained in section 2.3.1. A back-gate voltage provides a tunable parameter to mimic different effective refractive indices and, thereby, the corresponding Fresnel laws at the boundaries. The possibility of readily realizing negative refractive indices in graphene adds to the fascination of such studies.

In [226], the decay features of integrable disk- and chaotic stadium-type cavities were studied based on classical ray tracing. Schrepfer *et al* [103] explores charge carrier trapping and (directed) emission for deformed leaky graphene

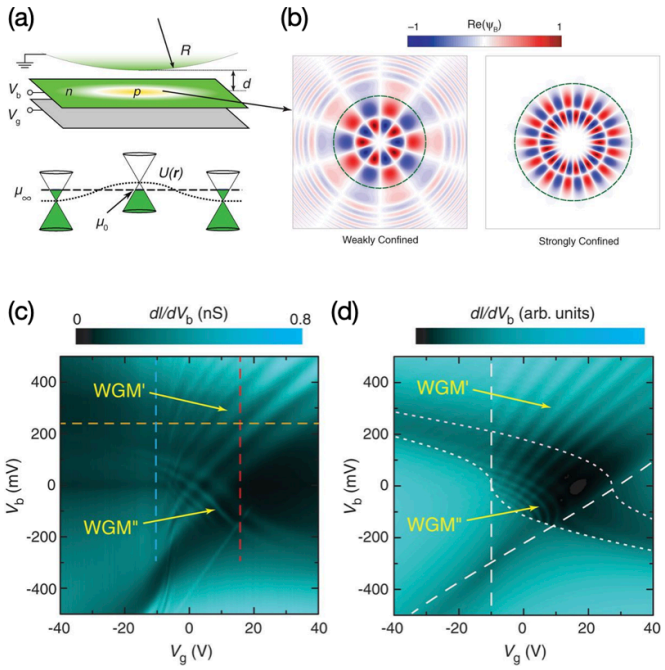

Figure 21. Confining and probing electronic states in single-layer graphene cavities. (a) Disk-like microscopic cavity (hosting resonant states) based on a circular p-n junction created by the combined effect of an STM tip with voltage bias (Vb) and a back-gate voltage (Vg) inducing a ring-type p-n junction (see [210]). It creates a sharp boundary with associated Klein scattering of charge carrier waves giving rise to confined whispering-gallery resonant states. (b) Spatial profile of calculated whispering-gallery modes. The effective confinement is stronger for larger angular momentum with more oblique wave incidence angles. The left (right) panel shows modes with weak (strong) confinement, respectively. (c) Differential tunneling conductance (d*I*/dVb) as a function of Vb and Vg. The two fans of interference features, marked WGM' and WGM", originate from different WGM resonances. (d) Corresponding calculations based on an effective Dirac model. From [210]. Reprinted with permission from AAAS.

micro-disks by considering the complete ray-wave correspondence through classical and quantum simulations. As depicted in figure 22(a), the corresponding ray and wave results agree semi-quantitatively. They both exhibit a pronounced directed emission of electrons, leaving the cavity to the right for that setting. More generally, one finds various emission characteristics depending on the position of the source where charge carriers are fed into the cavities. Furthermore, single-layer and double-layer graphene cavities exhibit Klein- and anti-Klein tunneling at the cavity boundary, respectively, leading to distinct differences concerning dwell times and resulting emission profiles of the cavity states. Moreover, bilayer-based cavities offer the additional possibility to tune between Klein and anti-Klein tunneling by varying a respective asymmetry parameter [65, 108, 111, 201, 227, 228]. For bilayer graphene, trapping of resonant states is more efficient, and the emission characteristics depend less on the source position [103]. Recently, in [228] the trapping, respectively transmission, of charge carriers in a single- and bilayer graphene-based Corbino disk has been studied and proposed as a signature of Klein and anti-Klein tunneling, respectively.

4.5.2. Symmetry breaking through anisotropic Fermi surfaces. The left panel of figure 22(b) shows a typical resonant state in a bilayer-graphene-based disk. Interestingly, despite the circular cavity geometry, the wave simulation result displays distinct emission directions, which can be understood as follows. While the current is injected isotropically from the central point source, the reflected waves (through anti-Klein tunneling) return to the point injector, then acting as a scatterer. However, the scattering is non-isotropic because the underlying Fermi contour gets non-circular for bilayer graphene at finite energies. Hexagonal contributions to the Fermi contour lead to six predominant velocity directions [99] that are filtered out, cf section 4.4.2, figure 20. They determine the resonant state in figure 22(b) and thereby peculiar directional charge carrier emission. In [201], the emergence of non-standard fermion optics solely due to anisotropic material characteristics, i.e. *k*-space structure, has been examined in much more detail. There it is shown how the anisotropic dispersion of bilayer graphene induces chaotic and regular charge carrier dynamics depending on the gate voltage, despite the high symmetry of the circular cavity, cf the right panel of figure 22(b).

These findings imply that directional emission can be steered by breaking the cavity geometry's symmetry and through an anisotropic dispersion. Compared to standard mesoscopic optics, graphene electron optics provides an additional, fundamentally different further mechanism for symmetry breaking and steering electron beams. Besides, contrary to electromagnetic optics, the charge carrier dynamics in graphene can be further manipulated through external magnetic fields, opening another angle of research. We discuss various aspects of *k*-space anisotropies in ballistic graphene-based systems in section 4.4.2.

5. Quantum-interference in graphene p-n junctions

5.1. Quantum-interference in zero magnetic field

5.1.1. FPI based on p-n junctions. In a ballistic 2D electron system, a combination of semitransparent mirrors can result in cavity resonances when wave propagation is coherent. A very well-known example from optics is the Fabry–Pérot interferometer (FPI). It consists of two parallel semitransparent mirrors that are spaced by a distance L_c. An illustration is shown in figure 23(a). An optical plane wave incident from left under an angle Θ relative to the normal of the mirrors enters the cavity with transmission probability T. At the other mirror the wave is reflected with probability $R = 1 - T$. This process can be continued to a finite number of partial waves limited by temporal and spatial coherence. Once summing up all transmitted partial waves $\sum_i \psi_i$ one obtains for the transmitted intensity the well-known relation $1/(1 + K\sin(\gamma/2)^2)$, where $K = 4R/T^2$ is proportional to the square of the so called Finesse $F = \pi\sqrt{R}/T$ and γ the propagation phase between two successive emitted partial waves: $\gamma = 4\pi n L_c \cos(\Theta)/\lambda$. Here, n is the refractive index and λ the wavelength. The finesse can be seen as the quality factor, which in a practical optical etalon or narrow-band filter can take large values close

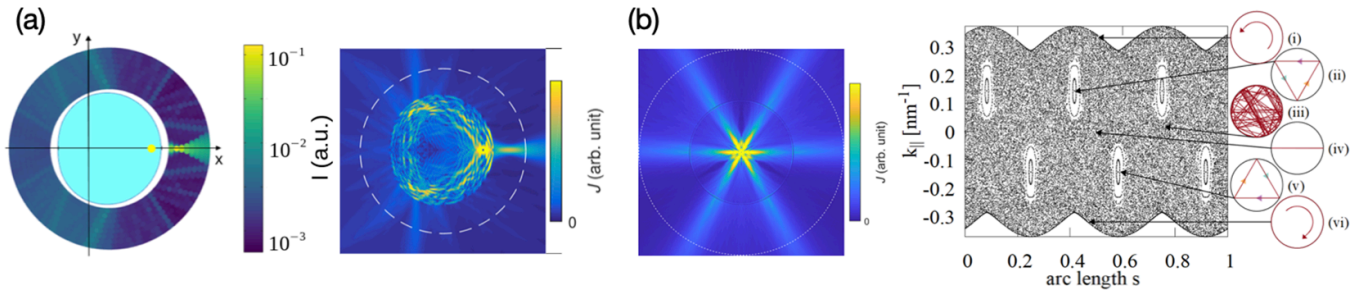

Figure 22. (a) Directed charge carrier emission from tailored graphene-disks. Ray-wave correspondence in single-layer graphene billiards of Limaçon shape with effective refractive index $n = -1$. The light blue area marks the cavity. Left: Ray simulations for point source injection marked as yellow dot. Right: Corresponding wave simulations for the same source position as on the left. The color scale represents the electronic wave function intensity. Reprinted (figure) with permission from [103], Copyright (2021) by the American Physical Society. (b) Effects of k-space anisotropy. Left: Local charge carrier density for charges injected from a point-like source at the center of a bilayer graphene disk (diameter 1 μm), dashed line marks the midfield region ($r_m = 2$ μm). Reprinted (figure) with permission from [103], Copyright (2023) by the American Physical Society. Right: Poincaré surface of section revealing different types of trajectory dynamics in a gate-defined bilayer graphene electron cavity: chaotic dynamics (iii), stable triangular, periodic orbits (ii, v), unstable periodic orbits along the diameter (iv), and whispering-gallery-like orbits (i, vi). Images taken from [201].

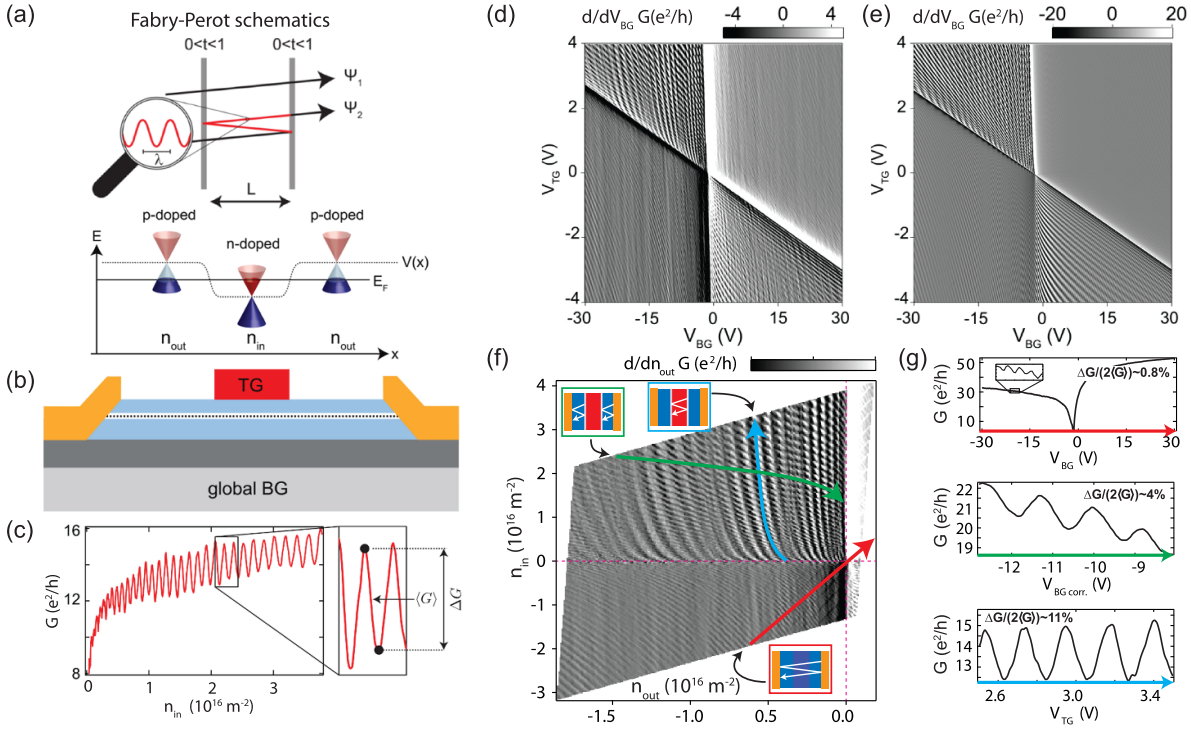

Figure 23. FP oscillations in p-n-p or n-p-n cavities. (a) Schematics of a Fabry–Pérot (FP) setup with two planar mirrors separated by the distance L. The mirrors have a fixed transparency of t. In the lower part, the bandstructure is shown for such a three-section graphene device in a p-n-p gate configuration. (b) Cross section of the encapsulated graphene device with the two outer sections controlled by the global back gate (BG) and the middle one controlled by the local top gate (TG). In (c) the measured conductance $G(n)$ as a function of carrier density n is shown for a typical device. The conductance modulation corresponds to $\sim$10%. (d), (e) The derivative $\mathrm{d}G/\mathrm{d}V_{\mathrm{BG}}$ of the two-terminal conductance is shown as a function of back-gate and top-gate voltages. The left graph (d) is the experiment and the right one (e) the simulation. (f) G as a function of normalized densities in the outer, n_{out}, and inner region, n_{in}. On the right side (g) three cuts along different directions (red, green, blue) are shown. The modulation is clearly largest along the blue cut, which is the directions along which only the carrier density of the inner region is changed. (a)–(e) Reproduced with permission from [69]. The calculation in (e) was performed by Ming-Hao Liu and (f) and (g) Reprinted with permission from [229]. Copyright (2017) American Chemical Society.

to $F \sim 1000000$, see e.g. in [230]. In analogy, electrons in a ballistic 2D electron systems at the Fermi energy are coherent if temperature is small enough and phase randomization due, for example, gate noise can be neglected. Since p-n junctions in graphene have the properties of a semitransparent mirror, they can serve as elements to realize an electronic FPI. An example is sketched in figure 23(b) and a typical interference pattern as measured by the two-terminal conductance G, which is proportional to the total transmission probability, is shown in figure 23(c). Here, an encapsulated graphene device

is sketched that consists of three gateable regions: the central inner one and two outer regions that are gated by the back gate BG, while an additional top gate TG is used for the inner region. Here, we can realize a n-p-n, p-n-p or a general n-n'-n device. Let us assume that we gate the device into the p-n-p regime as indicated by the energy diagram. The measured interference pattern in G is shown as a function of carrier density in the middle section $n_{\rm in}$. The carrier density in the inner n-region is increased starting from the CNP at $n_{\rm in} = 0$ to $4 \cdot 10^{16}$ m^{-2}. The conductance increases with carrier density as expected, but on top of this general trend conductance oscillations are seen. The visibility is of order 10%. This is very different to optical cavities where the visibility is $\sim$ 100%. This shows that the transmission probability of the mirrors in graphene, averaged over all angles is surprisingly large. This is due to Klein tunneling which leads to a large transmission at normal incidence. If we would only consider waves travelling normal to the p-n junctions, the visibility would disappear. It is important to remember that the low visibility in graphene interferometers based on p-n junctions as semitransparent mirrors is not caused by limitations in coherence but is intrinsic and caused by Klein tunneling [25].

The bandstructure of graphene at the tight-binding level is rather simple. However, combining all electrodes and contacts with graphene is not straightforward to model, but it can be performed using the scaling approach introduced in detail in section 2.5.3. Figure 23 shows a comparison between a measurement (panel (d)) and the respective parameter-free simulation (panel (e)). The correspondence between the two is remarkable, even detailed features are reproduced. Note, to enhance the features, the derivative of the conductance versus the back-gate voltage is plotted here. There are four regions, clearly separated by two pronounced lines. The vertical line at $V_{\rm BG} = 0$ corresponds to the CNP in the outer two regions. The line with the negative slope corresponds respectively to the CNP of the middle region. This line has a finite slope because $n_{\rm in}$ is tuned by both gate voltages. Of the four quadrants, the top left corresponds to the gating situation p-n-p, the top right to n-n'-n, bottom right to n-p-n, and bottom left to p-p'-p. We see Fabry–Pérot (FP) interference effects in all four quadrants, though they are the weakest in the n-n'-n case. In contrast, they are most pronounced in the bipolar regions. Here, the main contribution originates form the expected FP resonances formed in the inner region. For the unipolar situations, the electron waves propagate all the way from the left source to the right drain contacts, where reflections can happen, too. That the oscillations are fainter in the n-n'-n case as compared to the p-p'-p case suggests that the contacts are n-doped. In this case, there are also p-n junctions present at the contacts enhancing the reflection probability. It is instructive to inspect the interference pattern even further. A zoomed-in graph is shown in figure 23(f), now plotted as a function of normalized coordinates, $n_{\rm in}$ and $n_{\rm out}$. The modulation in G that one experiences in a cut along the blue line corresponds to the proper FP oscillations of the inner cavity (see panel (g) for the conductance traces along these lines). The oscillation along the green cut shows oscillations that are due to FP oscillations generated in the left and right outer regions separately. And finally, the red cut corresponds to unipolar gating with the largest cavity size. The visibility is the weakest in the red cut, intermediate for the green one, and largest for the blue cut.

FP resonances have become the key signature for claiming ballistic transport in all kinds of graphene devices [23, 25, 31, 61, 87, 111, 229, 231–240] which is only qualitatively correct as detailed below. FP resonances not only appear in the linear-response conductance, but also when superconductors are involved, for example in the critical current of graphene-based Josephson junctions [234, 236, 238, 239] and in Andreev reflection in normal metal-graphene-superconductor devices [240]. They would also show up in thermoelectrical properties [231, 241] and higher moments in charge transfer, for example in noise properties. FP interferences go beyond monolayer graphene. They have been observed in bilayer [111] and trilayer graphene [232]. Additionally, in graphene superlattices the secondary Dirac points can give rise to additional (quasi-) bipolar barriers, yielding more complex interference patterns [99, 229, 242].

While the observation of FP interferences is widely used as evidence for ballistic transport, based on the bare observation one should not claim that the scattering mean-free path is larger than the sample size: $l_{\rm mfp} > L$ (see a similar discussion on magnetic focusing in section 4.1). Even if there is appreciable disorder, e.g. close to sample edges, there is still a distribution in scattering so that there might still be enough electron trajectories that remain ballistic in the interior of the sample. A detailed study would require modelling the visibility of the interference pattern taking also finite temperature into account [243]. As mentioned before, p-n junctions are never abrupt, and they are rather smooth in high-quality graphene devices which can be operated at lower carrier concentrations for which $\lambda_{\rm F}$ is large. To assess the effective width of the p-n junction barriers, it is helpful to deduce the effective cavity length L_c from the experiment. It can be estimated if we assume hard wall potentials bounding the cavity. For waves travelling normal to the cavity mirrors, constructive interference occurs if the path difference between the adjacent partial waves is a multiple of $\lambda_{\rm F}$. This leads to the condition $2L_c = j\lambda_{\rm F}$, where j is an integer. Since the Fermi wavelength $\lambda_{\rm F}$ depends on the carrier density as $k_{\rm F} = 2\pi/\lambda_{\rm F} = \sqrt{\pi n}$, we obtain for the j-th constructive interference maximum the condition $L_c\sqrt{n_j} = j\sqrt{\pi}$. In the experiment we can note down the carrier density for two adjacent conductance maxima, n_{j+1} and n_j, to obtain for the effective cavity length L_c the equation $L_{c,j} = \sqrt{\pi}/(\sqrt{n_{j+1}} - \sqrt{n_j})$. This length depends on the index j. In practice it should be a constant if the barrier were indeed hard wall potentials. However, it strongly varies in graphene devices. In a p-n-p graphene cavity, the extracted $L_{c,j}$ strongly depends both on the inner and outer carrier density. L_c expands (shrinks) if the inner carrier density is increased (decreased), and vice versa, L_c shrinks (expands) if the outer carrier density is increased (decreased). The change in cavity length can be large and can account for a $\sim$100% change [69, 229]. Until today, Fabry–Pérot interference effects were only studied in the low bias regime, where the oscillations display a checkerboard pattern in conductance on bias-gate maps. It would be interesting to explore interference effects also in the non-linear

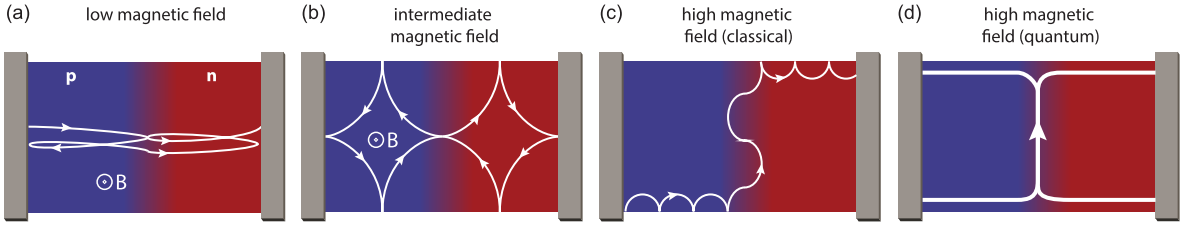

Figure 24. Different field regimes. This schematic emphasizes on the four different magnetic-field regimes. In the Fabry–Pérot regime (a) the straight classical electron trajectories are only slightly bent, while for larger fields (b) two-dimensional cavity bound states, also known as scar states, can form. If the magnetic field is as large that the cyclotron orbit is smaller than the sample dimension both in width and length, skipping orbits are formed (c). These orbits are chiral, meaning that there is a unidirectional propagation determined by the sign of magnetic field and the sign of the charge carriers (electron or holes) along each edge. At a p-n junction, and for a constant magnetic field, snake states lead to a current flow that follows the p-n junction, crossing one side of the sample to the other. If the field is even higher (d), one enters the quantum Hall regime where skipping orbits become one-dimensional edge channels. Reproduced from [27]. CC BY 4.0.

transport regime, which is a topic of increasing interest [244]. The temperature dependence of FP resonances has been studied in detail in [243].

5.2. Non-zero magnetic field (low field regime)

5.2.1. Different magnetic-field regimes. In the following, we introduce the four different magnetic field regimes for p-n junctions, depicted in figure 24. We assume phase-coherent ballistic transport and consider a single p-n junction in the center of a two-terminal graphene device. Since there are two cavities, Fabry–Pérot resonances may appear on both sides of the p-n junction, provided there is enough specular scattering of electron waves at the contacts. We have already mentioned that contact doping is a general phenomenon in graphene devices. It can be n or p-type depending on the contact material and fabrication processes involved. It is a parameter that is still today not very well understood. Let us further assume that the size of the sample is much larger than the Fermi wavelength λ_F and that the graphene edge is ideal with a large probability for specular reflection. In this case, we can consider electron propagation in the form of wave packets that follow semiclassical electron-optical trajectories. A magnetic field B applied perpendicular to the graphene plane causes a Lorentz force to act on the electrons which consequently are deflected. If the deflection angle is much smaller than one, we are in the low field limit which is indicated in figure 24(a). Here, the Fabry–Pérot condition for constructive interference is only slightly modified. But there is an interesting effect in the acquired phase which has been used as evidence for Klein tunneling [22]. It will be discussed further below. The electrons in a homogeneous magnetic field will follow cyclotron motion, as detailed in section 2.2.1. The cyclotron radius, r_c shrinks with increasing magnetic field. If r_c is of order sample size (length or width), the corrections to the conventional Fabry–Pérot resonance are becoming large. New bound states can form, so called scar-states [245]. A very symmetric scar-state is indicated as an example in figure 24(b). Scar states can be much more complex having intersecting electron trajectories, for example. If r_c is smaller than the sample size, full cyclotron orbits fit into the two cavities. Now, so-called skipping orbits are formed along the edges of the device as seen in figure 24(c). They lead to charge transport along the edges in a directional manner determined by both the sign of the magnetic field and the carrier type. The cyclic motion is opposite in a p-type materials as compared to an n-type one, as discussed in section 2.2. If we follow the cyclic motion along the edges, we see that propagation can be pinned to a p-n junction, due to the opposite chirality on opposite sides of the junctions. The charge motion now follows the partial cyclotron orbits along the p-n junction. This propagating state is known as snake-state [27, 94, 235, 246–253]. This is a very peculiar addition to charge transport as it connects the two edges of the graphene device. Snake-states were proposed already before graphene for 2D electron systems realized in semiconducting heterostructures [254–257]. Since this electron gas is unipolar (electrons), one requires a magnetic field reversal in the two areas to obtain a snake state. This is much more difficult to realize. Hence, the ambipolar nature of graphene has given us a neat playground to study this special kind of electron state [27, 235]. If the magnetic field is increased further, the skipping orbits evolve into quantum Hall edge states [95, 258–262]. To understand when and how one enters the quantum regime it is instructive to look at the cyclotron frequency $\omega_c = eBv_F/\hbar k_F$. To reach the quantum Hall regime, ω_c times the scattering time in the bulk should be larger than one. This ensures that there are full cycles that need to be quantized along the usual Sommerfeld-Bohr condition. Additionally, $\hbar\omega_c$ should be larger than the thermal energy. There is an additional length parameter, known as the magnetic length l_B which follows from the Landau quantization: $l_B = \sqrt{h/eB}$. Now, we can formulate the two conditions required to remain in the regime where semiclassical electron orbits can be considered: $l_B \gg \lambda_F$ and $r_c \gg \lambda_F$. To remain in the semiclassical regime, the magnetic field cannot be too large. What is very interesting and peculiar is the dependence on electron density. The cyclotron radius shrinks with decreasing density. Hence, the closer one approaches the Dirac point (zero density), the less trustable is the assumption of semiclassical transport. If one crosses from an n-type to a p-type region, the semiclassical approach must break down in the center of the junction. It is therefore clear that a semiclassical approach to snake states can only

Table 3. This table illustrates the dependence of the Fermi wavelength λ_F and cyclotron radius r_c at a relatively weak magnetic field of 0.1 T on the gate voltage V_g or the respective carrier-density n. The first two rows show cases where a classical description is not valid, as the filling factor ν drops below one. It is important to rationalize that while passing across a p-n junction the carrier-density must change sign. Hence, there is a region in the center of the p-n junction where a classical description in terms of electron trajectories can only provide an approximation.

V_g (V)	n (cm^{-2})	λ_F	r_c (at 0.1 T)	l_B (at 0.1 T)	ν (at 0.1 T)
0.01	10^8	3 μm	12 nm	200 nm	0.04
0.1	10^9	1 μm	40 nm	200 nm	0.4
1.0	10^{10}	330 nm	120 nm	200 nm	4.0
10	10^{11}	100 nm	400 nm	200 nm	40

deliver qualitative results and that a proper quantum treatment is required to make quantitative predictions.

Another interesting relation is given by $(l_B/\lambda_F)^2 = r_c/\lambda_F = \nu/4\pi$, where ν denotes the filling factor given by $\nu = nh/eB$. Semiclassical transport, as discussed in the following two sections, requires large filling factors. To have an idea regarding absolute values, examples for typical graphene densities at a still low magnetic field of 0.1 T are given in table 3:

5.2.2. Correction to Fabry-Pérot oscillations for the lowest magnetic fields. For low magnetic fields the classical electron-optical trajectories bend very little. It is important to recall how the FP signal appears in a graphene p-n-p device without a magnetic field. Due to Klein tunneling, there are no contributions to the interference from trajectories that propagate normal to the two mirrors. These trajectories have angles $\Theta_1 = \Theta_2 = 0$. Only trajectories with a finite angle add to the interference. Since the reflection amplitude at each mirror drops fast with angle, due to the typical soft potential steps in realistic devices, the main contribution to the interference is due to electron trajectories with finite but *small* angles [22]. A scattering situation with finite angle in zero magnetic field is shown in figure 25(a). The two angles at the two mirrors have opposite sign, $\Theta_1 = -\Theta_2$ in (i). As pointed out by Shytov *et al* [25] the reflection amplitude of the mirrors, $r_{1,2}(\Theta)$, must be an odd function, since $r_{1,2}$ goes through zero when Θ changes sign. This sign change is thus an additional feature of Klein tunneling. It has measurable consequences when a magnetic field bends the electron trajectories. There are bent trajectories of two kinds possible: (ii) one for which the two angles remain of opposite sign, and one kind for which the two angles have the same sign. In the former, and thus for small magnetic fields, a phase shift of π adds to the interference contribution due to the product $r_1 \cdot r_2$ acquiring a minus sign. With increasing magnetic field, the symmetric trajectories that enclose the origin start to dominate and the π shift disappears. Hence, it has been proposed that a hallmark of Klein tunneling would be a π-shift of the FP oscillation pattern when a magnetic field is added [25]. This has indeed been observed, first by Young and Kim [22]. The magnetic field scale for this transition is determined by the inverse of the cavity area given by the length of the cavity times its width.

Figure 25(b) shows the first experimental evidence for the π-shift due to Klein tunneling [22]. One can see that the interference fringes shift a bit faster with magnetic field around a field value of 0.5 T. The additional five cross-sections in (c) make this effect a bit clearer. Due to the generally observed dispersion of the interference fringes with magnetic field the π-shift is not as evident as one would like to have it. In higher mobility samples, the shift can show up in a more pronounced manner. This is illustrated with figure 25(d) where the cross-over already appears at around 25 mT [69]. This result was obtained in an encapsulated graphene device with a much longer cavity length compared to the previous mentioned example. Figure 25(e) shows FP resonances measured in a suspended ultraclean graphene device in a larger parameter range [75]. For magnetic fields $\gtrsim$15 mT further oscillations appear. They are highlighted with yellow lines on the negative magnetic field side. These resonances are so-called scar-states. They were discovered in studies of bound states of quasi-classical trajectories of electrons in a two-dimensional electron gas with stadium boundaries [263]. Unlike the FP resonances, which can be seen as one-dimensional bound states, scar states are cavity states that include scattering at the edges of the sample. Additionally, a measurement and a simulation of conductance oscillations in a graphene device with a single p-n junction is reproduced in figure 25(f) and (g). Here the boundary between the 'low-field' regime and the 'large-field' regime is emphasized. The boundary is determined by the condition $r_c = L$, where L is the cavity size and r_c the cyclotron radius. Outside this boundary, states with a parabolic-like dispersion are seen. These are due to skipping orbits and will be discussed in the next chapter. The resonances emphasized in blue are FP resonances where the typical π-shift is evident too. In addition, one can clearly see many more interference features in the low-field regime caused to two-dimensional cavity states. A remarkable good agreement between simulation and experiment is found [75].

5.2.3. Skipping orbits and snake states at intermediate to high magnetic fields. In the intermediate to high magnetic-field regime, the cyclotron radius r_c is smaller than the length and width of the cavity: $r_c < L, W$. In agreement with figure 24(c) we assume here a graphene device with a single p-n junction in the middle. The p-doped region is on the left side and has a hole-carrier density of $p_{\text{left}} > 0$. In analogy, the n-doped region is on the right side with electron carrier density of $n_{\text{right}} = p_{\text{left}}$. We assume first, that the carrier-density jumps abruptly at the p-n junction located at coordinate $x = 0$ (the x-axis points along the sample direction from source to drain and the y-axis is transverse along the p-n junction). In the classical electron optical picture and for a global constant perpendicular magnetic field B, the carrier trajectory would alternate between the p and n-side with skipping orbits being half circles with opposite chirality. This situation is illustrated in figure 26(a). The picture also suggest why one should observe conductance oscillations due to these so-called snake-states [264–266]. If the last half-cycle ends on the left side, the charge is reflected back to the source contact on the left. In contrast, if it ends on the right side, it will be transmitted to the drain contact

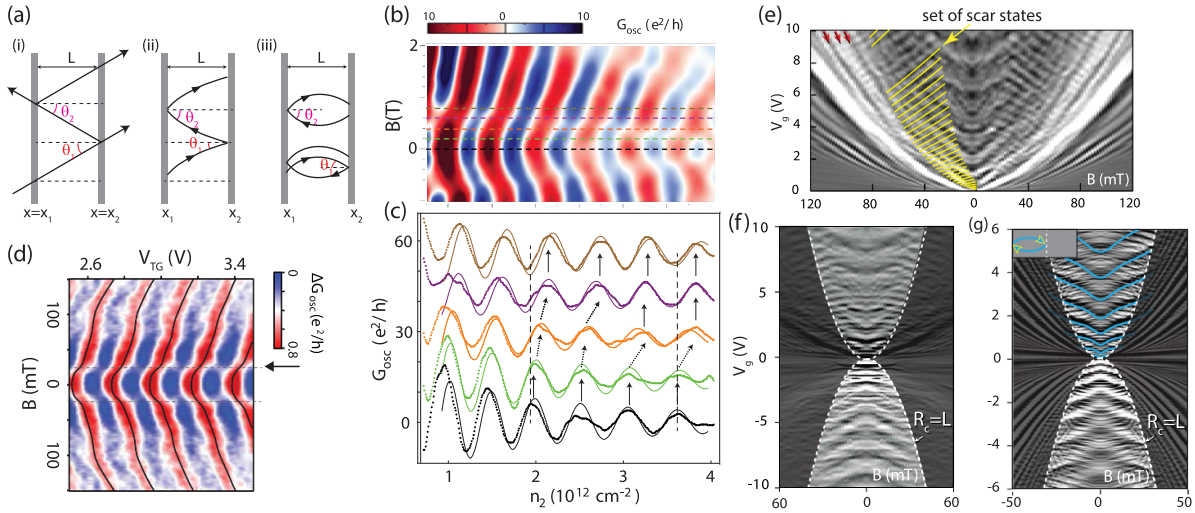

Figure 25. Low and intermediate field regime with π-shift and scar states. (a) schematically shows classical electron trajectories for a FP arrangement with two mirrors m_1 and m_2 at position x_1 and x_2 in (i) zero magnetic and (ii,iii) in a weak magnetic field. For the latter one must distinguish between two cases: (ii) when the two scattering angles have opposite or (iii) the same sign. The contribution from the symmetric loop, where the angles have the same sign, dominates for larger fields. This change in sign gives rise to a π-shift in the interference pattern. (b), (c) Experimental data of the π-shift. (b) and (c) Reproduced from [22], with permission from Springer Nature. The shift appears at around 0.5 T. (d) Similar experimental data obtained with an encapsulated graphene device, reproduced with permission from [69]. Here, the shift already appears at a much lower field of ∼20 mT. (e) shows another low-field interference pattern obtained from an ultraclean suspended graphene device, taken from [75]. The fine regular pattern, which is emphasized in yellow on the negative field side, is caused by scar states. Measurement (f) and a simulation (g) for interference in a single p-n junction as a function of magnetic field and gate axis taken along the bipolar direction. What is emphasized here, is the border between the low field and higher-field regime determined by the cavity size L and the cyclotron radius r_c. The upwards dispersing curves emphasized in light blue belong to the small angle FP interferences. The additional interference pattern within the low field region is due to cavity states (scar states). (e) and (f) Reproduced with permission from [75].

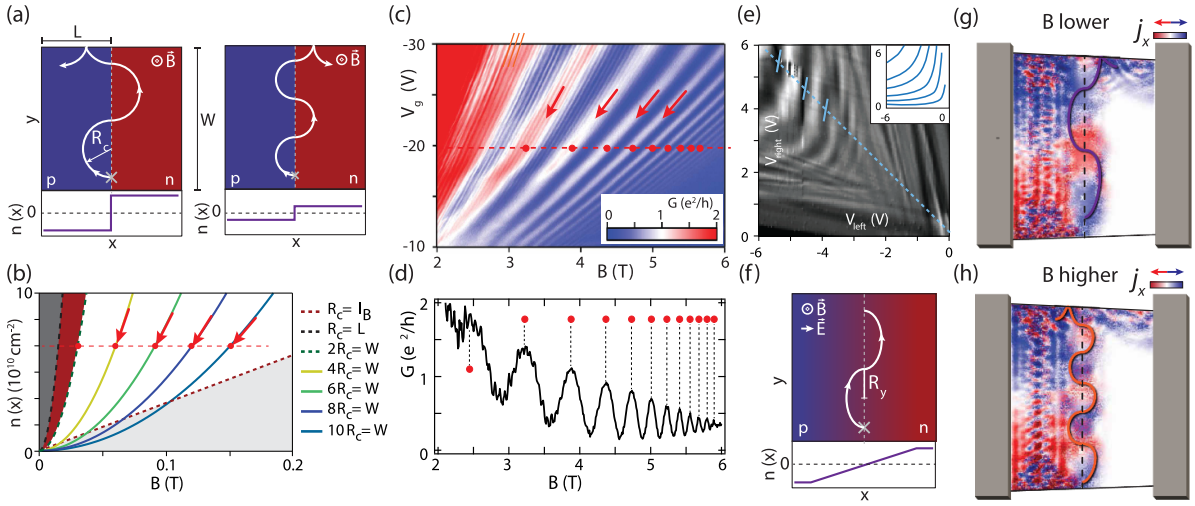

Figure 26. Intermediate to high-field regime with quasi-classical skipping and snake-state orbits. (a) Illustration of snake-states that propagate along p-n junctions. If we assume a common starting point (crosses) at the bottom, the trajectory may either end up on the left or right side, depending on the ratio between the width W and the cyclotron radius r_c. This results in conductance oscillations. Lines for a fixed ratio W/r_c are parabolic in a density n versus magnetic field B map, as seen in (b). For a constant density, neighboring peaks in $G(B)$ are expected to be equidistantly spaced (red dots). (c), (d) show an experimental result obtained in an h-BN encapsulated graphene p-n device. The snake-state oscillation is emphasized by the red arrows and red points. It is found that the peaks are not equidistantly spaced. This is caused by a distortion of the orbits due to the gradual density change at the p-n junction, sketched in (f), see text for further explanations. (e) shows the oscillation pattern in a gate-gate map at constant magnetic field. The peaks and dips follow a hyperbolic-like pattern (inset). Finally, (g) and (f) show numerical simulations of p-n junctions for two different magnetic fields. Plotted in color is the current density along the horizontal axis. If one follows the pattern along the zero-density line (dashed), one can see that there is a periodic sign change consistent with the notion of snake-states. In addition to the snake-state, one can see other bound states residing on the left side. These simulations were performed by Ming-Hao Liu, see [75]. Note, there are further equidistant oscillations (orange lines) seen in (c). They are of Aharonov–Bohm type and are addresses in further chapters. (a), (b), (e),(f)–(h) Reproduced from [27]. CC BY 4.0. (c) and (d) Reprinted (figure) with permission from [95], Copyright (2018) by the American Physical Society.

on the right. Hence, the conductance should oscillate with a period given by $4r_c$, if we assume that $p_{\text{left}} = n_{\text{right}} = n > 0$. The conductance modulation δG can be written to be proportional to $\cos(\pi W/2r_c)$, leading to conductance minima and maxima whenever W is an even multiple of r_c. Since r_c is proportional to $\sqrt{n}/B$, lines of constant phase in the n versus B plane follow a parabolic dependence: $n \propto B^2$. This is sketched in figure 26(b). In the experiment we expect the conductance modulation to follow the colored curves. The dashed red line denotes the condition $l_B = r_c$, with $l_B = \sqrt{h/eB}$ is the magnetic length. In the shaded region, where $l_B > r_c$, the quasi-classical description must break down. In this regime of large magnetic field and/or small carrier concentration, Landau quantization needs to be considered.

Figure 26(c) shows an experimental result [75]. Note, the gate voltage V_g controls both the carrier density on the p- and n-side with an equal magnitude. The stronger intensity modulation which starts with a spacing in magnetic field of ∼0.5 T, which then seems to decrease, is thought to be due to snake-states [27, 235]. The previous reasoning for the snake-state oscillation predicts a constant period δB in magnetic field at constant carrier density. This is not what is observed, as shown in panel (d). Clearly, if we consider a horizontal cut at constant density, the spacing narrows with increasing magnetic field. In the data, there is another set of faster but weaker oscillations seen superimposed. This oscillation pattern is to a good approximation equidistant in magnetic field. It likely originates from Aharonov–Bohm oscillations due to edge-states forming along the p-n junctions at small densities [95, 154]. This physics will be covered in section 6.2.

One could also think that other quasi-classical electron trajectories could contribute to the current. For example, trajectories crossing the p-n junction not at normal incidence, but with a shallower or larger angle. However, one expects that these contribute less to the total conductance. The main contribution is due to trajectories that cross the interface at (or close to) normal incidence, since for those trajectories the transmission probability is maximal due to the Klein effect, while for all others the transmission probability is strongly suppressed. This argument does not really hold for a sharp step in carrier density, but only for a smooth potential changes. In real devices, however, the step varies smoothly over a length of > 20 nm.

It is not straightforward to calculate the shape of the snake-state electron trajectory in a self-consistent manner, accounting accurately for the gradual potential change. The semicircles deform by elongating along the y-direction as indicated in figure 26(f). However, it is possible to evaluate the length R_y assuming a linear density change between the p and the n side [95]. One obtains:

$$R_y = \left(\frac{\pi\hbar}{eB}\right)^2 \frac{|p_{\text{left}} - n_{\text{right}}|}{2d}. \tag{44}$$

Here, d is the width over which the density changes from the p to the n-side. Interestingly, the skipping orbit length at fixed magnetic field is determined by the local electric field. Figure 26(e) shows measurements at fixed magnetic field of 0.12 T as a function of the two gate voltages V_{left} and V_{right} that control the densities in the two regions. The inset shows lines of constant electric field E_x obtained numerically. The oscillation pattern appears in the gate-gate map in the form of hyperbola. The modified equation for the skipping-orbit length preserves the relation $n(B) \propto B^2$ that is followed by intensity maxima and minima as introduced with figure 26(b). However, it does change the periodicity in magnetic field for constant densities. One does not expect a constant ΔB anymore, but rather $\Delta B \propto 1/B$. This fits much better to the experimental observation in figures 26(c) and (d) where it is evident that for a horizontal cut the spacing between adjacent conductance maxima decreases with increasing magnetic field. This observation can be taken as a confirmation that the potential drops gradually at the p-n junction.

Figure 26(f) also shows 2D-simulations of current patterns. Here, the current component in x-direction is shown for two different scenarios: a small and a large field. If we concentrate on the region of the p-n junction, with the zero-density line indicated by a dashed line, we can recognize the alternating skipping pattern. Following along the dashed line from the bottom to the top, the current alternates. It is first blue (positive), then changes to red (negative), and so forth. Hence, the picture of commensurate snake orbits determining the conductance is appealing. However, it assumes a fixed starting point. This starting point is indicated in figure 26(a) with a cross. One might think that the conductance oscillation could average out if one varies the starting point. There has been simulation of this problem in which the sum of all trajectories was considered. Interestingly, caustics can show up causing repeated refocusing which in a similar manner can cause the conductance modulation [116, 264]. If we look at the left half of the sample in the simulations, we see two things: (i) a fast oscillation pattern which is due to scar states, but (ii) we also see a peculiar blue region close to the bottom sample edge and an opposite red one close to the upper sample edge. These regions can be interpreted as the starting points of the quasi-classical picture with snake trajectories. The charge current is fed into the sample along the bottom edge with $j_x > 0$ (blue region). The current stream then follows the snake orbit. The part that is reflected ends on the top edge with $j_x < 0$ (red region). The part that is transmitted to the right can nicely been seen as skipping orbits along the upper edge in the right half of the sample. What exactly determines these 'starting points' is at present not known.

Since graphene is a zero-bandgap semimetal, the Fermi energy can continuously by moved from the valence band into the conductance band. Hence, the discovery of graphene had made it possible to study snake state physics in quite some detail for the first time [27, 235]. Other geometries that were theoretically studied are cylindrical magnetic field patterns, which can be realized in graphene with a cylindrical gate. Such a gate can confine electrons through boundary snake-states. Many more electron-optical devices can be conceived based on confinement geometries defined by bipolar junctions. Further examples are discussed in the section 4.2 and section 4.3.

6. Edge state interferometers

In the previous section we saw that semiclassical arguments well describe transport in a wide range of magnetic field strengths, see figures 24(a)–(c). We now move to the quantum regime, when semiclassical skipping orbits and snake states break down and give way to fully formed quantum Hall edge channels—such channels exist wherever the electronic density changes enough for at least one Landau level to be crossed, which is for example the case both at the physical edge of the graphene flake and on each side of a p-n junction, see figure 28. We thus present electron quantum optics developments in graphene setups using such edge channels as waveguides. The first step is to outline the basics of quantum Hall transport. Fundamental concepts, including the physics of decoherence, will be introduced from a general perspective, while the peculiarities of graphene will be highlighted when necessary. The second step is a detailed review of different edge state interferometers realised in graphene, in particular Mach–Zehnder interferometers (MZIs) based on p-n junctions and Fabry–Pérot ones formed by QPCs, much as in 2DEGs. We also present some considerations, both experimental and theoretical, on decoherence effects in these experiments, and how they compare with their AlGaAs/GaAs counterpart.

6.1. Chiral edge electronics: theory essentials

The basics of integer quantum Hall transport can be understood within a single (quasi)particle picture via the Landauer-Büttiker formalism [74, 267]. In the simplest linear-response scenario, electrons injected from a given reservoir propagate phase-coherently and independently from each other along the available 1D edge channels—one for each filled Landau level—and are finally absorbed by a second reservoir. The conductances of arbitrary multi-terminal setups are obtained once the single-particle transmission amplitudes at the Fermi energy $t^{mn}_{\alpha\beta}$ are known, where $m\,(n)$ labels a given quantum channel from/into reservoir $\alpha\,(\beta)$. Numerous extensions of the formalism were worked out, *e.g.* to deal with non-linearities [268] in various contexts [269–272] or to consider AC transport and current fluctuations via Floquet scattering theory [273, 274]. Though simple[10], this approach provides a clear and remarkably well-working physical picture of edge transport. It is on this basis that some key concepts behind electron quantum optics eventually developed [32, 274, 277, 278]. In spite of its successes, this intuitive construction has limitations coming from its two main requirements: (i) idealised, featureless 1D chiral edge channels in one-to-one correspondence with bulk Landau levels; (ii) Fermi liquid premises, *i.e.* free quasielectrons propagating from reservoir to reservoir. Though fair initial assumptions, neither turns out to be particularly accurate.

Consider first the edge state problem, starting from a 2D system at $\mathbf{B}=0$. The sample edges are defined by a confining potential $\Phi(\mathbf{r})$, to which one can (semiclassicaly) associate a smooth local electronic density $n_0(\mathbf{r})$ which decreases to zero as it approaches the sides. Now let $\mathbf{B}\neq 0$. The textbook picture of adiabatically bending the Landau level energies $E_n(k)$ as they approach the sample sides [74]

$$E_n\,(k)\to E_n\,(k)-e\Phi\,(\mathbf{r}_k)\,,\ \mathbf{r}_k=(x_k,y)\,,\ x_k=kl_B^2, \qquad (45)$$

yields sharply defined 1D channels with velocity $v_n\sim\partial_k E_n(k)$, and an associated electronic density $n_B(\mathbf{r})$ which is discontinuous at each Landau level crossing. This is shown in figures 27(a)–(c). The smooth density profile at $B=0$, sketched in red, is massively distorted and becomes step-like when the magnetic field is switched on, $n_0(\mathbf{r})\to n_B(\mathbf{r})$. It was realised [279, 280] and formalised [281, 282] early on that this cannot be accurate: the electrostatically defined profile $n_0(\mathbf{r})$ can only be modified slightly in the presence of $\mathbf{B}$, since $\hbar\omega_c\ll|e\Phi_0|$. At the same time the Landau levels do not simply adiabatically bend. The qualitatively correct picture is shown in figures 27(d)–(f). It implies the formation of *compressible* $(\partial_n\mu\neq 0)$ electronic strips—the edge states—separated by *incompressible* $(\partial_n\mu=\infty)$ regions—the gapped Landau levels. The problem must be solved self-consistently, since the electrostatic potential, the electronic density and the spectrum

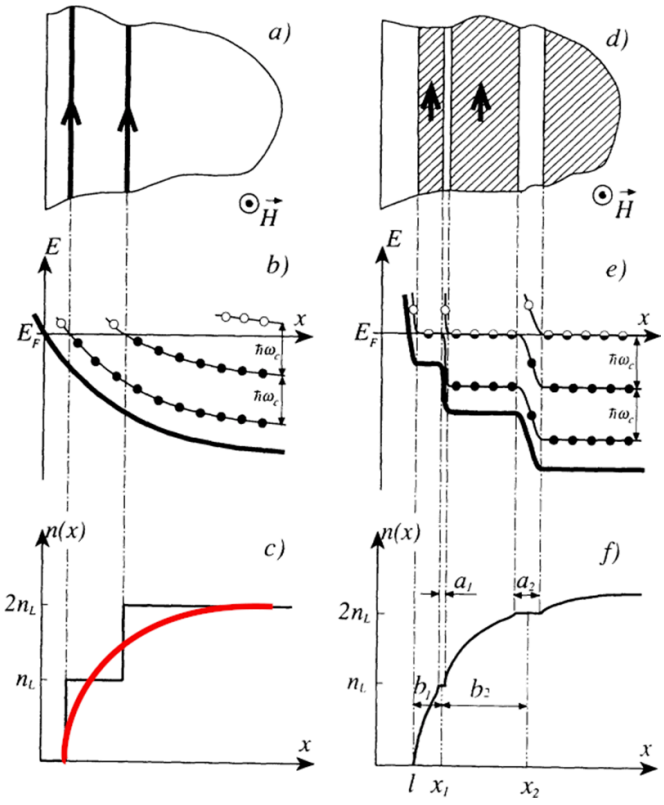

Figure 27. (a)–(c): Single-particle Landauer-Büttiker picture of widely-separated, exactly 1D edge channels. Arrows indicate the propagation direction. (d)–(f): Chklovskii-Shklovskii-Glazman self-consistent (Hartree) picture. Edge channels are compressible (shaded) strips of finite width a distance $b_i, i=1,2$ apart, separated by narrow incompressible (white) strips of width $a_i, i=1,2$. Reprinted (figure) with permission from [281], Copyright (1992) by the American Physical Society.

[10] Its simplicity is actually deceiving, as it hides numerous subtleties rooted in mesoscopic physics (non-locality of responses, role of contacts, invasiveness of probes…). See *e.g.* [275, 276] for some details.

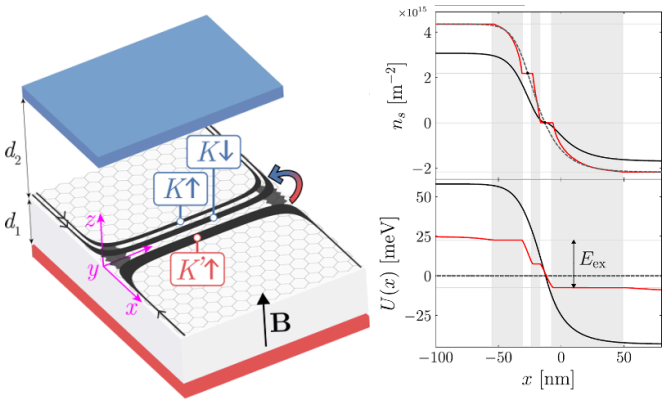

Figure 28. Edge channel structure at a graphene p-n junction. The top (blue) and bottom (red) gates define the junction and the filling factors ν, here $\nu = 2, -1$ respectively on the n and p side. The n and p quantum Hall channels are compressible regions of finite width (shaded gray in the right panel) running along the graphene edges and following the junction profile. They are labelled by valley (K, K') and spin $(\uparrow, \downarrow)$. The red curves in the right panel show the density and electrostatic profiles for $B = 9T, d_1 = d_2 = 20$ nm. Reprinted (figure) with permission from [284], Copyright (2022) by the American Physical Society.

form a set of coupled non-linear equations. The original construction by Chklovskii, Shklovskii, Glazman and Matveev [281, 282] was recently improved via self-consistent numerics [283] and in this form applied to graphene p-n junctions [284], see figure 28. It is a Hartree-level construction. What if non-local exchange (Fock) is also taken into account? Remarkably, in this case the bulk-boundary correspondence 'one edge state for each Landau level' does not necessarily hold [285]. This 'edge state reconstruction' was experimentally confirmed in different systems [286, 287], and recently further investigated [288, 289]. One concludes that the edge state properties of a quantum Hall droplet are less universal than those of the bulk topological phase. In particular, the edges have in general a non-trivial internal structure possibly hosting multiple co- and counter-propagating modes of varying width—which may also be more or less strongly coupled to one another, see below. This is a general conclusion, affecting both integer and fractional quantum Hall phases. In fact, since transport experiments probe edge state excitations, it is not always obvious how to relate these with excitations of the topological bulk, *e.g.* the fractionally charged quasiparticles of a fractional quantum Hall phase [279]. Note that full edge reconstruction with counter-propagating modes is expected to take place for smoothly confined quantum Hall droplets [285, 289], but the situation in graphene is varied, as it depends on how edges are experimentally realised. Pristine edges obtained by exfoliation can be sharp and clean, showing no sign of reconstruction [290, 291], while in etched samples the formation of incompressible strips is important [292], and counter-propagating modes were also observed [293]. Edges obtained by gating are clean but smooth on the l_B scale at higher fields [283, 284], so that full reconstruction cannot always be excluded *a priori*.

Let us now reconsider the Fermi liquid assumption. This is somewhat questionable for narrow edge states, since in 1D the Fermi liquid picture breaks down and is substituted by the Luttinger liquid one [294]. The breakdown is brought about by electron–electron interactions, whose critical importance in 1D can be formalised by the bosonisation procedure [295]. It turns out that the (almost) free quasiparticles of a 1D fermionic many-body state are not the quasielectrons of Fermi liquids, but collective bosonic modes, the simplest being charge density waves. Ideal 1D quantum Hall edge states are actually realisations of *chiral* Luttinger liquids, *i.e.* , Luttinger liquids hosting either only left- or only right-propagating modes. Explicitly, considering spinless electrons for simplicity's sake, the chiral (right) Luttinger model may be brought into the following basic form[11]

$$H_{cLL} = \sum_{\mathbf{q}>0} \hbar v_{\mathbf{q}} q \hat{b}^{\dagger}_{\mathbf{q}} \hat{b}_{\mathbf{q}}, \tag{46}$$

with $\hat{b}^{\dagger}_{\mathbf{q}}, \hat{b}_{\mathbf{q}}$ bosonic operators creating/annihilating collective density fluctuations propagating with velocity $v_{\mathbf{q}} \geqslant 0$, the latter depending on details of the electron-electron interaction.

An in-depth discussion of the Tomonaga-Luttinger low-energy model does not belong here [294–299]. It suffices to say that it is a standard starting point to study (time-dependent) quantum Hall edge transport [300, 301], though not always necessary [278, 302–304]. Indeed, the internal structure of the compressible edge strips (varying width, lack of perfect homogeneity) and the coexistence of different channels in close vicinity, see figures 27 and 28, remind us of the approximate nature of equation (46), and that strips are not ideal 1D objects. Their width should notably influence their character (Fermi vs. Luttinger) and the velocity of excitations propagating through them [283, 305], as well as posing fine practical problems in the definition of a surface they may enclose [306]. On the other hand disorder of different origins may cause phase transitions within the (quasi) 1D state, as well as enhancing inter-channel coupling [294, 301]. The latter is a fundamental point, as inter-channel coupling is a major source of decoherence in quantum Hall setups [307–312], together with intrinsic non-linearities of the 1D electron liquid beyond the ideal Luttinger construction [296, 298, 299].

Decoherence indicates the loss of phase memory of a quantum state. It is intimately related with *irreversible* loss of (quantum) information, which takes place whenever the quantum state interacts with additional entities—a heat bath, a fluctuating electromagnetic environment and so on—whose dynamics is beyond our control [275, 313]. The quantum state here is an electronic excitation propagating along an edge channel, be it of Fermi or Luttinger nature. Its phase-memory loss comes *e.g.* from interactions with a bath [314], which may explicitly be classical [302] or quantum [303, 315], or from intra-channel [305, 316] and inter-channel coupling [307–310, 312, 317].

To be definite, consider the case of inter-channel coupling in an ideal Luttinger liquid scenario. The propagating signal is an eigenmode of the Hamiltonian equation (46), thus

[11] See *e.g.* [294] for details.

by definition it never decays. In presence of a second chiral Luttinger strip coupled to the first by *e-e* interactions [305, 307, 318] the Hamiltonian becomes

$$H = H^1_{cLL} + H^2_{cLL} + \delta H^{12}_{ee}. \tag{47}$$

Consider an excitation propagating through the first Luttinger strip. If the second channel sits unbiased nearby it will act as a bath, which can be traced out breaking the unitarity of time evolution within the first channel. The dynamics induced by mutual coupling is however richer in general, since excitations become coherent objects spreading across two channels [304, 307, 318]. The latter may lose phase coherence by coupling to additional environment entities, *e.g.* other channels, the bulk, nearby gates. Notice that qualitatively similar conclusions would be reached if the strips were Fermi liquid in character. In fact, decoherence processes can be modelled quite effectively via phenomenological 'Büttiker probes', *i.e.* fictitious floating voltage probes which spoil phase memory without affecting the overall charge transfer [278, 319]. This widely employed approach is successful also in graphene [96], but obviously cannot provide substantial microscopic insight.

We have thus seen that the theory basis for electron quantum optics in the quantum Hall regime is the competition between electron-electron interactions (electrostatics and beyond) and the applied strong magnetic field. Specifically concerning graphene as a platform, some of its characteristics set is aside from traditional semiconductor systems. Besides its 'relativistic' Landau level spectrum, see section 2.1.2, two are of central importance: (i) the valley and sublattice internal degrees of freedom (isospin) and their locking to momentum; (ii) the finer control one has over electrostatics and specifically screening, since metallic gates can be very close to the transport sample. The latter is in particular a great advantage, since it allows to realise compact p-n interferometers and to effectively screen edge channels from the environment and each other, largely increasing the coherence length within each [320].

6.2. P-n junction based MZIs

The first observation of a graphene p-n junction based MZI was reported by Morikawa and coworkers in [321]. They have realized a p-n-p junction using two gate electrodes. At high magnetic fields edge states form which propagate along the sample edges, and the outermost electron and hole edge states, corresponding to filling factor 2 and -2, merge at the p-n interface where they co-propagate at $\nu = 0$, as shown in figure 29(a). However, if as written in section 2.1.2, the interactions split the lowest Landau level up, at lower field or moderate interaction strength, into a doublet (K and K') then the edge states at the p-n interface will move away from the interface to regions where the doping corresponds to $\nu = \pm 1$ (separating gapped bulk regions of $\nu = 0$ and $\nu = \pm 2$). This is shown in panel (b) of figure 29. As a result, co-propagating edge states are formed at the p-n junction. If there is no coupling of these edge states, this would lead to an insulating behaviour in transport measurements. As long as these edge states

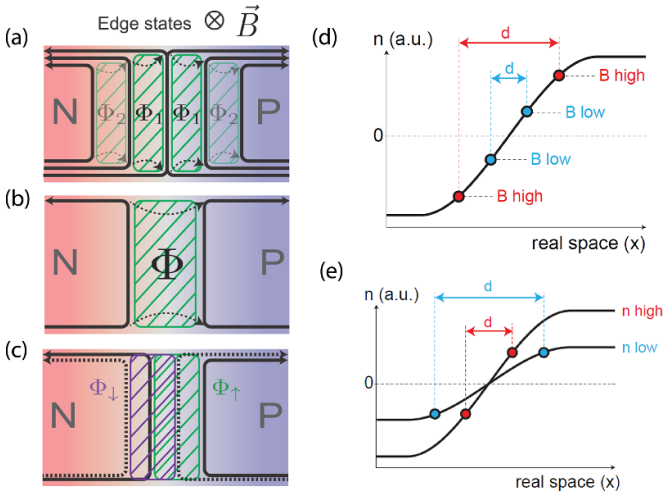

Figure 29. The formation of MZ interferometers in graphene p-n junctions. (a) Edge states along a p-n junction, with an electron–hole like edge states propagating along the p-n junction. Scattering between the channels is possible at the edges. Green dashed line mark possible MZ interformeter areas. (b) For larger fields the lowest LL is split up and the gapped region between electron and hole trajectories gives the interferometer's area. (c) If spin spilitting is present mixing is only possible between states with the same spin. (d) The positions of the edge states, which reside at a given filling factor along the p-n junction are marked with small circles with at two different magnetic fields. (e) Position of the edge states is shown for two different dopings. Reproduced with permission from [69].

are close (smaller magnetic field) the coupling along the full length of the p-n interface will result in an oscillating motion of electrons originating from the source electrode, which is the quantum description of the quasi-classical snake states. Edge states with larger filling factor on both sides can participate in the formation of quasi-classical trajectories [95]. As the magnetic field is increased, the edge states become separated in the bulk, but as was suggested by Morikawa and coworkers they can be coupled at the bottom and top edge of the sample, as shown in figure 29(b), and hence an interferometer loop can be formed. This interference loop results in an oscillating conductance, where the conductance maxima is separated by a change of flux quantum within the loop. Therefore one expects that the conductance maxima follows lines on gate-gate or gate-magnetic field maps, where the flux within the interference loop is constant.

For simplicity, let us assume, that a symmetric, smooth p-n junction is formed. In this case, by increasing the doping on the two sides, the density gradient at the p-n junction increases, therefore the edge states which reside at fix filling factor move inward, as shown in panel (f) of figure 29. In order to keep the flux constant, the magnetic field has to be increased. Without a detailed derivation, this leads to parabolic-like oscillation maxima in the conductance in gate-magnetic field maps, as can be seen in figure 30(a). Using similar arguments, it can be shown, that for constant magnetic field if one of the gate voltages is changed, to keep the area constant the other gate needs to be used for compensation, leading to hyperbolic lines in the conductance in gate-gate maps as shown in figures 30(b)–(d).

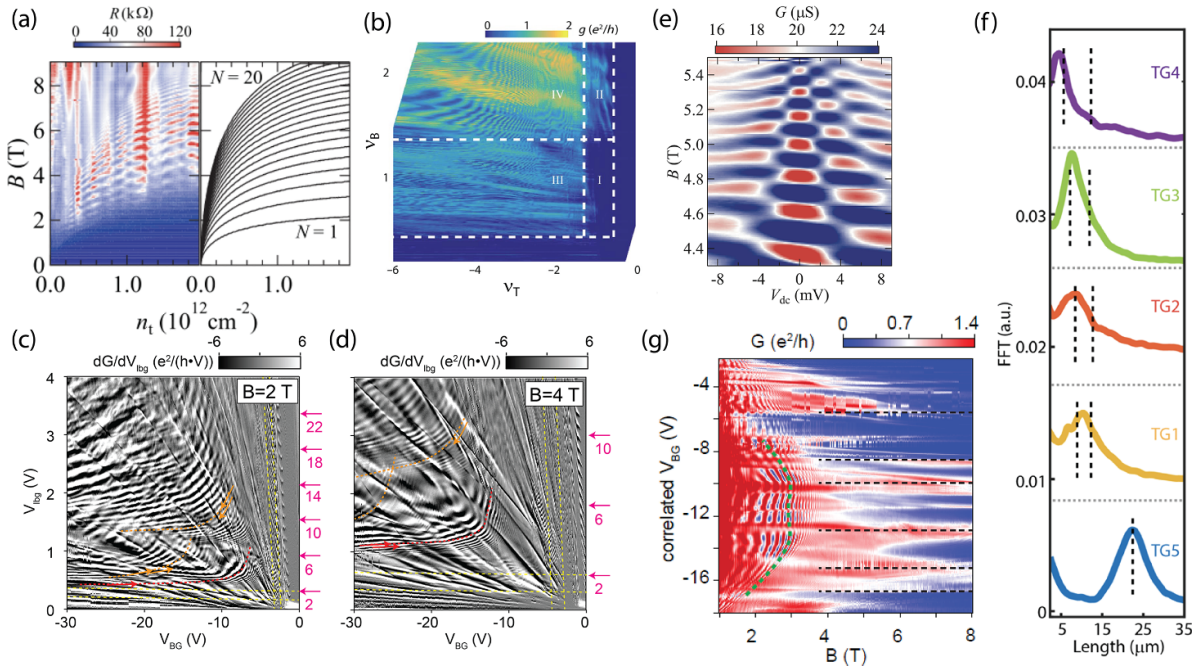

Figure 30. First graphene based MZ interferometers. (a) Magneto-resistance oscillations dispersing as a function of B-field and doping. Simple calculations reproducing the findings based on the edge state positions is shown in the right [321]. (b) Magneto-conductance oscillation as a function of the filling factors on the two sides of the p-n junction [322]. (c) and (d) Similar features shown from [95] in 2 and 4 T magnetic field, respectively, as a function of the two gate voltages. The derivative of the conductance is shown to highlight the oscillations. Different oscillations marked with different colors are attributed to different origin. (e) Bias dependence of the magneto conductance oscillation as function of magnetic field demonstrating a checkerboard pattern [321]. (f) Oscillation periodicity for MZ oscillations is extracted for different samples, and the from that the length of the interferometer is calculated, matching nicely the dependence on p-n junction length [322]. (g) Magnetoconductance oscillations attributed to valley-isospin physics shown in gate-B-field maps with horizontal lines. For this figure the gate voltage is tuned such that only the p-n junction position is changed, whereas the potential profile remains the same [323]. (a) Reprinted from [321], with the permission of AIP Publishing. (b), (e), (f) From [322]. Reprinted with permission from AAAS. (c) and (d) Reprinted (figure) with permission from [95], Copyright (2018) by the American Physical Society. (g) Reprinted with permission from [323]. Copyright (2017) American Chemical Society.

If the magnetic field or the interaction strength is further increased then the lowest Landau level splits further. In this case, spin and valley split edge states co-propagate along the p-n interface (figure 29(c)). Since spin-scattering is prohibited even on the edge of the sample, only edge states with the same spin can mix. This was first observed by in [322] (figure 30(b)) and later in [95] (panels (c)and (d)). The Mach–Zehnder interpretation was also corroborated in [322] by investigating interferometers with different p-n junction lengths leading to different oscillation periodicity (figure 30(f)). Finally, the bias dependence of these oscillations was also studied, for which an example is shown in figure 30(e), more details can be found in [95, 321, 322]. We note that even in the non-split Landau level case (figure 29(a)) Aharonov–Bohm oscillations are possible between, e.g. the lowest and higher lying Landau levels. Since all these different MZ oscillations and the snake states give similar signatures in both magnetic field-gate and gate-gate maps, see, e.g. all the oscillations in figures 30(c) and (d) with different colors, their identification is possible only based on further bias or temperature dependent measurements. Whereas snake states can be observed up to 100 K, MZ oscillations disappear at few Kelvins or below. Finally we would draw the attention to another set of very prominent oscillations which stem radially from the charge neutrality point (marked by black dashed lines in figure 30(g)). As seen in panel (g) they seem to be magnetic field dependent. Along such lines and the position of the p-n junction is fixed and these oscillations have been attributed to valley-isospin oscillations probing the microscopic character of the edges [323]. This is discussed in the next section.

6.3. *Tunable Mach Zehnder inteferometers*

A controlled approach to achieve Mach-Zehnder interferences was demonstrated in a recent study [324] where electronic beam splitters were utilized, leveraging the valley degree of freedom in graphene. The concept of valley beam splitters builds upon theoretical work by [325, 326] and earlier experimental work of [323, 327], where the crystalline structure at the corner of a graphene p-n junction enables electron scattering between p-n interface channels with opposite valley polarizations of quantum Hall edge channels. In the experiment, the researchers employed small electrostatic side gates to tune the mixing point of the edge channels along the edge of the graphene flake, thereby controlling the scattering process. This allowed for the reliable modulation of electronic transmission through the valley beam splitters, ranging from zero to near unity. Notably, this work demonstrated the complete tunability

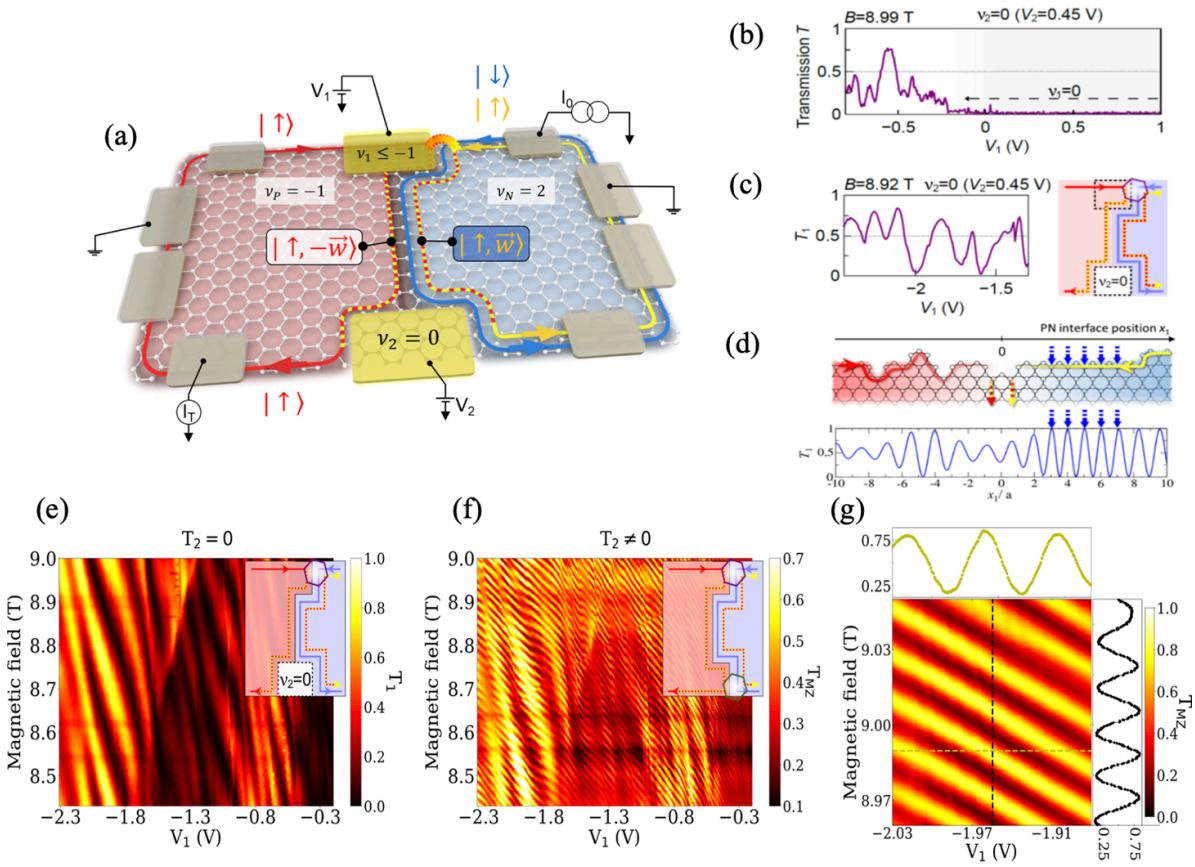

Figure 31. (a) Schematic of a fully tunable Mach–Zehnder interferometer using valley degrees of freedom of graphene [324]. (b) Measured transmission T_1 of the top valley splitter as a function of the side gate voltage i.e controlling the filling fraction below it. (c) Oscillation of transmission of a valley splitter. Right panel: The edge state configuration in this condiction. (d) KWANT simulation of transmission (T_1) as a function of the position along the p-n interface. (e) Measured T_1 as a function of gate voltage and magnetic field. (f) Transmission in the MZ interferometer configuration (T_{MZ}) when both (top and bottom) the splitters are allowed to have valley mixing. (g) T_{MZ} as a function of magnetic field and gate voltage. Reprinted (figure) with permission from [324], Copyright (2021) by the American Physical Society.

of Aharonov–Bohm (AB) interference by adjusting the side gate voltage and magnetic field. The resulting AB oscillations exhibited stability and reproducibility.

The sample schematic is depicted in figure 31(a), illustrating an encapsulated graphene in a bipolar quantum Hall state. In the N region, the Landau-level filling factor is $\nu_N = 2$, resulting in two counterclockwise circulating channels with opposite spins ($\uparrow$, $\downarrow$) along the boundary. On the other hand, the p region has a filling factor of $\nu_P = -1$, featuring only one clockwise circulating spin-down channel.

When an injected current of $I_0/2$ carried by spin-down carriers is introduced, it can interact with the edge current flowing from the p region. Consequently, this interaction leads to a contribution to the transmitted current I_T. The flow of the spin-down current is regulated by splitting it into p-n interface channels that possess opposite valley isospins [328]. After the physical top edge of graphene intersects with the electrostatically defined p-n interface, the current proceeds along either the p -side or the n -side of the interface. The transmission probability along the P -side is denoted as $T_1 = |t_1|^2$, while the reflection probability on the N side is given by $|r_1|^2 = 1 - T_1$. In the presence of a strong perpendicular magnetic field, the valley degeneracy is lifted, as discussed in section 2.1.2. As a result, the currents on the n -side and p -side exhibit opposite valley isospins, represented as $\pm\vec{w}$. The probability T_1 reflects the degree of valley-channel splitting, which can be described by a quantum-mechanical superposition.

$$|\Psi_{\text{initial}}\rangle = r_1|\uparrow,\vec{w}\rangle + t_1|\uparrow,-\vec{w}\rangle. \tag{48}$$

At the n-side interface, the spin-up state is represented as $|\uparrow,\vec{w}\rangle$, while at the p-side interface, it is denoted as $|\uparrow,-\vec{w}\rangle$. The valley-isospin undergoes a change from that of the top edge channel to $\pm\vec{w}$, resulting in a significant momentum shift. This change is attributed to the atomic structure at the intersection [326].

By applying voltages to the side gates, they could modify the electrostatic potential profile at both ends of the p-n interface, as depicted in the schematic diagram figure 29. In a recent investigation employing the Chklovski-Shklovskii-Glazman formalism, the precise positioning of edge states in a graphene p-n junction was determined through rigorous quantitative calculations [284]. When the filling factor below a side gate was set to $\nu \leqslant -1$, the p-n junction intersected the physical edge, creating a sharp potential change at the atomic distance scale. This sharp potential change facilitated the mixing of the

valley channels. On the other hand, by setting the filling factor to $\nu = 0$, the p-n junction intersected an electrically defined edge where the potential landscape was smooth, resulting in no change in valley isospin. Through the manipulation of these side gates and the associated filling factors, the researchers could control the extent of valley-channel splitting and restrict the mixing of valleys. This allowed for precise control over the transmission probability and the preservation of valley isospin within the system.

The authors of this study first demonstrated the ability to tune the transmission probability T_1, defined as the ratio of transmitted current I_T to half of the injected current $I_0/2$. This tuning was achieved by adjusting the voltage V_1 applied to the top side gate, as shown in figure 31(b). To achieve valley-channel splitting at the top intersection while suppressing it at the bottom, they set the filling factor ν_1 below the top side gate to $\nu_1 \leqslant -1$, and ν_2 below the bottom side gate to $\nu_2 = 0$. When a positive non-zero voltage was applied to V_1, it resulted in $\nu_1 = 0$, ensuring that the edge channels only intersected at electrostatically defined edges without valley-channel splitting, leading to a vanishing transmission. Conversely, for $V_1 < 0$, they ensured $\nu_1 \leqslant -1$, causing the p-n junction to intersect the top physical edge. This enabled valley-channel splitting and resulted in a finite transmission. Subsequently, the authors demonstrated the full tunability of the transmission probability T_1 from zero to nearly unity, as depicted in figure 31(c), by varying the voltage V_1. Importantly, they also showed that T_1 could be tuned by changing the magnetic field, as illustrated in figure 31(e). The period of the dependence on V_1 was estimated to be around $\Delta V_1 \sim 100$ meV on average. It was calculated that this change in voltage caused the p-n interface to shift by approximately $\sim$1 nm below the top side gate. The period of the magnetic field (B) dependence was found to be $\Delta B_1 \sim 300$ mT, corresponding to a change of approximately $\sim$0.2 nm in the magnetic length at $B = 9.2$ T. These length scales are comparable to the interatomic distance of pristine graphene (approximately 0.142 nm) and the period of atomic edge structures (e.g. 0.246 nm for the zigzag edge), but significantly shorter than the spatial variation of the electrostatic potential induced by gate voltage. This strongly suggests that the transmission probability T_1 can be controlled by the atomic structure at the top intersection. The shift of the p-n interface, estimated from experimental data, was made possible by independent control of the top and bottom side gates, which was not achievable in previous works [322, 323]. Similar experiments were conducted with the bottom side gate, yielding a comparable physical scenario and trend in the results. In the transmission results, some irregular but reproducible oscillations were observed. These oscillations were attributed to the roughness in the upper physical edge of the graphene. The theoretical simulation using KWANT simulations, as depicted in figure 31(d), supported this explanation. Overall, the experiments and simulations provided strong evidence that the transmission probability T_1 in the system could be controlled by the atomic structure at the top intersection, and the observed irregularities in the results were attributed to edge roughness effects.

Finally, the investigated the MZIs by utilizing both the top and bottom valley splitters. The edge channels from the two sides of the p-n junction acted as the arms of the interferometer, while the valley splitters served as the beam splitters, as illustrated in figure 31(f). Notably, smaller-scale Aharonov–Bohm oscillations were observed with a magnetic field period of approximately 25 mT. The area of the interferometer was calculated to be 0.15 μm^2, indicating a separation of around 110 nm between the edge channels. This separation is attributed to electron-electron interactions. When both valley splitters were set to a half-transmission configuration, the interferometer exhibited regular oscillations, as depicted in figure 31(g). The visibility of the MZIs, defined as $(T_{max} - T_{min})/(T_{max} + T_{min})$, was approximately 60%.

The paper also discussed the coherence properties of the valley-split state in relation to the energy of the transported electrons. A lobe pattern was observed in the transmission probability T_{MZ} as a function of the bias voltage, which is a typical behavior in MZIs fabricated in conventional GaAs heterostructures. The microscopic origin of this lobe pattern is now well understood and discussed in detail in the [320]. Moreover for the graphene MZI studied in these works, the value of V_{lob} was found to be 210 μeV, which is relatively large compared to the reported value of 20 μeV for MZIs fabricated in GaAs/AlGaAs heterostructures. This suggests that the graphene MZI exhibits robust phase coherence over a wider energy range.

This robustness of phase coherence of graphene MZI has been harnessed recently to demonstrate coherent phase manipulation of periodically injected single electronic state [329]. This development opens up further avenues for exploring electronic experiment analogous to optics in graphene platform.

6.4. Decoherence and relaxation in quantum Hall MZIs

Single electron coherence in quantum edge channels is notably highlighted by Mach–Zehnder interferometry experiments. But it also digs up a number of questions on the electron decoherence mechanism in these systems. A large majority of experiments dealing with quantum Hall interferometers in conventional semiconductors suffers from decoherence, which can come from different sources like edge reconstruction due to the presence of impurity [285], inter-edge interaction [330, 331] and intra-edge Coulomb interaction [307, 332, 333]. Most of the time, those interactions are intertwined which makes it hard to address them separately. Within the last decade, the majority of experimental and theoretical works addressed the issue of inter-edge interaction [39, 300, 301, 307–310, 312, 315, 332, 334–348] but there is still an ongoing debate about the observed results. One possible way out is demonstrated in [320] by using a fully tunable graphene MZ interferometer utilizing p-n junctions. In the experiment, three interferometers of different lengths (figures 32(a)–(c)) were studied, showing a persistence of the interferences up to 1.6 K, relatively high compared to the operating temperature of GaAs interferometers. The visibility of the interferences, as shown in figure 32(d), was shown to have two distinct regimes

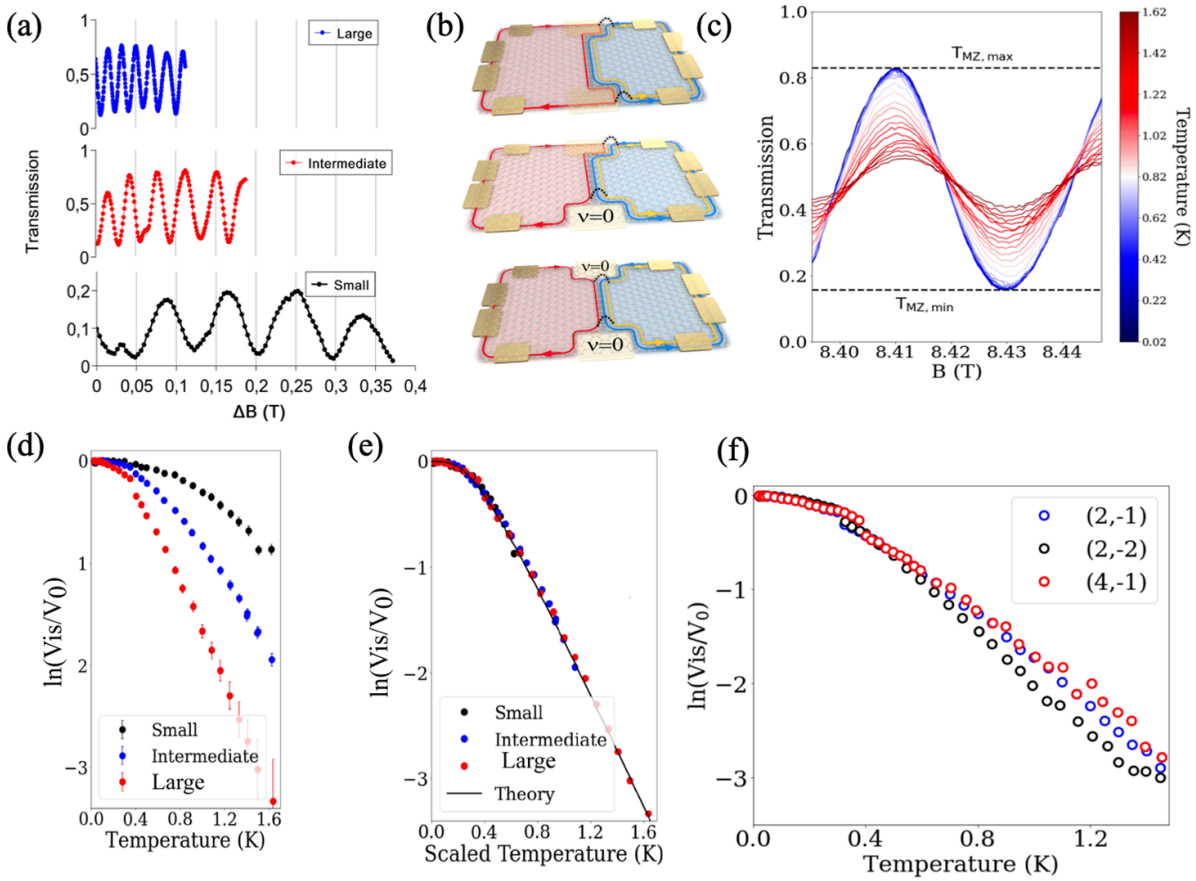

Figure 32. (a) AB oscillation in three MZ interferometer of different lengths. (b) The schematic of channel mixing points in the interferometer. (c)Temperature dependence of the transmission for the large interferometer. (d) Visibility decay of with temperature for all the interferometer. (e) universal scaling behaviour of visibility. (f) Visibility decay profile in presence of different number of edge channels. Reproduced from [320]. CC BY 4.0.

in temperature. Visibility decay is found to be algebraic instead of exponential below 1 K which signifies the suppression of thermal route of decoherence. This 'new-found' algebraic decay regime was not observed before in conventional semiconductor system, and it does not depend on the different configurations (e.g. different edge configurations of p and n side) of the interferometer. Electron heating giving rise to this kind of scaling behavior was ruled out by careful measurement of thermal noise at each temperature confirming the electrons to be well thermalized. Interestingly, the decay profile for all the three interferometers lies on a single curve (figure 32(e)) if plotted against a scaled temperature LT/L_0 where T is temperature, L is the interferometer length, and L_0 is the length of the large interferometer. This scaling behaviour is in good agreement with an intra-channel interaction model. To access the effect of the presence of adjacent edge channels, the temperature dependence of interference visibility was monitored by changing the number of edge channels which is shown in figure 32(f). The short-range inter-channel interaction fractionalizes the electron flow in fast and slow modes which causes decoherence. No significant change in decay profile was observed, indicating the absence of influence of inter-edge channel interaction mechanisms. In a van-der-Waals architecture, the possibility to position the electrostatic gates very close (vertical distance 30 nm) to the 2DEG provides screening between nearest edge channels. Therefore, the decoherence mechanism due to inter-edge channel interaction can be efficiently suppressed and one can only talk about the intra-edge channel interaction.

Moreover, at high bias, magnons can be emitted which are also a source of decoherence [328, 349].

6.5. *Graphene QPCs in the QH regime*

Quantum points contacts realized in conventional 2DEGs rely on the ability to deplete the electron gas locally using electrostatic gates. This is not possible in single layer graphene at zero magnetic field since in this condition graphene is gapless. Under a high magnetic field, one can rely on the gap between different Landau levels to locally confine the edge channels with gates until backscattering occurs between the two counter propagating edges. An order of magnitude of these gaps is given by recent measurement conducted at 4 T and 1.4 K, estimating broken symmetry state gaps to be about 100 meV [353]. This QPC technique under strong magnetic field has been implemented in several recent experiments both in the integer [91, 350, 354] and in the fractional QH regime [351, 352, 355, 356]. Typical geometries are depicted in figure 33.

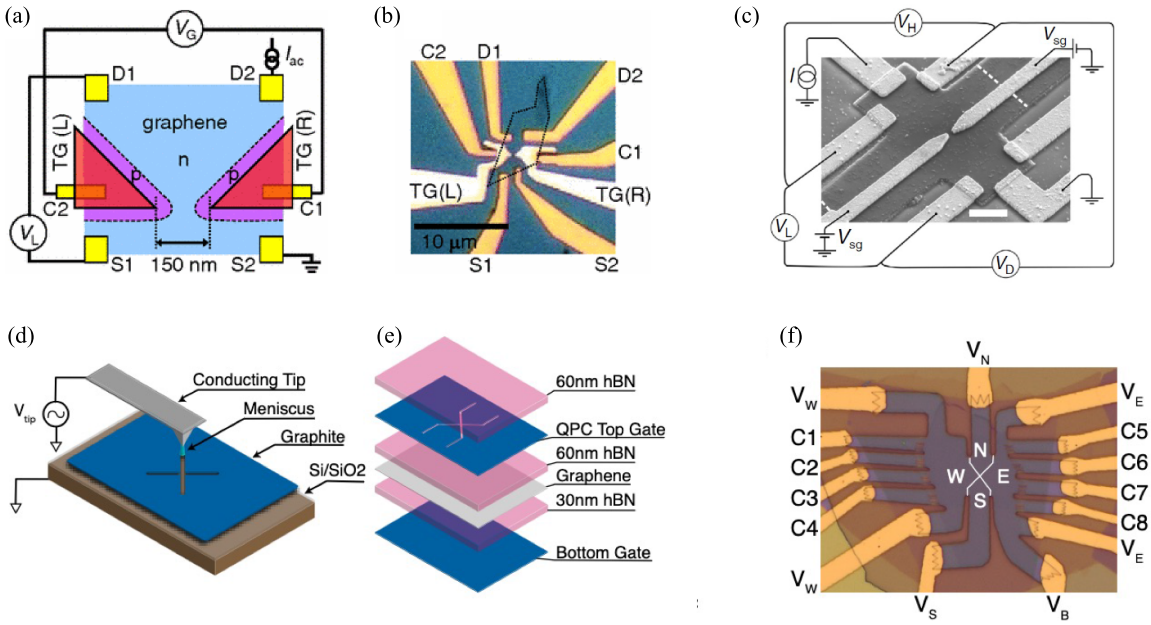

Figure 33. Graphene quantum Hall QPC devices. (a) and (b), First generation reported in [350], where a thin layer of aluminium oxide is used to separate the gates from the graphene flake deposited on a SiO2 substrate. (a), device schematics and (b) optical micrograph of the sample. (c) Scanning electron micrograph of a QPC realized in hBN-encapsulated graphene [351], with metallic QPC gates deposited on the surface of the hBN/graphene/hBN stack. (d), (e) and (f) high-mobility, dual graphite gates devices reported in [352], where the top graphite gate is divided in 4 regions by anodic oxidation (d). (e) stack structure and (f) optical micrograph of the sample. The regions denoted *N* and *S* correspond to the QPC gates. (a) and (b) Reprinted (figure) with permission from [350], Copyright (2011) by the American Physical Society. (c) Reproduced from [351]. CC BY 4.0. (d)–(f) Reproduced from [352], with permission from Springer Nature.

QPC split gates, made of either metal or thin graphite flakes, are fabricated on top of an hBN-encapsulated graphene flake, and are biased with a dc voltage such that the quantum Hall states below them is set to a filling factor smaller than the bulk filling factor, thereby expelling the edge channel from beneath. The filling factor of the bulk is tuned using a global back gate (usually in graphite) combined with additional graphite top gates in [352, 355, 356]. The distance between the split gates is typically about 100 nm. In [352, 355, 356], the QPC and bulk top gates are realized from a single top graphite flake divided into the local gates by either reactive ion etching as shown in figure 35(c) [355] or by local anodic oxidation using an AFM tip as shown in figures 33(d)–(f) [352, 357] .

Typical QPC characterization, shown in figure 34, consists in maps of the electric conductance across the QPC measured as a function of both QPC gate voltage and back/top gate voltage. They show regions of quantized conductance, corresponding to an integer number of channels perfectly transmitted across the QPC. When applying larger negative voltage on the QPC, a depleted region is first created below the gate. At higher voltages this region become populated with negatively charged carriers leading to an effective p-n-p barrier. In earlier devices [91, 350, 354], equilibration among channels in p and n regions led to an effective short cut of the split gates who could then not work as a QPC. These devices thus required the filling factor below the top gate to be fixed at $\nu = 0$, the gap of which prevents equilibration across the gate. Because of the finite density range over which $\nu = 0$ is defined, the QPC gate voltage could only be tuned in a limited range (typically, $\Delta V_{\mathrm{QPC}} \sim 100$ mV at 5 T, for an approx. 50 nm thick BN). The global back gate and additional top gates were thus tuned in combination with the QPC gates, such that the electrostatic potential at the saddle point is raised or lowered while the filling factor below the QPC gates, and in the bulk of the sample, are fixed. This leads to configurations typically depicted in figures 34(g)–(i), where an integer number of edge channels can be ballistically transmitted across the QPC in a controlled fashion, leading to the conductance plateaus shown, e.g., in figure 34(f). The condition for the split gates to operate correctly as a QPC in these early devices depending on the carrier concentration below the gate and a critical magnetic field has been extensively studied for example in [61]. Most recent devices with higher mobility and operating at higher field do not present signs of equilibration [351, 352, 355, 358]. In particular, they show extended regions of zero conductance, demonstrating the ability to effectively pinch those devices thanks to the different quantum Hall gaps and even in the absence of an intrinsic bandgap.

The ideal point contact signature has been the subject of debates in the GaAs community recently [359–361]. While these discussions focused on the use of QPCs for shot noise measurement, similar questions arise for the use of QPCs for interferometry, and it is not clear whether a QPC which is ideal for all measurements exists (or is even possible). Notably, a recent article showed for the first time tunneling measurements across a QPC between edge channels at filling factors $\nu = 1$ and $\nu = 1/3$, and observed the scaling laws for the bias

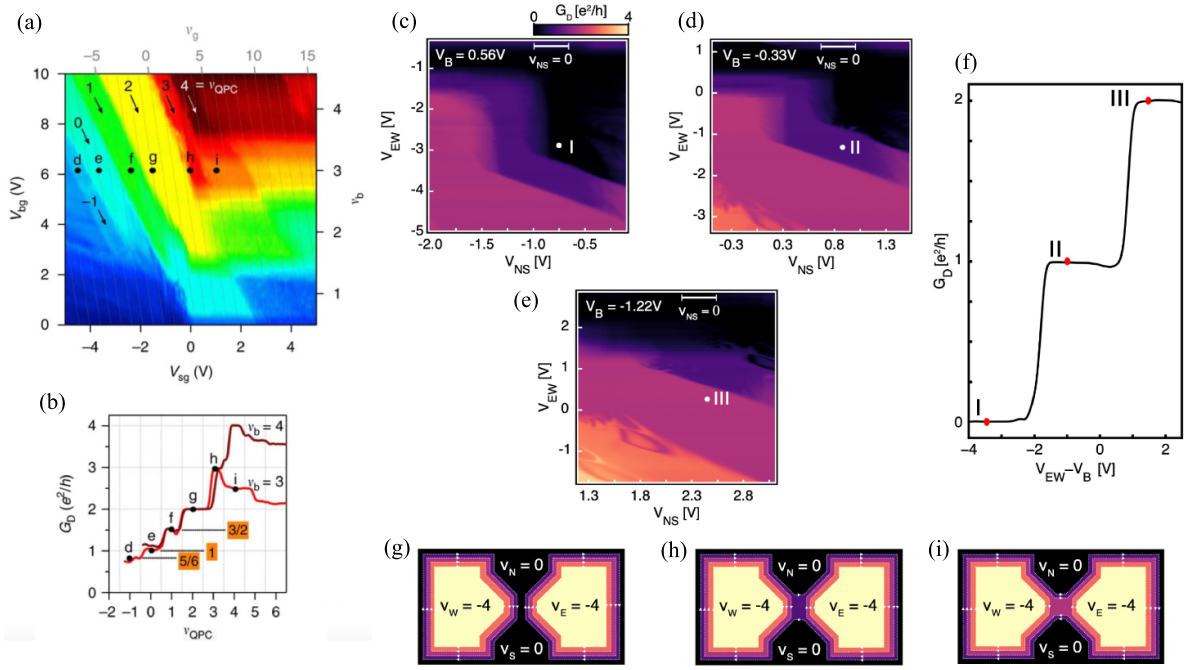

Figure 34. Conductance measurements in graphene QPCs. (a) conductance map of the QPC realized in [351], as a function of the back gate (V_{bg}) and QPC gate (V_{sg}) voltages. (b) line cuts of the data plotted in (a) at fixed back gate voltage, showing the quantized conductance plateaus. (c), (d) and (e) conductance map of the QPC realized in [352] as a function of the bulk top gates ((V_{EW}) and QPC gates (V_{NS}) voltages, for 3 different values of the bulk back gate (V_B) voltage. The white bar indicates the QPC gate voltage range over which the filling factor below the QPC gates is $\nu = 0$. (e) line cut of the conductance data as a function of a combination of the bulk top and back gates, showing the quantized conductance plateaus. (g), (h) and (i) schematic representation of the filling factors in the vicinity of the QPC corresponding to the points marked I, II and III in (c)–(f). (a) and (b) Reproduced from [351]. CC BY 4.0. (c)–(i) Reproduced from [352], with permission from Springer Nature.

and temperature dependence of the tunneling conductance predicted by the Tomonaga-Luttinger liquid theory [356].

6.6. Quantum Hall FPIs

6.6.1. Principle of the FPI experiment. The quantum Hall Fabry–Pérot interferometer (FPI) is a pivotal tool for accessing the exchange statistic of exotic quasiparticles and realizing anyonic braiding [363, 364]. In analogy with optical FPI, where semi-transparent mirrors reflect the incident light back and forth and enable photon interference, QPCs are utilized as electron beam splitters to backscatter the chiral edge channels of the quantum Hall states. The electronic QH FPI can be built with two QPCs in series in a two-dimensional electron gas in semiconducting heterostructures or 2D materials in the QH regime, where selective partitioning of the edge channels leads to interferences. In this configuration, interference of electrons propagating along the periphery of the cavity can be controlled by the Aharonov–Bohm phase $\varphi_{AB} = 2\pi AB/\phi_0$, where A and B are the enclosed area and magnetic field, and $\phi_0 = \mathrm{h/e}$ is the magnetic flux quantum.

Historically, this type of interferometer was first realized in a 2D electron gas embedded in GaAs/AlGaAs quantum wells [365–369]. However, the presence of charging effects between the edge modes and the compressible bulk has long hindered the measurement of the Aharonov–Bohm phase, not to mention the exploration of braiding statistics [31, 368–370]. Recently, new GaAs heterostructures, purposely designed to mitigate charging effects by incorporating additional quantum wells serving as screening layers, have enabled the long-awaited observation of Aharonov–Bohm interference of a 1/3 fractional QH edge [40, 369] and subsequently at filling factor 2/5 [371]. Nevertheless, the quest for smaller interferometers with negligible charging energy is fervently pursued for practical applications.

Graphene-based van-der-Waals heterostructures offer a promising alternative platform for realizing QH FPI due to their intrinsically advantageous dielectric environment. The presence of a graphite backgate, typically positioned in close proximity ($\sim 20 - 60$ nm) to the graphene, naturally provides electrostatic screening, which effectively reduces the device's charging energy. Moreover, crystallographic edges create a hard-wall potential, limiting possible edge reconstructions [291] that might otherwise generate undesired additional integer, fractional and even neutral modes. These neutral modes are known to be detrimental to coherence [287].

Recently, monolayer and bilayer graphene-based FPIs have been successfully fabricated. We review here the various strategies employed in the design of interferometers with minimal charging energy, as well as the observation of Aharonov–Bohm conductance oscillations in the integer quantum Hall regime [198, 355, 358].

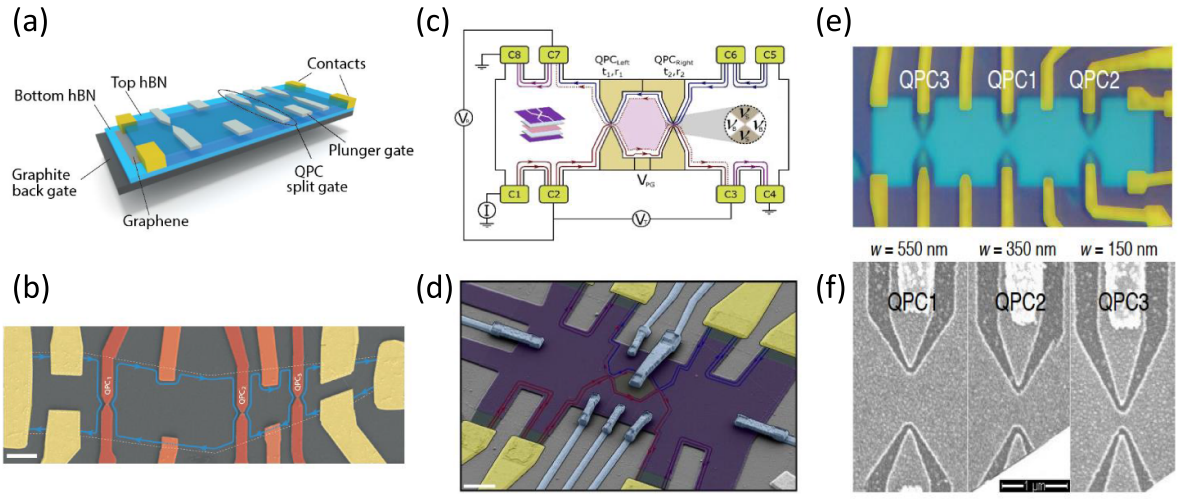

Figure 35. Quantum Hall Fabry-Pérot interferometers. (a) Schematic and (b) SEM image of the device studied in [358]: 1D Ohmic contact made by Cr/Au, QPC split gates and plunger gates are made by depositing Pd electrodes on the hBN top flake. (c) Schematic and (d) SEM image of the device studied in [355]. QPC and plunger gates are made by selectively etching the uppermost graphite flake. (e) Optical image and (f) SEM image of the device studied in [362]. QPC and plunger gates are made by etching both the top h-BN and the graphene flake. (a) and (b) Reproduced from [358], with permission from Springer Nature. (c) and (d) Reproduced from [355], with permission from Springer Nature. (e) and (f) Reprinted with permission from [362]. Copyright (2022) American Chemical Society.

6.6.2. Monolayer graphene based FPI. Figure 35 illustrates representative graphene-based devices. These heterostructures consist of h-BN encapsulated graphene deposited on top of a graphite backgate as detailed in [355, 358]. Two distinct technical approaches have been employed to define the FPI cavity for quantum Hall edge channels. In the first approach, the physical edge of graphene, in conjunction with QPCs and plunger gates made from Pd deposited atop the uppermost h-BN, were used by Déprez and coworkers [358] as shown in figures 35(a) and (b). Plunger gates placed between the QPCs manipulate the electron trajectory, enabling the modulation of the interference loop area. Multiple FPIs can be constructed by incorporating additional QPCs, as shown in figures 35(a) and (b), where three QPCs define three cavities of different sizes. A second approach, developed by Ronen and coworkers [355], involves an additional graphite layer on top of the hBN heterostructure. This layer is locally etched to establish QPC and plunger gates (as depicted in figures 35(c) and (d)). The interferometer cavity is thus entirely determined electrostatically through these top-gates. These gates offer the flexibility to tune the smoothness of the electrostatic edge potential, thereby enabling a modulation of the edge channel velocity. Last, Zhao and coworkers [362] implemented a similar device where the QPCs are constructed by etching both graphene and top h-BN layer.

A standard measurement setup, as shown in figure 35(c), is commonly used in most experiments [355, 358]. The measurement of the longitudinal or diagonal resistance of the FPI are performed using lock-in amplifiers.

The new interesting aspect of the graphene platform lies in the extensive tunability provided by the plunger gate. In contrast to GaAs heterostructures, where the plunger gate tunability is constrained by the depletion of electrons beneath the gate, graphene's gapless band structure allows for a broad gate sweep covering multiple quantum Hall states and filling factors. Figure 36 illustrates characteristic resistance oscillations with high visibility across a wide voltage range. Applying a negative voltage to the plunger gate depletes the electron gas and eventually accumulates holes beneath the gate. Consequently, the electron trajectory is continuously pushed toward the device interior with decreasing plunger gate voltage (see figure 36(d)).

Graphene-based FPIs exhibit less charging effect compared to GaAs-based ones of similar sizes. Figures 37(a) and (b) depict 2D plots of the resistance R_{D} as a function of both magnetic field and plunger gate voltage for the outer channel interference of two interferometers of different sizes ($A = 3.1\ \mu\mathrm{m}^2$ and $A = 14.7\ \mu\mathrm{m}^2$). Effective interferometer areas (A) calculated from magnetic field periodicities (ΔB) using the formula $A = \phi_0/\Delta B$, are found to be in excellent agreement with area defined by lithography. The periodic stripes in the plot correspond to lines of constant phase. The direction of these lines is used to distinguish whether the interference is dominated by Aharonov–Bohm effect or Coulomb interactions [364]. A constant Aharonov–Bohm phase results in stripes with a negative slope due to the diminished area being compensated by an enhanced magnetic field, as expressed by the equation $\Delta\varphi_{\mathrm{AB}} = 2\pi/\phi_0(B\Delta A + A\Delta B) = 0$. The observed negative slopes in figures 37(a) and (b), along with the accurate estimation of interference area, provide clear evidence that these interferometers are operating in the Aharonov–Bohm regime. It is noteworthy that GaAs-based interferometers of similar size were reported to be dominated by Coulomb interactions [31].

Edge velocity can be probed through the oscillation dependence on both the DC bias voltage and the temperature. When a source-drain DC bias voltage is applied, electrons experience a dynamical phase shift given by

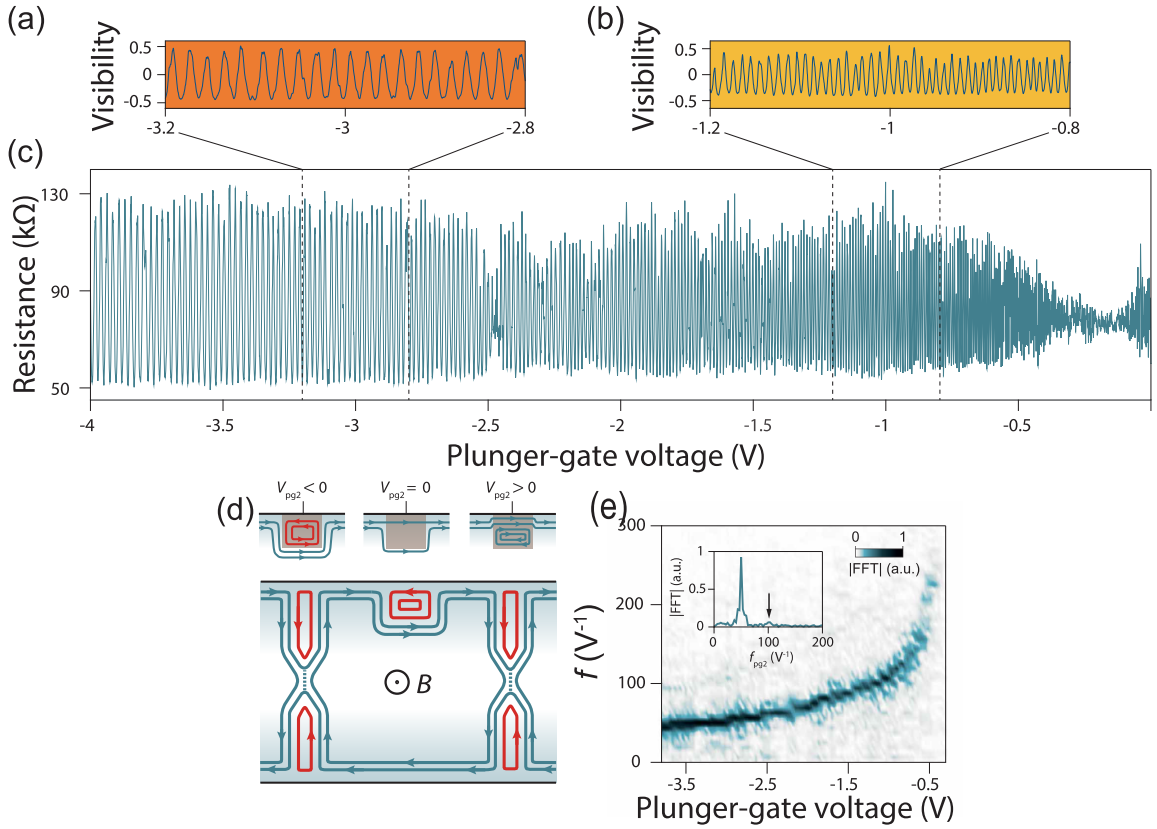

Figure 36. Plunger gate dependant oscillations. Resistance oscillations of outer channel of $\nu = 1.5$ at $B = 14$ T.Plunger gate voltage sweeps from -3.2 V to -2.8 V in (a), from -1.2 V to -0.8 V in (b) and from -4 V to 0 V in (c). (d) Schematic of the edge channel position at different plunger gate voltages. (e) Amplitude of sliding Fourier transform of the resistance oscillations shown in (c) as a function of plunger gate voltage and plunger gate frequency. Adapted from [358]. Reproduced from [358], with permission from Springer Nature.

$\varphi_{\rm dyn} = 2\pi eV_{\rm DC}2L/(h\nu) = 4\pi eV_{\rm DC}/E_{\rm Th}$, where L is the length of edge propagation between the two QPCs, ν is the edge velocity, and $E_{\rm Th} = h\nu/L$ is the Thouless energy. Depending on the energy relaxation processes consecutive to the current flow, and on the electrostatic coupling between the cavity, the back gate, the source and the drain, the electrochemical potential in the cavity will adjust itself at a value intermediate between that of the source and that of the drain. The resulting conductance oscillations depending on the potential drop across the interferometer have been calculated in [358] by extending the theory of [372]. It reads

$$G = g_{\rm osc}\left[\beta\cos\left(2\pi\frac{\varphi}{\phi_0} - \frac{2L}{\hbar\nu}eV\beta\right)\right. \tag{49}$$

$$\left. + \overline{\beta}\cos\left(2\pi\frac{\varphi}{\phi_0} + \frac{2L}{\hbar\nu}eV\beta\right)\right], \tag{50}$$

where β and $\overline{\beta}$ are asymmetry parameters describing how symmetric is the voltage drop on the two side of the interferometer (see Supplementary Information in [358] for definition), and $g_{\rm osc} = \frac{e^2}{h}2\sqrt{R_1R_2}$ with R_1 and R_2 the reflection coefficients of each QPCs. Equation (49) reduces to $\Delta G \sim \cos(2\pi\phi/\phi_0 - 4\pi eV_{\rm DC}/E_{\rm Th})$ for a fully asymmetric potential drop across the interferometer and $\Delta G \sim \cos(2\pi\phi/\phi_0)\cos(2\pi eV_{\rm DC}/E_{\rm Th})$ for a fully symmetric potential drop. Figures 37(c) and (d) illustrates the resulting conductance oscillations as a function of plunger gate voltage and voltage bias for the asymmetric (small interferometer) and symmetric (large interferometer) cases, respectively. The edge velocity ν determined from the bias periodicity via $\nu = \Delta V_{\rm DC}L/h$, is found to be approximately 1.4×10^5 m s^{-1} (at 14 T). Another method to estimate the Thouless energy stems from the temperature dependence of the oscillation amplitude, described by $\exp(-T/T_0)$, as exemplified in figures 37(e)–(f) [358]. The fits of the Fourier peaks are used to estimate T_0 and the Thouless energy $E_{\rm Th} = 4\pi^2k_{\rm B}T_0L$. Figure 37(g) demonstrates the excellent agreement between the Thouless energies estimated using these two methods.

The interferometer geometry in [355] shown in figure 35(d), allows to study the phase coherence of interfering edges defined either by gating or by etching. Figure 38(a) shows plunger gate dependent oscillations of the inner channel at filling factor 2, where interfering channels undergo distinct potential confinements, as schematized on top of the figure. Figure 38(b) shows the edge channel positions (upper panel), interfering area (middle panel) and coherence length (lower panel) in these different configurations. In regime I ($1\ {\rm V} < V_{\rm pg} < 1.4\ {\rm V}$), oscillations' visibility remains relatively constant and the extracted interfering area corresponds to

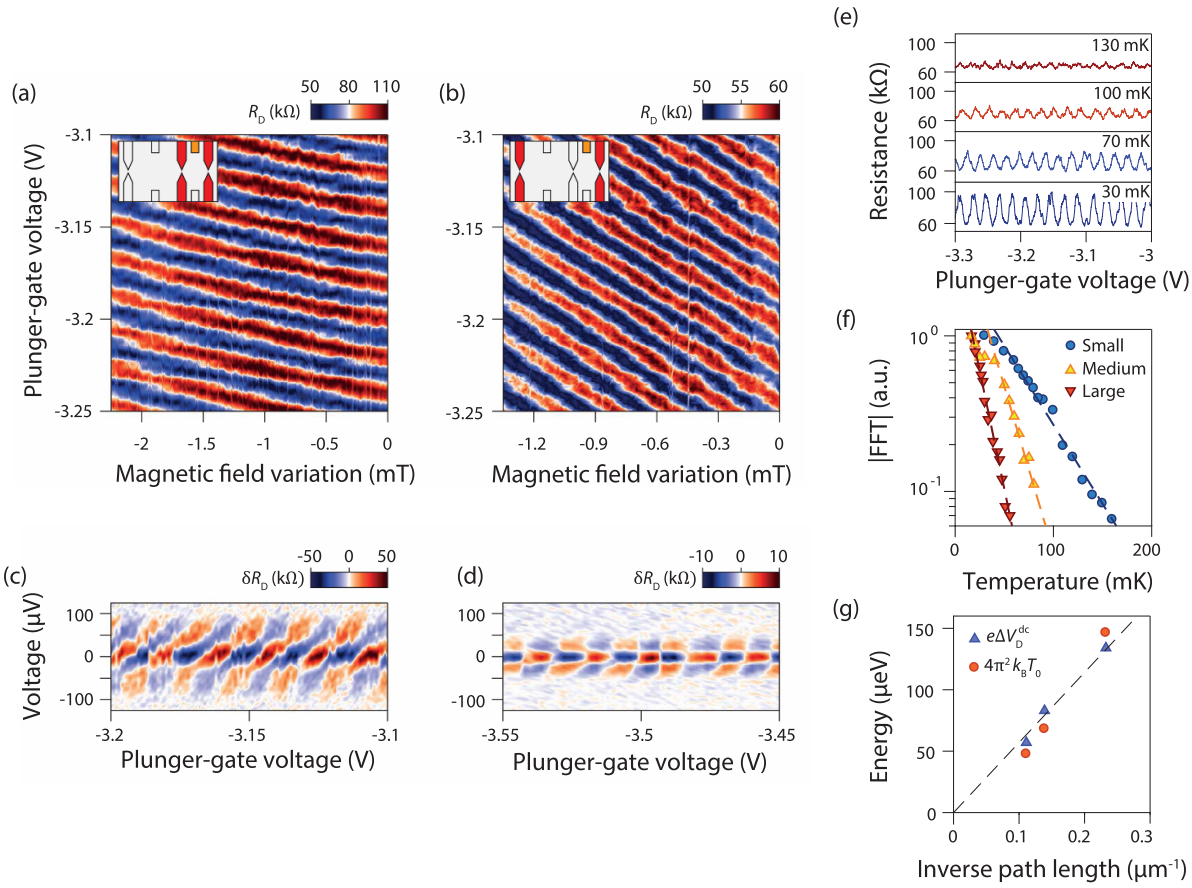

Figure 37. Resistance oscillations with magnetic field and plunger gate voltage. (a) in a 3 μm^2 interferometer and (b) in a 15 μm^2 interferometer (b). Checkerboard pattern obtained from the 3 μm^2 interferometer in (c) and from the 15 μm^2 interferometer in (d). (e) Resistance oscillations with plunger gate voltage at different temperatures. (f) Oscillation amplitudes extracted from a Fourier transform as a function of temperature for three interferometers ($A = 3.1$ μm^2, $A = 10.7$ μm^2 and $A = 14.7$ μm^2). (g) Energy scale extracted from the checkerboard patterns in (c) and (d) and the temperature dependence in (f) as a function of the inverse path length. Reproduced from [358], with permission from Springer Nature.

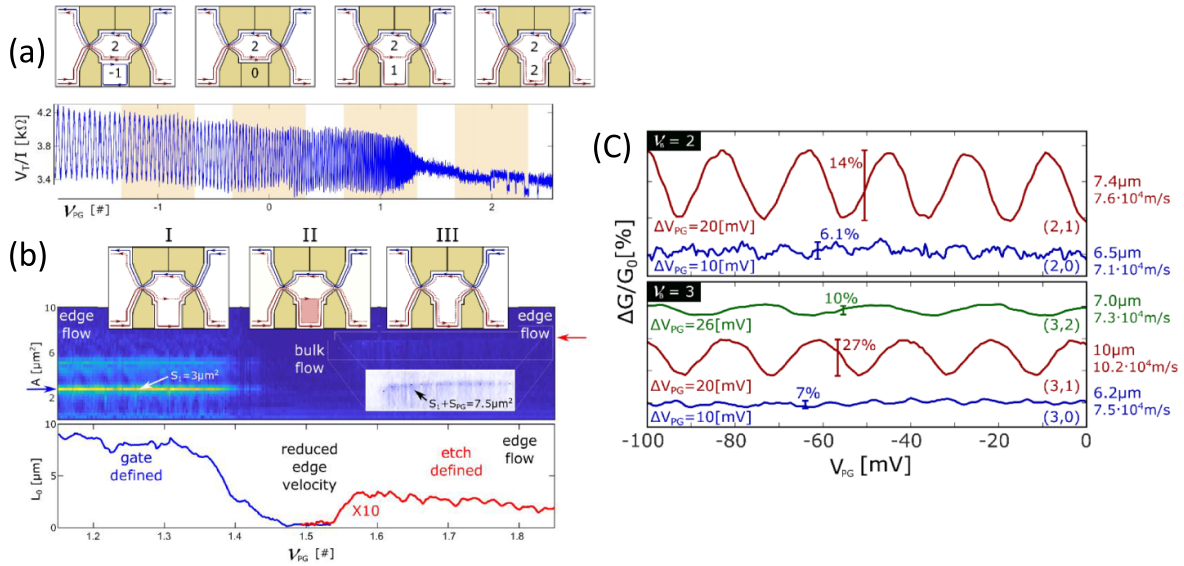

Figure 38. (a) Resistance oscillations with plunger gate voltages from −2 V to 3 V. (b) Interfering area extracted from oscillation periodicity in (a) from 1 V to 2 V (middle panel), top schematics indicate the quantum Hall edges path for each oscillation regime. Bottom panel is the phase coherence length extracted from the oscillations' visibility. (c) Oscillation visibility at bulk filling factor 2 (up) and 3 (bottom) for different edge channel interference. Reproduced from [355], with permission from Springer Nature.

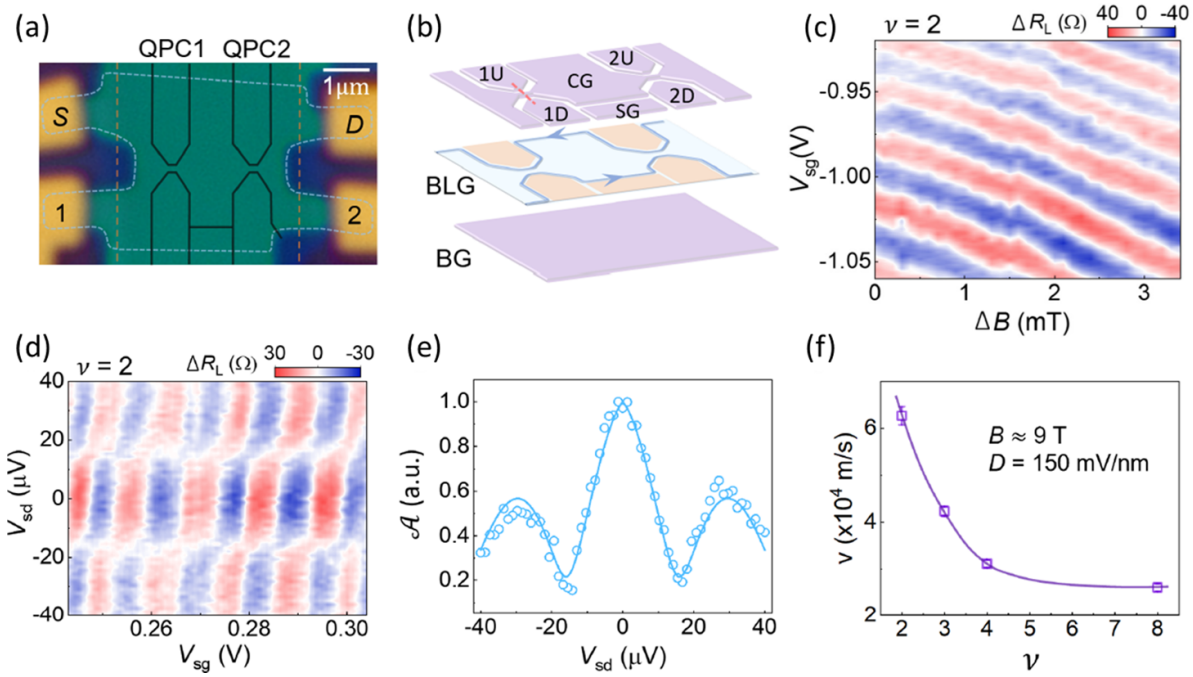

Figure 39. Bilayer graphene based Fabry-Pérot interferometer. (a) Optical image of the device. (b) Schematic of the device in an exploded view. (c) Resistance oscillations showing an Aharonov Bohm type pyjama at filling factor 2 for a field about 9 T. (d) The resistance oscillations as a function of side gate voltage and source drain voltage display a typical checkerboard pattern (B = 9 T, filling factor 2, 20 mK). (e) The oscillation amplitude at the oscillation frequency shows a lobe structure as a function of source drain voltage. The author extract both a Thouless energy and an edge velocity by fitting the lobe structure with the usual theory [355, 358] (f) Edge channel velocity (extracted from lobe structure as in (e) versus filling factor. The decrease in velocity for increasing filling factor can be understood in a non-interacting edge channel picture as the channels are further and further from the edge as the filling factor increase [198]. Reprinted with permission from [198]. Copyright (2023) American Chemical Society.

the inner channel traveling along the plunger gate. In regime III ($V_{pg} > 1.6$ V), the oscillations' visibility is dramatically reduced and the extracted area now includes the plunger gate delimited area, suggesting that both channels are propagating along the etched graphene edge. Note that the coherence lengths are about 7 μm for gate defined channels and 400 nm for etched defined channels. The detrimental effect on the coherence observed in etched-edge defined FPIs can be attributed to edge disorder and charge accumulation at the physical edge. Interestingly graphene crystal edges that have not undergone etching, as in the experiment conducted by Déprez and coworkers [358], led to a coherence length assessment of 10 μm, implying that pristine edges are equally good for coherence.

The authors of [355] systematically investigated the interference of various channels at filling factors 2 and 3. Figure 38(c) summarizes the plunger gate periodicity, oscillation visibility, edge velocity, and phase coherence length for these channels. The colors blue, red, and green are used to distinguish the innermost, middle, and outermost edges, respectively. The coherence lengths are of the order of tens of microns. The highest velocity and coherence length are obtained in the middle channel of $\nu_B = 3$ and are accounted for by interaction screening by adjacent edges.

6.6.3. Bilayer graphene based FPI. Bilayer graphene also hosts numerous fractional QH states, particularly those with even denominator fractions are believed to involve non-Abelian quasi-particles [373]. BLG is thus considered as a highly promising platform for performing non-Abelian braiding through interferometry. In the study reported by Fu and coworkers [198], the first Fabry-Pérot quantum Hall interferometer in bilayer graphene was introduced. In this investigation, bilayer graphene is encapsulated by h-BN flakes, with a global graphite gate at the bottom and several split gates on the top (see figures 39(a) and (b)). The devices operate in the Aharonov–Bohm regime as demonstrated in figure 39(c). The checkerboard pattern (figure 39(d)) is analysed through the same framework as in [355, 358], and the edge channel velocity is extracted from the lobe structure (figure 39(e)) at different filling factors (figure 39(f)). A careful analysis show that this velocity decreases as the distance of the edge channel to the edge increases, as expected. This work opens the door for further studies that might benefit from recent technical improvement, such as the use of air bridges [355] or atomic force microscopy etching [352].

In conclusion, the robust oscillations observed in single and bilayer graphene-based quantum Hall FPIs with various designs, characterized by strongly suppressed charging energy

and an extended phase coherence length, offer compelling reasons to advance and deepen these studies into fractional quantum Hall interferometry. Concurrently, some correlated phenomena in the integer quantum Hall regime remain to be understood. Very recent experiments have presented evidence for electron pairing at bulk filling factors $\nu \geqslant 2$ [374, 375], reproducing the phenomenology of GaAs FPIs [370, 376], and even tripling of electrons at $\nu = 3$ [375]. These phenomena are characterized by an anomalous Aharonov–Bohm flux period of $h/2e$ and $h/3e$, respectively. Interpretations suggest that these intriguing phenomena result from attracting pairing emerging via the exchange of neutral modes [377], or from inter-edge states charging effects [374]. They underscore the genuinely complex nature of these FPI devices, challenging initial expectations based on an apparently simple, non-interacting theory [372]. Exploring the physics of anyons in the fractional quantum Hall regime will undoubtedly require careful and systematic experiments, but the highly versatile graphene platform may bring advantages that may be pivotal for nailing down anyon interferometry.

7. Conclusion and perspectives

We have seen throughout this review that graphene has emerged as an excellent and unique platform for the realization of electron optical devices. This stems, among other things, from the ultra-high mobility of graphene structures and the ability of forming gapless p-n interfaces, where the doping changes continuously from electron to hole doping. This allowed, as detailed before, observing magnetic focusing and snake states and realizing interferometers based on quantum-Hall edge channels. The presence of the lattice and valley degree of freedom (or the layer in case of bilayer graphene) leads to a richer and much more fascinating behaviour than in conventional 2DEGs. Moreoever, due to the semimetallic nature of graphene, it can be contacted with ferromagnetic and superconducting electrodes. This yields ballistic spintronic devices that can show chiral properties, on the one hand, and ballistic interferometers that are governed by unconventional Andreev physics at p-n interfaces, on the other hand. The ability to combine graphene with other 2D materials and to stack different materials together with arbitrary twist angles opens a large parameter space, allowing to tailor the bandstructure and to design materials with yet unknown phenomenology. Correspondingly, these developments, including emergent phenomena such as unconventional superconductivity, also open up new challenges to theory. Properties, like superconducting pairing, spin-orbit interaction and magnetic exchange can also be introduced in monolayer and bilayer graphene through proximity to TMDCs or van der Waals superconductors and ferromagnets. This is a largely unexplored area where the combination with ballistic carriers opens up a new playground for quantum electron optics.

The outlook for graphene-based quantum devices is marked by intriguing possibilities and technological challenges. Research endeavors are directed towards achieving metrologically precise single electron pumps in graphene, aiming to match or even surpass the precision observed in traditional materials like GaAs [33, 378] and Silicon [379]. Additionally, the exploration of single electron transport utilizing surface acoustic waves in graphene presents a novel avenue, leveraging the unique properties of both the material and wave-based manipulation. Investigating the potential for Coulomb-induced anti-bunching [380–382] with single electrons in graphene, coupled with single-shot detection, stands as a challenging yet transformative goal with implications for quantum information processing. Furthermore, the pursuit of flying electron qubits in non-chiral geometry [383] opens up innovative pathways for quantum computing, capitalizing on graphene's exceptional electronic structure. The overall trajectory suggests a dynamic field with prospects for groundbreaking advancements, necessitating interdisciplinary collaboration at the intersection of materials science, quantum physics, and engineering to unlock the full potential of graphene in quantum technologies.

Data availability statement

The data cannot be made publicly available upon publication because they are owned by a third party and the terms of use prevent public distribution. The data that support the findings of this study are available upon reasonable request from the authors.

Acknowledgments

This common work was supported by various funding organizations.

P M acknowledges support from the Multi-Spin and 2DSOTECH FlagERA networks, the Twistrain ERC grant. This research was supported by the Ministry of Culture and Innovation and the National Research, Development and Innovation Office within the Quantum Information National Laboratory of Hungary (Grant No. 2022-2.1.1-NL-2022-00004).

M-H L acknowledges National Science and Technology Council (NSTC) of Taiwan (Grant Number NSTC 112-2112-M-006-019-MY3) for financial support. He further received funding through the *2023 International Presidential Visiting Scholarship* of University of Regensburg.

K R acknowledges support from the Deutsche Forschungsgemeinschaft (DFG, German Research Foundation) within Project-ID 314695032—SFB 1277 (Project A07).

A K acknowledges support from the Deutsche Forschungsgemeinschaft (DFG, German Research Foundation) within DFG Individual grant KN 1383/4, Project-ID 529637137.

C S acknowledges support from the European Research Council (ERC) under the European Union's Horizon 2020 research and innovation program: Grant Agreement No. 787414, ERC-Adv TopSupra, the Swiss NCCR Quantum Science and Technology (QSIT), the Swiss Nanoscience Institute (SNI) and the University of Basel.

F D P acknowledges support from the ERC (ERC-2018-STG QUAHQ), the 'Investissements d'Avenir' LabEx PALM (ANR-10-LABX-0039-PALM), and the Major Interest Domain (DIM) SIRTEQ and QUANTIP funded by the Ile-de-France Region.

C G acknowledges support from the Agence Nationale de la Recherche (ANR, French National Research Agency; project DADI), and thanks the STherQO members for pointing out certain relevant publications.

D P acknowledges support from a French government grant managed by the ANR agency under the 'France 2030 plan', with reference ANR-22-PETQ-0003. W Y acknowledges support the QuantERA II Program that has received funding from the European Union's Horizon 2020 research and innovation program under Grant Agreement No. 101017733.

P R and H C acknowledges support from the Agence Nationale de la Recherche (ANR, French National Research Agency; Project DADI).

ORCID iDs

Himadri Chakraborti https://orcid.org/0000-0001-8621-4007
Cosimo Gorini https://orcid.org/0000-0002-3197-8322
Angelika Knothe https://orcid.org/0000-0003-4488-5958
Ming-Hao Liu https://orcid.org/0000-0001-5602-4181
Péter Makk https://orcid.org/0000-0001-7637-4672
François D Parmentier https://orcid.org/0000-0001-9319-565X
David Perconte https://orcid.org/0000-0001-7480-8123
Klaus Richter https://orcid.org/0000-0001-7296-4237
Preden Roulleau https://orcid.org/0000-0002-8397-5019
Benjamin Sacépé https://orcid.org/0000-0001-5943-9999
Christian Schönenberger https://orcid.org/0000-0002-5652-460X

References

[1] Novoselov K S, Geim A K, Morozov S V, Jiang D, Zhang Y, Dubonos S V, Grigorieva I V and Firsov A A 2004 Electric field in atomically thin carbon films *Science* **306** 666–9
[2] Cao Y, Fatemi V, Fang S, Watanabe K, Taniguchi T, Kaxiras E and Jarillo-Herrero P 2018 Unconventional superconductivity in magic-angle graphene superlattices *Nature* **556** 43–50
[3] Hanbury Brown R and Twiss R Q 1954 A new type of interferometer for use in radio astronomy *Phil. Mag.* **45** 663–82
[4] Hanbury Brown R and Twiss R Q 1956 Correlation between photons in two coherent beams of light *Nature* **177** 27–29
[5] Huard B, Sulpizio J, Stander N, Todd K, Yang B and Goldhaber-Gordon D 2007 Transport measurements across a tunable potential barrier in graphene *Phys. Rev. Lett.* **98** 236803
[6] Lemme M C, Echtermeyer T J, Baus M and Kurz H 2007 A graphene field-effect device *IEEE Electron Device Lett.* **28** 282–4
[7] Williams J, DiCarlo L and Marcus C 2007 Quantum hall effect in a gate-controlled pn junction of graphene *Science* **317** 638–41
[8] Abanin D and Levitov L 2007 Quantized transport in graphene pn junctions in a magnetic field *Science* **317** 641–3
[9] Katsnelson M I, Novoselov K S and Geim A K 2006 Chiral tunnelling and the Klein paradox in graphene *Nat. Phys.* **2** 620–5
[10] Cheianov V V, Fal'ko V and Altshuler B L 2007 The focusing of electron flow and a veselago lens in graphene p-n junctions *Science* **315** 1252–5
[11] Cheianov V V and Fal'ko V I 2006 Selective transmission of Dirac electrons and ballistic magnetoresistance of np junctions in graphene *Phys. Rev.* B **74** 041403
[12] Silvestrov P and Efetov K 2007 Quantum dots in graphene *Phys. Rev. Lett.* **98** 016802
[13] Dingle R, Störmer H L, Gossard A C and Wiegmann W 1978 Electron mobilities in modulation-doped semiconductor heterojunction superlattices *Appl. Phys. Lett.* **33** 665–7
[14] Ketterson A, Ponse F, Henderson T, Klem J and Morkoç H 1985 Extremely low contact resistances for AlGaAs/GaAs modulation-doped field-effect transistor structures *J. Appl. Phys.* **57** 2305–7
[15] Chung Y J, Gupta A, Baldwin K W West K W , Shayegan M and Pfeiffer L N 2022 Understanding limits to mobility in ultrahigh-mobility gaas two-dimensional electron systems: 100 million cm^2/vs and beyond *Phys. Rev.* B **106** 075134
[16] van Wees B J, van Houten H, Beenakker C W J, Williamson J G, Kouwenhoven L P, van der Marel D and Foxon C T 1988 Quantized conductance of point contacts in a two-dimensional electron gas *Phys. Rev. Lett.* **60** 848–50
[17] Bolotin K I, Sikes K J, Jiang Z, Klima M, Fudenberg G, Hone J, Kim P and Stormer H L 2008 Ultrahigh electron mobility in suspended graphene *Solid State Commun.* **146** 351–5
[18] Du X, Skachko I, Barker A and Andrei E Y 2008 Approaching ballistic transport in suspended graphene *Nat. Nanotechnol.* **3** 491–5
[19] Dean C R *et al* 2010 Boron nitride substrates for high-quality graphene electronics *Nat. Nanotechnol.* **5** 722–6
[20] Wang L, Chen Z, Dean C R, Taniguchi T, Watanabe K, Brus L E and Hone J 2012 Negligible environmental sensitivity of graphene in a hexagonal boron nitride/graphene/h-bn sandwich structure *ACS Nano* **6** 9314–9
[21] Wang L *et al* 2013 One-dimensional electrical contact to a two-dimensional material *Science* **342** 614–7
[22] Young A F and Kim P 2009 Quantum interference and Klein tunnelling in graphene heterojunctions *Nat. Phys.* **5** 222–6
[23] Rickhaus P, Maurand R, Liu M-H, Weiss M, Richter K and Schönenberger C 2013 Ballistic interferences in suspended graphene *Nat. Commun.* **4** 2342
[24] Banszerus L, Schmitz M, Engels S, Goldsche M, Watanabe K, Taniguchi T, Beschoten B and Stampfer C 2016 Ballistic Transport Exceeding 28 μm in CVD Grown Graphene *Nano Lett.* **16** 1387–91
[25] Shytov A V, Rudner M S and Levitov L S 2008 Klein backscattering and Fabry-Pérot interference in graphene heterojunctions *Phys. Rev. Lett.* **101** 156804
[26] Williams J R 2017 Electron optics with graphene p-n junctions *2D Materials: Properties and Devices* (Cambridge University Press) pp 141–58
[27] Rickhaus P Makk P, Liu M-H, Tóvári E, Weiss M, Maurand R, Richter K and Schönenberger C 2015 Snake trajectories in ultraclean graphene p-n junctions *Nat. Commun.* **6** 1–6
[28] Novoselov K S, Geim A K, Morozov S V, Jiang D, Katsnelson M I, Grigorieva I V, Dubonos S V and

Firsov A A 2005 Two-dimensional gas of massless Dirac fermions in graphene *Nature* **438** 197–200
[29] Zhang Y B, Tan Y W, Stormer H L and Kim P 2005 Experimental observation of the quantum Hall effect and Berry's phase in graphene *Nature* **438** 201–4
[30] Yacoby A, Heiblum M, Mahalu D and Shtrikman H 1995 Coherence and phase sensitive measurements in a quantum dot *Phys. Rev. Lett.* **74** 4047
[31] Zhang Y, McClure D T, Levenson-Falk E M, Marcus C M, Pfeiffer L N and West K W 2009 Distinct signatures for Coulomb blockade and Aharonov-Bohm interference in electronic Fabry-Perot interferometers *Phys. Rev.* B **79** 241304
[32] Ji Y Chung Y, Sprinzak D, Heiblum M, Mahalu D and Shtrikman H 2003 An electronic Mach–Zehnder interferometer *Nature* **422** 415–8
[33] Fève G, Mahe' A, Berroir J-M, Kontos T, Plaçais B, Glattli D C, Cavanna A, Etienne B and Jin Y 2007 An on-demand coherent single-electron source *Science* **316** 1169–72
[34] Dubois J, Jullien T, Portier F, Roche P, Cavanna A, Jin Y, Wegscheider W, Roulleau P and Glattli D C 2013 Minimal-excitation states for electron quantum optics using levitons *Nature* **502** 659–63
[35] Henny M, Oberholzer S, Strunk C, Heinzel T, Ensslin K, Holland M and Schönenberger C 1999 The fermionic Hanbury Brown and Twiss experiment *Science* **284** 296–8
[36] Oliver W D, Kim J, Liu R C and Yamamoto Y 1999 Hanbury Brown and Twiss-type experiment with electrons *Science* **284** 299–301
[37] Liu R, Odom B, Yamamoto Y and Tarucha S 1998 Quantum interference in electron collision *Nature* **391** 263–5
[38] Bocquillon E, Parmentier F D, Grenier C, Berroir J-M, Degiovanni P, Glattli D C, Plaçais B, Cavanna A, Jin Y and Fève G 2012 Electron quantum optics: Partitioning electrons one by one *Phys. Rev. Lett.* **108** 196803
[39] Bocquillon E, Freulon V, Berroir J-M, Degiovanni P, Plaçais B, Cavanna A, Jin Y and Fève G 2013 Coherence and indistinguishability of single electrons emitted by independent sources *Science* **339** 1054–7
[40] Nakamura J, Liang S, Gardner G C and Manfra M J 2020 Direct observation of anyonic braiding statistics *Nat. Phys.* **16** 931–6
[41] Bartolomei H *et al* 2020 Fractional statistics in anyon collisions *Science* **368** 173–7
[42] Nayak C, Simon S H, Stern A, Freedman M and Das Sarma S 2008 Non-Abelian anyons and topological quantum computation *Rev. Mod. Phys.* **80** 1083–159
[43] Bäuerle C, Glattli D C, Meunier T, Portier F, Roche P Roulleau P, Takada S and Waintal X 2018 Coherent control of single electrons: a review of current progress *Rep. Prog. Phys.* **81** 056503
[44] Goerbig M O 2011 Electronic properties of graphene in a strong magnetic field *Rev. Mod. Phys.* **83** 1193–243
[45] Young A F, Dean C R, Wang L, Ren H, Cadden-Zimansky P, Watanabe K, Taniguchi T, Hone J, Shepard K L and Kim P 2012 Spin and valley quantum Hall ferromagnetism in graphene *Nat. Phys.* **8** 550–6
[46] Kharitonov M 2012 Phase diagram for the $\nu = 0$ quantum hall state in monolayer graphene *Phys. Rev.* B **85** 155439
[47] Kharitonov M 2012 Canted antiferromagnetic phase of the ν=0 quantum hall state in bilayer graphene *Phys. Rev. Lett.* **109** 046803
[48] Knothe A and Jolicoeur T 2016 Phase diagram of a graphene bilayer in the zero-energy landau level *Phys. Rev.* B **94** 235149
[49] Allen M T, Martin J and Yacoby A 2012 Gate-defined quantum confinement in suspended bilayer graphene *Nat. Commun.* **3** 934
[50] Dröscher S, Barraud C, Watanabe K, Taniguchi T, Ihn T and Ensslin K 2012 Electron flow in split-gated bilayer graphene *New J. Phys.* **14** 103007
[51] Goossens A S M, Driessen S C M, Baart T A, Watanabe K, Taniguchi T and Vandersypen L M K 2012 Gate-defined confinement in bilayer graphene-hexagonal boron nitride hybrid devices *Nano Lett.* **12** 4656–60
[52] Overweg H *et al* 2018 Electrostatically induced quantum point contacts in bilayer graphene *Nano Lett.* **18** 553–9
[53] Fong K C, Wollman E E, Ravi H, Chen W, Clerk A A, Shaw M D, Leduc H G and Schwab K C 2013 Measurement of the electronic thermal conductance channels and heat capacity of graphene at low temperature *Phys. Rev.* X **3** 041008
[54] Betz A C, Jhang S H, Pallecchi E, Ferreira R, Fève G, Berroir J-M and Plaçais B 2013 Supercollision cooling in undoped graphene *Nat. Phys.* **9** 109–12
[55] Fay A, Danneau R, Viljas J K, Wu F, Tomi M Y, Wengler J, Wiesner M and Hakonen P J 2011 Shot noise and conductivity at high bias in bilayer graphene: Signatures of electron-optical phonon coupling *Phys. Rev.* B **84** 245427
[56] Guinea F, Geim A K, Katsnelson M I and Novoselov K S 2010 Generating quantizing pseudomagnetic fields by bending graphene ribbons *Phys. Rev.* B **81** 035408
[57] Choi S-M, Jhi S-H and Son Y-W 2010 Effects of strain on electronic properties of graphene *Phys. Rev.* B **81** 081407
[58] Grassano D, D'Alessandro M, Pulci O, Sharapov S G, Gusynin V P and Varlamov A A 2020 Work function, deformation potential and collapse of landau levels in strained graphene and silicene *Phys. Rev.* B **101** 245115
[59] Wang L, Baumgartner A, Makk P, Zihlmann S, Varghese B S, Indolese D I, Watanabe K, Taniguchi T and Schönenberger C 2021 Global strain-induced scalar potential in graphene devices *Commun. Phys.* **4** 147
[60] Young A F, Sanchez-Yamagishi J D, Hunt B, Choi S H, Watanabe K, Taniguchi T, Ashoori R C and Jarillo-Herrero P 2014 Tunable symmetry breaking and helical edge transport in a graphene quantum spin Hall state *Nature* **505** 528–32
[61] Veyrat L, Jordan A, Zimmermann K, Gay F, Watanabe K, Taniguchi T, Sellier H and Sacépé B 2019 Low-magnetic-field regime of a gate-defined constriction in high-mobility graphene *Nano Lett.* **19** 635–42
[62] Knothe A and Jolicoeur T 2015 Edge structure of graphene monolayers in the $N = 0$ quantum Hall state *Phys. Rev.* B **92** 165110
[63] McCann E and Fal'ko V I 2006 Landau-level degeneracy and quantum Hall effect in a graphite bilayer *Phys. Rev. Lett.* **96** 086805
[64] McCann E, Abergel D S and Fal'ko V I 2007 The low energy electronic band structure of bilayer graphene *Eur. Phys. J. Spec. Top.* **148** 91–103
[65] McCann E and Koshino M 2013 The electronic properties of bilayer graphene *Rep. Prog. Phys.* **76** 056503
[66] Chang M-C and Niu Q 1995 Berry phase, hyperorbits and the Hofstadter spectrum *Phys. Rev. Lett.* **75** 1348–51
[67] Ashcroft N W and Mermin N D 1976 *Solid State Physics* (Holt, Rinehart and Winston)
[68] Liu M-H, Bundesmann J and Richter K 2012 Spin-dependent Klein tunneling in graphene: Role of Rashba spin-orbit coupling *Phys. Rev.* B **85** 085406
[69] Handschin C 2017 Quantum-Transport in Encapsulated Graphene P-N junctions *PhD Thesis* Department of Physics, University of Basel, Magna Cum Laude
[70] Klein O 1929 Die Reflexion von Elektronen an einem Potentialsprung nach der relativistischen Dynamik von Dirac *Z. Phys.* **53** 157–65
[71] Beenakker C W J 2008 Colloquium: Andreev reflection and Klein tunneling in graphene *Rev. Mod. Phys.* **80** 1337–54

[72] Castro Neto A H, Guinea F, Peres N M R, Novoselov K S and Geim A K 2009 The electronic properties of graphene *Rev. Mod. Phys.* **81** 109

[73] Allain P and Fuchs J 2011 Klein tunneling in graphene: optics with massless electrons *Eur. Phys. J.* B **83** 301–17

[74] Datta S 1995 *Electronic Transport in Mesoscopic Systems* (Cambridge University Press)

[75] Rickhaus P 2015 Electron Optics in Ballistic Graphene *PhD Thesis* Department of Physics, University of Basel

[76] Wimmer M 2008 Quantum transport in nanostructures: from computational concepts to spintronics in graphene and magnetic tunnel junctions *PhD Thesis* Universität Regensburg

[77] Lewenkopf C H and Mucciolo E R 2013 The recursive Green's function method for graphene *J. Comput. Electron.* **12** 203–31

[78] Luryi S 1988 Quantum capacitance devices *Appl. Phys. Lett.* **52** 501–3

[79] Fang T, Konar A, Xing H and Jena D 2007 Carrier statistics and quantum capacitance of graphene sheets and ribbons *Appl. Phys. Lett.* **91** 092109

[80] Dröscher S, Roulleau P, Molitor F, Studerus P, Stampfer C, Ensslin K and Ihn T 2010 Quantum capacitance and density of states of graphene *Appl. Phys. Lett.* **96** 152104

[81] Liu M-H 2013 Theory of carrier density in multigated doped graphene sheets with quantum correction *Phys. Rev.* B **87** 125427

[82] Multiphysics C 1998 Introduction to comsol multiphysics® *Comsol Multiphysics* vol 9 (*Burlington*) p 2018

[83] Logg A, Mardal K-A and Wells G N *et al* 2012 *Automated Solution of Differential Equations by the Finite Element Method* (Springer)

[84] The MathWorks, Inc. 2023 Partial Differential equation Toolbox™ User's Guide

[85] Mreńca-Kolasińska A, Rickhaus P, Zheng G, Richter K, Ihn T, Ensslin K and Liu M-H 2022 Quantum capacitive coupling between large-angle twisted graphene layers *2D Mater.* **9** 025013

[86] Liu M-H 2013 Gate-induced carrier density modulation in bulk graphene: theories and electrostatic simulation using Matlab pdetool *J. Comput. Electron.* **12** 188–202

[87] Liu M-H, Rickhaus P Makk P, Tóvári E, Maurand R, Tkatschenko F, Weiss M, Schönenberger C and Richter K 2015 Scalable tight-binding model for graphene *Phys. Rev. Lett.* **114** 036601

[88] Rickhaus P, Liu M-H, Makk P, Maurand R, Hess S Zihlmann S, Weiss M, Richter K and Schönenberger C 2015 Guiding of electrons in a few-mode ballistic graphene channel *Nano Lett.* **15** 5819–25

[89] Rickhaus P Makk P, Liu M-H, Richter K and Schönenberger C 2015 Gate tuneable beamsplitter in ballistic graphene *Appl. Phys. Lett.* **107** 251901

[90] Terres B *et al* 2016 Size quantization of dirac fermions in graphene constrictions *Nat. Commun.* **7** 11528

[91] Xiang S, Mreńca-Kolasińska A, Miseikis V, Guiducci S, Kolasiński K, Coletti C, Szafran B, Beltram F, Roddaro S and Heun S 2016 Interedge backscattering in buried split-gate-defined graphene quantum point contacts *Phys. Rev.* B **94** 155446

[92] Liu M-H, Gorini C and Richter K 2017 Creating and steering highly directional electron beams in graphene *Phys. Rev. Lett.* **118** 066801

[93] Bours L, Guiducci S, Mreńca-Kolasińska A, Szafran B, Maan J C and Heun S 2017 Manipulating quantum Hall edge channels in graphene through scanning gate microscopy *Phys. Rev.* B **96** 195423

[94] Kolasinski K, Mrenca-Kolasinska A and Szafran B 2017 Imaging snake orbits at graphene $n-p$ junctions *Phys. Rev.* B **95** 045304

[95] Makk P, Handschin C, Tóvári E, Watanabe K, Taniguchi T, Richter K, Liu M-H and Schönenberger C 2018 Coexistence of classical snake states and Aharonov-Bohm oscillations along graphene p n junctions *Phys. Rev.* B **98** 035413

[96] Ma Q, Parmentier F D, Roulleau P and Fleury G 2018 Graphene $n-p$ junctions in the quantum Hall regime: numerical study of incoherent scattering effects *Phys. Rev.* B **97** 205445

[97] Brun B, Moreau N, Somanchi S, Nguyen V-H, Watanabe K, Taniguchi T, Charlier J-C, Stampfer C and Hackens B 2019 Imaging dirac fermions flow through a circular veselago lens *Phys. Rev.* B **100** 041401

[98] Lane T L M, Knothe A and Fal'ko V I 2019 Semimetallic features in quantum transport through a gate-defined point contact in bilayer graphene *Phys. Rev.* B **100** 115427

[99] Kraft R, Liu M-H, Selvasundaram P B, Chen S-C, Krupke R, Richter K and Danneau R 2020 Anomalous cyclotron motion in graphene superlattice cavities *Phys. Rev. Lett.* **125** 217701

[100] Kang W-H, Chen S-C and Liu M-H 2020 Cloning of zero modes in one-dimensional graphene superlattices *Phys. Rev.* B **102** 195432

[101] Moreau N, Brun B, Somanchi S, Watanabe K, Taniguchi T, Stampfer C and Hackens B 2021 Upstream modes and antidots poison graphene quantum Hall effect *Nat. Commun.* **12** 1–7

[102] Moreau N, Brun B, Somanchi S, Watanabe K, Taniguchi T, Stampfer C and Hackens B 2021 Contacts and upstream modes explain the electron-hole asymmetry in the graphene quantum Hall regime *Phys. Rev.* B **104** L201406

[103] Schrepfer J-K, Chen S-C, Liu M-H, Richter K and Hentschel M 2021 Dirac fermion optics and directed emission from single- and bilayer graphene cavities *Phys. Rev.* B **104** 155436

[104] Brun B, Nguyen V-H, Moreau N, Somanchi S, Watanabe K, Taniguchi T, Charlier J-C, Stampfer C and Hackens B 2022 Graphene whisperitronics: transducing whispering gallery modes into electronic transport *Nano Lett.* **22** 128–34

[105] Chiu S-B, Mreńca-Kolasińska A, Lei K L, Chiu C-H, Kang W-H, Chen S-C and Liu M-H 2022 Manipulating electron waves in graphene using carbon nanotube gating *Phys. Rev.* B **105** 195416

[106] Zhumagulov Y, Frank T and Fabian J 2022 Edge states in proximitized graphene ribbons and flakes in a perpendicular magnetic field: emergence of lone pseudohelical pairs and pure spin-current states *Phys. Rev.* B **105** 205134

[107] Rao Q, Kang W-H, Xue H, Ye Z, Feng X, Watanabe K, Taniguchi T, Wang N, Liu M-H and Ki D-K 2023 Ballistic transport spectroscopy of spin-orbit-coupled bands in monolayer graphene on WSe_2 *Nat. Commun.* **14** 6124

[108] Du R, Liu M-H, Mohrmann J, Wu F, Krupke R, von Löhneysen H, Richter K and Danneau R 2018 Tuning anti-Klein to Klein tunnelingin bilayer graphene *Phys. Rev. Lett.* **121** 127706

[109] Liu M-H and Richter K 2012 Efficient quantum transport simulation for bulk graphene heterojunctions *Phys. Rev.* B **86** 115455

[110] Drienovsky M, Schrettenbrunner F-X, Sandner A, Weiss D, Eroms J, Liu M-H, Tkatschenko F and Richter K 2014 Towards superlattices: Lateral bipolar multibarriers in graphene *Phys. Rev.* B **89** 115421

[111] Varlet A, Liu M-H, Krueckl V, Bischoff D, Simonet P, Watanabe K, Taniguchi T, Richter K Ensslin K and Ihn T 2014 Fabry-Pérot interference in gapped bilayer graphene

with broken anti-Klein tunneling *Phys. Rev. Lett.* **113** 116601
[112] Rickhaus P *et al* 2020 The electronic thickness of graphene *Sci. Adv.* **6** eaay8409
[113] Mayorov A S *et al* 2011 Micrometer-scale ballistic transport in encapsulated graphene at room temperature *Nano Lett.* **11** 2396–9
[114] Taychatanapat T, Watanabe K, Taniguchi T and Jarillo-Herrero P 2013 Electrically tunable transverse magnetic focusing in graphene *Nat. Phys.* **9** 225–9
[115] Bhandari S, Lee G-H, Klales A, Watanabe K, Taniguchi T, Heller E, Kim P and Westervelt R M 2016 Imaging cyclotron orbits of electrons in graphene *Nano Lett.* **16** 1690–4
[116] Lee M, Wallbank J R, Gallagher P, Watanabe K, Taniguchi T, Fal'ko V I and Goldhaber-Gordon D 2016 Ballistic miniband conduction in a graphene superlattice *Science* **353** 1526–9
[117] Chen J H, Jang C, Xiao S, Ishigami M and Fuhrer M S 2008 Intrinsic and extrinsic performance limits of graphene devices on SiO2 *Nat. Nanotechnol.* **3** 206–9
[118] Goossens A M, Calado V E, Barreiro A, Watanabe K, Taniguchi T and Vandersypen L M 2012 Mechanical cleaning of graphene *Appl. Phys. Lett.* **100** 73110
[119] Lindvall N, Kalabukhov A and Yurgens A 2012 Cleaning graphene using atomic force microscope *J. Appl. Phys.* **111** 064904
[120] Tombros N, Veligura A, Junesch J, Van Den Berg J J, Zomer P J, Wojtaszek M, Vera Marun I J, Jonkman H T and Van Wees B J 2011 Large yield production of high mobility freely suspended graphene electronic devices on a polydimethylglutarimide based organic polymer *J. Appl. Phys.* **109** 093702
[121] Maurand R, Rickhaus P Makk P, Hess S, Tóvári E, Handschin C, Weiss M and Schönenberger C 2014 Fabrication of ballistic suspended graphene with local-gating *Carbon* **79** 486–92
[122] Freitag F, Weiss M, Maurand R, Trbovic J and Schönenberger C 2012 Homogeneity of bilayer graphene *Solid State Commun.* **152** 2053–7
[123] Jung M, Rickhaus P, Zihlmann S, Eichler A, Makk P and Schönenberger C 2019 Ghz nanomechanical resonator in an ultraclean suspended graphene p-n junction *Nanoscale* **11** 4355–61
[124] Haigh S J, Gholinia A, Jalil R, Romani S, Britnell L, Elias D C, Novoselov K S, Ponomarenko L A, Geim A K and Gorbachev R 2012 Cross-sectional imaging of individual layers and buried interfaces of graphene-based heterostructures and superlattices *Nat. Mater.* **11** 764–7
[125] Zomer P J, Guimar aes M H, Brant J C, Tombros N and Van Wees B J 2014 Fast pick up technique for high quality heterostructures of bilayer graphene and hexagonal boron nitride *Appl. Phys. Lett.* **105** 013101
[126] Kretinin A V *et al* 2014 Electronic properties of graphene encapsulated with different two-dimensional atomic crystals *Nano Lett.* **14** 3270–6
[127] Pizzocchero F, Gammelgaard L, Jessen B S, Caridad J M, Wang L, Hone J, Bøggild P and Booth T J 2016 The hot pick-up technique for batch assembly of van der Waals heterostructures *Nat. Commun.* **7** 1–10
[128] Purdie D G, Pugno N M, Taniguchi T, Watanabe K, Ferrari A C and Lombardo A 2018 Cleaning interfaces in layered materials heterostructures *Nat. Commun.* **9** 1–12
[129] Castellanos-Gomez A, Duan X, Fei Z, Gutierrez H R, Huang Y, Huang X, Quereda J, Qian Q, Sutter E and Sutter P 2022 Van der waals heterostructures *Nat. Rev. Methods Primers* **2** 58
[130] Guarochico-Moreira V H *et al* 2022 Tunable spin injection in high-quality graphene with one-dimensional contacts *Nano Lett.* **22** 935–41
[131] Zibrov A A, Kometter C, Zhou H, Spanton E M, Taniguchi T, Watanabe K, Zaletel M P and Young A F 2017 Tunable interacting composite fermion phases in a half-filled bilayer-graphene Landau level *Nature* **549** 360–4
[132] Zeng Y, Li J I, Dietrich S A, Ghosh O M, Watanabe K, Taniguchi T, Hone J and Dean C R 2019 High-quality magnetotransport in graphene using the edge-free corbino geometry *Phys. Rev. Lett.* **122** 137701
[133] Polshyn H Zhou H, Spanton E M, Taniguchi T, Watanabe K and Young A F 2018 Quantitative transport measurements of fractional quantum Hall energy gaps in edgeless graphene devices *Phys. Rev. Lett.* **121** 226801
[134] Yankowitz M, Ma Q, Jarillo-Herrero P and LeRoy B J 2019 van der Waals heterostructures combining graphene and hexagonal boron nitride *Nat. Rev. Phys.* **1** 112–25
[135] Wang W *et al* 2023 Ultra-clean assembly of van der Waals heterostructures *Nat. Electron.* **6** 1–10
[136] Barrier J *et al* 2020 Long-range ballistic transport of Brown-Zak fermions in graphene superlattices *Nat. Commun.* **11** 1–7
[137] Nam Y, Ki D K, Soler-Delgado D and Morpurgo A F 2017 Electron-hole collision limited transport in charge-neutral bilayer graphene *Nat. Phys.* **13** 1207–14
[138] Zihlmann S 2018 Spin and charge relaxation in graphene *PhD Thesis* Department of Physics, University of Basel
[139] Coissard A *et al* 2022 Imaging tunable quantum Hall broken-symmetry orders in graphene *Nature* **605** 51–56
[140] Liu X, Wang Z, Watanabe K, Taniguchi T, Vafek O and Li J I 2021 Tuning electron correlation in magic-angle twisted bilayer graphene using Coulomb screening *Science* **371** 1261–5
[141] Kim M *et al* 2020 Control of electron-electron interaction in graphene by proximity screening *Nat. Commun.* **11** 1–6
[142] Stepanov P, Das I, Lu X, Fahimniya A, Watanabe K, Taniguchi T, Koppens F H, Lischner J, Levitov L and Efetov D K 2020 Untying the insulating and superconducting orders in magic-angle graphene *Nature* **583** 375–8
[143] Neumann C *et al* 2015 Raman spectroscopy as probe of nanometre-scale strain variations in graphene *Nat. Commun.* **6** 8429
[144] Kumaravadivel P *et al* 2019 Strong magnetophonon oscillations in extra-large graphene *Nat. Commun.* **10** 3334
[145] Ribeiro-Palau R, Chen S, Zeng Y, Watanabe K, Taniguchi T, Hone J and Dean C R 2019 High-Quality Electrostatically Defined Hall Bars in Monolayer Graphene *Nano Lett.* **19** 2583–7
[146] Calado V E, Zhu S E, Goswami S, Xu Q, Watanabe K, Taniguchi T, Janssen G C and Vandersypen L M 2014 Ballistic transport in graphene grown by chemical vapor deposition *Appl. Phys. Lett.* **104** 023103
[147] Petrone N, Dean C R, Meric I, van der Zande A M, Huang P Y, Wang L, Muller D, Shepard K L and Hone J 2012 Chemical vapor deposition-derived graphene with electrical performance of exfoliated graphene *Nano Lett.* **12** 2751–6
[148] De Fazio D *et al* 2019 High-mobility, wet-transferred graphene grown by chemical vapor deposition *ACS Nano* **13** 8926–35
[149] Pezzini S, Mišeikis V, Pace S, Rossella F, Watanabe K, Taniguchi T and Coletti C 2020 High-quality electrical transport using scalable cvd graphene *2D Mater.* **7** 041003
[150] Banszerus L, Schmitz M, Engels S, Dauber J, Oellers M, Haupt F, Watanabe K, Taniguchi T, Beschoten B and Stampfer C 2015 Ultrahigh-mobility graphene devices

from chemical vapor deposition on reusable copper *Sci. Adv.* **1** e1500222
[151] Aprojanz J, Power S R, Bampoulis P, Roche S, Jauho A-P, Zandvliet H J W, Zakharov A A and Tegenkamp C 2018 Ballistic tracks in graphene nanoribbons *Nat. Commun.* **9** 4426
[152] Baringhaus J *et al* 2014 Exceptional ballistic transport in epitaxial graphene nanoribbons *Nature* **506** 349–54
[153] Prudkovskiy V S *et al* 2022 An epitaxial graphene platform for zero-energy edge state nanoelectronics *Nat. Commun.* **13** 7814
[154] Morikawa S, Dou Z, Wang S W, Smith C G, Watanabe K, Taniguchi T, Masubuchi S, Machida T and Connolly M R 2015 Imaging ballistic carrier trajectories in graphene using scanning gate microscopy *Appl. Phys. Lett.* **107** 243102
[155] Bhandari S, Lee G H, Watanabe K, Taniguchi T, Kim P and Westervelt R M 2020 Imaging Andreev reflection in graphene *Nano Lett.* **20** 4890–4
[156] Ingla-Aynés J, Manesco A L R, Ghiasi T S, Volosheniuk S, Watanabe K, Taniguchi T and van der Zant H S 2023 Specular electron focusing between gate-defined quantum point contacts in bilayer graphene *Nano Lett.* **23** 5453–9
[157] Chen S *et al* 2016 Electron optics with p-n junctions in ballistic graphene *Science* **353** 1522–5
[158] Berdyugin A I *et al* 2020 Minibands in twisted bilayer graphene probed by magnetic focusing *Sci. Adv.* **6** eaay7838
[159] Komatsu K, Morita Y, Watanabe E, Tsuya D, Watanabe K, Taniguchi T and Moriyama S 2024 Observation of the quantum valley hall state in ballistic graphene superlattices *Sci. Adv.* **4** eaaq0194
[160] Graef H *et al* 2019 A corner reflector of graphene Dirac fermions as a phonon-scattering sensor *Nat. Commun.* **10** 1–9
[161] Wang K, Elahi M M, Wang L, Habib K M, Taniguchi T, Watanabe K, Hone J, Ghosh A W, Lee G H and Kim P 2019 Graphene transistor based on tunable Dirac fermion optics *Proc. Natl Acad. Sci. USA* **116** 6575–9
[162] Elahi M M, Masum Habib K M, Wang K, Lee G H, Kim P and Ghosh A W 2019 Impact of geometry and non-idealities on electron "optics" based graphene p-n junction devices *Appl. Phys. Lett.* **114** 013507
[163] Morikawa S, Wilmart Q, Masubuchi S, Watanabe K, Taniguchi T, Plaçais B and Machida T 2017 Dirac fermion reflector by ballistic graphene sawtooth-shaped npn junctions *Semicond. Sci. Technol.* **32** 045010
[164] Lee G H, Park G H and Lee H J 2015 Observation of negative refraction of Dirac fermions in graphene *Nat. Phys.* **11** 925–9
[165] Barnard A W, Hughes A, Sharpe A L, Watanabe K, Taniguchi T and Goldhaber-Gordon D 2017 Absorptive pinhole collimators for ballistic Dirac fermions in graphene *Nat. Commun.* **8** 1–6
[166] Liu G, Velasco Jr. J, Bao W and Lau C N 2008 Fabrication of graphene p-n-p junctions with contactless top gates *Appl. Phys. Lett.* **92** 203103
[167] Handschin C, Fülöp B, Makk P, Blanter S, Weiss M, Watanabe K, Taniguchi T, Csonka S and Schönenberger C 2015 Point contacts in encapsulated graphene *Appl. Phys. Lett.* **107** 183108
[168] Gold C, Knothe A, Kurzmann A, Garcia-Ruiz A, Watanabe K, Taniguchi T, Fal'ko V, Ensslin K and Ihn T 2021 Coherent jetting from a gate-defined channel in bilayer graphene *Phys. Rev. Lett.* **127** 046801
[169] Zhang X *et al* 2022 Gate-tunable Veselago interference in a bipolar graphene microcavity *Nat. Commun.* **13** 1–6
[170] Cserti J, Pályi A and Péterfalvi C 2007 Caustics due to a negative refractive index in circular graphene $p-n$ junctions *Phys. Rev. Lett.* **99** 246801
[171] Péterfalvi C, Pályi A and Cserti J 2009 Electron flow in circular $n-p$ junctions of bilayer graphene *Phys. Rev.* B **80** 075416
[172] Péterfalvi C, Pályi A, Rusznyák A, Koltai J and Cserti J 2010 Catastrophe optics of caustics in single and bilayer graphene: fine structure of caustics *Phys. Status Solidi* b **247** 2949–52
[173] Dominik B, Pauline S, Anastasia V, Overweg Hiske C, Marius E, Thomas I and Klaus E 2015 The importance of edges in reactive ion etched graphene nanodevices *Phys. Status Solidi Rapid Res. Lett.* **10** 68–74
[174] Bischoff D, Libisch F, Burgdörfer J, Ihn T and Ensslin K 2014 Characterizing wave functions in graphene nanodevices: electronic transport through ultrashort graphene constrictions on a boron nitride substrate *Phys. Rev.* B **90** 115405
[175] Ihn T *et al* 2010 Graphene single-electron transistors *Mater. Today* **13** 44–50
[176] Overweg H *et al* 2018 Topologically nontrivial valley states in bilayer graphene quantum point contacts *Phys. Rev. Lett.* **121** 257702
[177] Lee Y *et al* 2020 Tunable valley splitting due to topological orbital magnetic moment in bilayer graphene quantum point contacts *Phys. Rev. Lett.* **124** 126802
[178] Banszerus L *et al* 2020 Observation of the spin-orbit gap in bilayer graphene by one-dimensional ballistic transport *Phys. Rev. Lett.* **124** 177701
[179] Knothe A and Fal'ko V 2018 Influence of minivalleys and Berry curvature on electrostatically induced quantum wires in gapped bilayer graphene *Phys. Rev.* B **98** 155435
[180] Kraft R, Krainov I V, Gall V, Dmitriev A P, Krupke R, Gornyi I V and Danneau R 2018 Valley subband splitting in bilayer graphene quantum point contacts *Phys. Rev. Lett.* **121** 257703
[181] Eich M *et al* 2018 Spin and valley states in gate-defined bilayer graphene quantum dots *Phys. Rev.* X **8** 031023
[182] Eich M *et al* 2018 Coupled quantum dots in bilayer graphene *Nano Lett.* **18** 5042–8
[183] Banszerus L, Frohn B, Epping A, Neumaier D, Watanabe K, Taniguchi T and Stampfer C 2018 Gate-defined electron hole double dots in bilayer graphene *Nano Lett.* **18** 4785–90
[184] Möller S *et al* 2021 Probing two-electron multiplets in bilayer graphene quantum dots *Phys. Rev. Lett.* **127** 256802
[185] Tong C *et al* 2021 Tunable valley splitting and bipolar operation in graphene quantum dots *Nano Lett.* **21** 1068–73
[186] Tong C *et al* 2022 Pauli blockade of tunable two-electron spin and valley states in graphene quantum dots *Phys. Rev. Lett.* **128** 067702
[187] Knothe A and Fal'ko V 2020 Quartet states in two-electron quantum dots in bilayer graphene *Phys. Rev.* B **101** 235423
[188] Banszerus L *et al* 2020 Electron hole crossover in gate-controlled bilayer graphene quantum dots *Nano Lett.* **20** 7709–15
[189] Kurzmann A *et al* 2021 Kondo effect and spin–orbit coupling in graphene quantum dots *Nat. Commun.* **12** 6004
[190] Garreis R *et al* 2021 Shell filling and trigonal warping in graphene quantum dots *Phys. Rev. Lett.* **126** 147703
[191] Banszerus L, Hecker K, Möller S, Icking E, Watanabe K, Taniguchi T, Volk C and Stampfer C 2022 Spin relaxation in a single-electron graphene quantum dot *Nat. Commun.* **13** 3637
[192] Banszerus L, Möller S, Icking E, Watanabe K, Taniguchi T, Volk C and Stampfer C 2020 Single-electron double quantum dots in bilayer graphene *Nano Lett.* **20** 2005–11

[193] Banszerus L, Möller S, Steiner C, Icking E, Trellenkamp S, Lentz F, Watanabe K, Taniguchi T, Volk C and Stampfer C 2021 Spin-valley coupling in single-electron bilayer graphene quantum dots *Nat. Commun.* **12** 5250

[194] Knothe A, Glazman L I and Fal'ko V I 2022 Tunneling theory for a bilayer graphene quantum dot's single- and two-electron states *New J. Phys.* **24** 043003

[195] Banszerus L, Möller S, Hecker K, Icking E, Watanabe K, Taniguchi T Stampfer C 2023 Particle-hole symmetry protects spin-valley blockade in graphene quantum dots *Nature* **618** 1–6

[196] Mayer D and Knothe A 2023 Tuning-confined states and valley G-factors by quantum dot design in bilayer graphene *Phys. Status Solidi* b **260** 2300395

[197] Iwakiri S, de Vries F K, Portolés E, Zheng G, Taniguchi T, Watanabe K, Ihn T and Ensslin K 2022 Gate-defined electron interferometer in bilayer graphene *Nano Lett.* **22** 6292–7

[198] Fu H L, Huang K, Watanabe K, Taniguchi T, Kayyalha M and Zhu J 2023 Aharonov-bohm oscillations in bilayer graphene quantum hall edge state fabry-perot interferometers *Nano Lett.* **23** 718–25

[199] Mirzakhani M, Myoung N, Peeters F M and Park H C 2023 Electronic mach-zehnder interference in a bipolar hybrid monolayer-bilayer graphene junction *Carbon* **201** 734–44

[200] Ingla-Aynés J, Manesco A L R, Ghiasi T S, Watanabe K, Taniguchi T and van der Zant H S J 2023 A ballistic electron source with magnetically-controlled valley polarization in bilayer graphene (arXiv:2310.15293)

[201] Seemann L, Knothe A and Hentschel M 2023 Gate-tunable regular and chaotic electron dynamics in ballistic bilayer graphene cavities *Phys. Rev.* B **107** 205404

[202] Péterfalvi C G, Oroszlány L, Lambert C J and Cserti J 2012 Intraband electron focusing in bilayer graphene *New J. Phys.* **14** 063028

[203] Xu S *et al* 2021 Tunable van Hove singularities and correlated states in twisted monolayer– bilayer graphene *Nat. Phys.* **17** 619–26

[204] Huber R, Liu M-H, Chen S-C, Drienovsky M, Sandner A, Watanabe K, Taniguchi T, Richter K, Weiss D and Eroms J 2020 Band conductivity oscillations in a gate-tunable graphene superlattice *Nano Lett.* **20** 8046–52

[205] Huber R, Steffen M-N, Drienovsky M, Sandner A, Watanabe K, Taniguchi T, Pfannkuche D, Weiss D and Eroms J 2022 Band conductivity oscillations in a gate-tunable graphene superlattice *Nat. Commun.* **13** 2856

[206] Drienovsky M, Joachimsmeyer J, Sandner A, Liu M-H, Taniguchi T, Watanabe K, Richter K, Weiss D and Eroms J 2018 Commensurability oscillations in one-dimensional graphene superlattices *Phys. Rev. Lett.* **121** 026806

[207] Mreńca-Kolasińska A, Chen S-C and Liu M-H 2023 Probing miniband structure and hofstadter butterfly in gated graphene superlattices via magnetotransport *npj 2D Mater. Appl.* **7** 64

[208] Moulsdale C, Knothe A and Fal'ko V 2020 Engineering of the topological magnetic moment of electrons in bilayer graphene using strain and electrical bias *Phys. Rev.* B **101** 085118

[209] Varlet A, Mucha-Kruczyński M, Bischoff D, Simonet P, Taniguchi T, Watanabe K, Fal'ko V, Ihn T and Ensslin K 2015 Tunable Fermi surface topology and Lifshitz transition in bilayer graphene *Synth. Met.* **210** 19–31

[210] Zhao Y, Wyrick J, Natterer F D, Rodriguez-Nieva J F, Lewandowski C, Watanabe K, Taniguchi T, Levitov L S, Zhitenev N B and Stroscio J A 2015 Creating and probing electron whispering-gallery modes in graphene *Science* **348** 672–5

[211] Ge Z *et al* 2021 Imaging quantum interference in stadium-shaped monolayer and bilayer graphene quantum dots *Nano Lett.* **21** 8993–8

[212] Rodriguez-Nieva J F and Levitov L S 2016 Berry phase jumps and giant nonreciprocity in dirac quantum dots *Phys. Rev.* B **94** 235406

[213] Wurm J, Rycerz A, Adagideli I, Wimmer M, Richter K and Baranger H U 2009 Symmetry classes in graphene quantum dots: universal spectral statistics, weak localization and conductance fluctuations *Phys. Rev. Lett.* **102** 056806

[214] Bardarson J H, Titov M and Brouwer P W 2009 Electrostatic confinement of electrons in an integrable graphene quantum dot *Phys. Rev. Lett.* **102** 226803

[215] Wurm J, Wimmer M, Baranger H U and Richter K 2010 Graphene rings in magnetic fields: Aharonov-Bohm effect and valley splitting *Semicond. Sci. Technol.* **25** MAR 4

[216] Schneider M and Brouwer P W 2011 Resonant scattering in graphene with a gate-defined chaotic quantum dot *Phys. Rev.* B **84** 115440

[217] Heinl J, Schneider M and Brouwer P W 2013 Interplay of Aharonov-Bohm and Berry phases in gate-defined graphene quantum dots *Phys. Rev.* B **87** 245426

[218] Schneider M and Brouwer P W 2014 Density of states as a probe of electrostatic confinement in graphene *Phys. Rev.* B **89** 205437

[219] Wurm J, Richter K and Adagideli i d I 2011 Edge effects in graphene nanostructures: from multiple reflection expansion to density of states *Phys. Rev.* B **84** 075468

[220] Wurm J, Richter K and Adagideli I 2011 Edge effects in graphene nanostructures: semiclassical theory of spectral fluctuations and quantum transport *Phys. Rev.* B **84** 205421

[221] Xu H-Y, Wang G-L, Huang L and Lai Y-C 2018 Chaos in Dirac electron optics: emergence of a relativistic quantum chimera *Phys. Rev. Lett.* **120** 124101

[222] Bercioux D, Frustaglia D and Martino A D 2023 Chiral spin channels in curved graphene *pn* junctions *Phys. Rev.* B **108** 115140

[223] Nöckel J U and Stone A D 1997 Ray and wave chaos in asymmetric resonant optical cavities *Nature* **385** 45–47

[224] Hentschel M and Richter K 2002 Quantum chaos in optical systems: the annular billiard *Phys. Rev.* E **66** 056207

[225] Wiersig J and Hentschel M 2008 Combining directional light output and ultralow loss in deformed microdisks *Phys. Rev. Lett.* **100** 033901

[226] Han C-D, Wang C-Z, Xu H-Y, Huang D and Lai Y-C 2018 Decay of semiclassical massless Dirac fermions from integrable and chaotic cavities *Phys. Rev.* B **98** 104308

[227] Varlet A, Liu M-H, Bischoff D, Simonet P, Taniguchi T, Watanabe K, Richter K, Ihn T and Ensslin K 2016 Band gap and broken chirality in single-layer and bilayer graphene *Phys. Statis Solidi Rapid Res. Lett.* **10** 46–57

[228] Elahi M M, Zeng Y, Dean C R and Ghosh A W 2024 Direct evidence of Klein-antiKlein tunneling of graphitic electrons in a Corbino geometry *Phys. Rev. Lett.* **132** 146302

[229] Handschin C, Makk P Rickhaus P , Liu M-H, Watanabe K, Taniguchi T, Richter K and Schönenberger C 2017 Fabry-Perot resonances in a graphene/hbn moire superlattice *Nano Lett.* **17** 328–33

[230] Thompson R J, Rempe G, Kimble H J and Lalezari R 1991 Measurement of ultralow losses in an optical interferometer *Optical Society of America Annual Meeting* (Optica Publishing Group) p WN4

[231] Divari P and Kliros G 2010 Modeling the thermopower of ballistic graphene ribbons *Physica* E **42** 2431–5

[232] Campos L C, Young A F, Surakitbovorn K Watanabe K , Taniguchi T and Jarillo-Herrero P 2012 Quantum and classical confinement of resonant states in a trilayer

graphene Fabry-Perot interferometer *Nat. Commun.* **3** 1239
[233] Oksanen M, Uppstu A Laitinen A, Cox D J, Craciun M F, Russo S, Harju A and Hakonen P 2014 Single-mode and multimode Fabry-Pérot interference in suspended graphene *Phys. Rev.* B **89** 121414
[234] Calado V E, Goswami S, Nanda G, Diez M, Akhmerov A R, Watanabe K, Taniguchi T, Klapwijk T M and Vandersypen L M K 2015 Ballistic josephson junctions in edge-contacted graphene *Nat. Nanotechnol.* **10** 761
[235] Taychatanapat T, Tan J Y, Yeo Y, Watanabe K, Taniguchi T and Oezyilmaz B 2015 Conductance oscillations induced by ballistic snake states in a graphene heterojunction *Nat. Commun.* **6** 6093
[236] Ben Shalom M *et al* 2016 Quantum oscillations of the critical current and high-field superconducting proximity in ballistic graphene *Nat. Phys.* **12** 318–22
[237] Allen M T *et al* 2017 Observation of electron coherence and Fabry-Perot standing waves at a graphene edge *Nano Lett.* **17** 7380–6
[238] Nanda G, Aguilera-Servin J L, Rakyta P, Kormanyos A, Kleiner R, Koelle D, Watanabe K, Taniguchi T, Vandersypen L M K and Goswami S 2017 Current-phase relation of ballistic graphene Josephson junctions *Nano Lett.* **17** 3396–401
[239] Zhu M, Ben Shalom M, Mishchsenko A, Fal'ko V I, Novoselov K and Geim A 2018 Supercurrent and multiple Andreev reflections in micrometer-long ballistic graphene josephson junctions *Nanoscale* **10** 3020–5
[240] Pandey P, Kraft R, Krupke R, Beckmann D and Danneau R 2019 Andreev reflection in ballistic normal metal/graphene/superconductor junctions *Phys. Rev.* B **100** 165416
[241] Jung M, Rickhaus P, Zihlmann S, Makk P and Schönenberger C 2016 Microwave photodetection in an ultraclean suspended bilayer graphene p-n junction *Nano Lett.* **16** 6988–93
[242] Rickhaus P *et al* 2019 Gap opening in twisted double bilayer graphene by crystal fields *Nano Lett.* **19** 8821–8
[243] Mueller M, Braeuninger M and Trauzettel B 2009 Temperature dependence of the conductivity of ballistic graphene *Phys. Rev. Lett.* **103** 196801
[244] Ideue T and Iwasa Y 2021 Symmetry breaking and nonlinear electric transport in van der waals nanostructures *Annu. Rev. Condens. Matter Phys.* **12** 201–23
[245] Huang L, Lai Y-C, Ferry D K, Akis R and Goodnick S M 2009 Transmission and scarring in graphene quantum dots *J. Phys.: Condens. Matter* **21** 344203
[246] Ghosh T K, De Martino A, Häusler W, Dell'Anna L and Egger R 2008 Conductance quantization and snake states in graphene magnetic waveguides *Phys. Rev.* B **77** 081404
[247] Oroszlány L, Rakyta P, Kormányos A, Lambert C J and Cserti J 2008 Theory of snake states in graphene *Phys. Rev.* B **77** 081403
[248] Milovanovic S P, Masir M R and Peeters F M 2014 Interplay between snake and quantum edge states in a graphene hall bar with a pn-junction *Appl. Phys. Lett.* **105** 123507
[249] Cohnitz L, De Martino A, Häusler W and Egger R 2016 Chiral interface states in graphene $p-n$ junctions *Phys. Rev.* B **94** 165443
[250] Bercioux D and De Martino A 2019 Spin-orbit interaction and snake states in a graphene p-n junction *Phys. Rev.* B **100** 115407
[251] LaGasse S W and Lee J U 2016 Theory of landau level mixing in heavily graded graphene $p-n$ junctions *Phys. Rev.* B **94** 165312
[252] LaGasse S W and Lee J U 2017 Understanding magnetic focusing in graphene $p-n$ junctions through quantum modeling *Phys. Rev.* B **95** 155433
[253] LaGasse S W and Cress C D 2020 Unveiling electron optics in two-dimensional materials by nonlocal resistance mapping *Nano Lett.* **20** 6623–9
[254] Sim H-S, Ahn K-H, Chang K J, Ihm G, Kim N and Lee S J 1998 Magnetic edge states in a magnetic quantum dot *Phys. Rev. Lett.* **80** 1501–4
[255] Nogaret A, Bending S J and Henini M 2000 Resistance resonance effects through magnetic edge states *Phys. Rev. Lett.* **84** 2231–4
[256] Reijniers J and Peeters F M 2000 Snake orbits and related magnetic edge states *J. Phys.: Condens. Matter* **12** 9771
[257] Reijniers J, Matulis A, Chang K, Peeters F M and Vasilopoulos P 2002 Confined magnetic guiding orbit states *Europhys. Lett.* **59** 749
[258] Halperin B I 1982 Quantized Hall conductance, current-carrying edge states and the existence of extended states in a two-dimensional disordered potential *Phys. Rev.* B **25** 2185–90
[259] MacDonald A H and Streda P 1984 Quantized Hall effect and edge currents *Phys. Rev.* B **29** 1616–9
[260] Kane B E, Tsui D C and Weimann G 1987 Evidence for edge currents in the integral quantum Hall effect *Phys. Rev. Lett.* **59** 1353–6
[261] Büttiker M 1988 Absence of backscattering in the quantum Hall effect in multiprobe conductors *Phys. Rev.* B **38** 9375–89
[262] Washburn S, Fowler A B, Schmid H and Kern D 1988 Quantized Hall effect in the presence of backscattering *Phys. Rev. Lett.* **61** 2801–4
[263] McDonald S W and Kaufman A N 1979 Spectrum and eigenfunctions for a hamiltonian with stochastic trajectories *Phys. Rev. Lett.* **42** 1189–91
[264] Davies N, Patel A A, Cortijo A, Cheianov V, Guinea F and Fal'ko V I 2012 Skipping and snake orbits of electrons: Singularities and catastrophes *Phys. Rev.* B **85** 155433
[265] Chen J-C, Xie X C and Sun Q-F 2012 Current oscillation of snake states in graphene *p-n* junction *Phys. Rev.* B **86** 035429
[266] Milovanovic S P, Masir M R and Peeters F M 2013 Spectroscopy of snake states using a graphene Hall bar *Appl. Phys. Lett.* **103** 233502
[267] Büttiker M 1992 The quantum hall effect in open conductors *Semiconductors and Semimetals* vol 35, ed M Reed (Elsevier) ch 4, pp 191–277
[268] Christen T and Büttiker M 1996 Low-frequency admittance of quantized Hall conductors *Phys. Rev.* B **53** 2064–72
[269] Sánchez D and Büttiker M 2004 Magnetic-field asymmetry of nonlinear mesoscopic transport *Phys. Rev. Lett.* **93** 106802
[270] Sánchez D and López R 2013 Scattering theory of nonlinear thermoelectric transport *Phys. Rev. Lett.* **110** 026804
[271] Gorini C, Weinmann D and Jalabert R A 2014 Scanning-gate-induced effects in nonlinear transport through nanostructures *Phys. Rev.* B **89** 115414
[272] Texier C and Mitscherling J 2018 Nonlinear conductance in weakly disordered mesoscopic wires: interaction and magnetic field asymmetry *Phys. Rev.* B **97** 075306
[273] Moskalets M and Büttiker M 2002 Floquet scattering theory of quantum pumps *Phys. Rev.* B **66** 205320
[274] Samuelsson P and Büttiker M 2005 Dynamic generation of orbital quasiparticle entanglement in mesoscopic conductors *Phys. Rev.* B **71** 245317
[275] Akkermans E and Montambaux G 2007 *Mesoscopic Physics of Electrons and Photons* (Cambridge University Press)
[276] Imry Y 2008 *Introduction to Mesoscopic Physics* (Oxford University Press)

[277] Samuelsson P, Sukhorukov E V and Büttiker M 2004 Two-particle Aharonov-Bohm effect and entanglement in the electronic Hanbury Brown–Twiss setup *Phys. Rev. Lett.* **92** 026805

[278] Chung V S-W, Samuelsson P and Büttiker M 2005 Visibility of current and shot noise in electrical Mach-Zehnder and Hanbury Brown Twiss interferometers *Phys. Rev.* B **72** 125320

[279] Beenakker C W J 1990 Edge channels for the fractional quantum Hall effect *Phys. Rev. Lett.* **64** 216–9

[280] Chang A 1990 A unified transport theory for the integral and fractional quantum Hall effects: phase boundaries, edge currents and transmission/reflection probabilities *Solid State Commun.* **74** 871–6

[281] Chklovskii D B, Shklovskii B I and Glazman L I 1992 Electrostatics of edge channels *Phys. Rev.* B **46** 4026–34

[282] Chklovskii D B, Matveev K A and Shklovskii B I 1993 Ballistic conductance of interacting electrons in the quantum Hall regime *Phys. Rev.* B **47** 12605

[283] Armagnat P and Waintal X 2020 Reconciling edge states with compressible stripes in a ballistic mesoscopic conductor *J. Phys. Mater.* **3** 02LT01

[284] Flór I M, Lacerda-Santos A, Fleury G, Roulleau P and Waintal X 2022 Positioning of edge states in a quantum Hall graphene p n junction *Phys. Rev.* B **105** L241409

[285] Chamon C d C and Wen X G 1994 Sharp and smooth boundaries of quantum Hall liquids *Phys. Rev.* B **49** 8227–41

[286] Paradiso N, Heun S Roddaro S, Sorba L, Beltram F, Biasiol G, Pfeiffer L N and West K W 2012 Imaging fractional incompressible stripes in integer quantum Hall systems *Phys. Rev. Lett.* **108** 246801

[287] Bhattacharyya R, Banerjee M Heiblum M, Mahalu D and Umansky V 2019 Melting of interference in the fractional quantum Hall effect: appearance of neutral modes *Phys. Rev. Lett.* **122** 246801

[288] Khanna U, Goldstein M and Gefen Y 2021 Fractional edge reconstruction in integer quantum Hall phases *Phys. Rev.* B **103** L121302

[289] Khanna U, Goldstein M and Gefen Y 2022 Emergence of neutral modes in Laughlin-like fractional quantum Hall phases *Phys. Rev. Lett.* **129** 146801

[290] Li G, Luican-Mayer A, Abanin D, Levitov L and Andrei E Y 2013 Evolution of Landau levels into edge states in graphene *Nat. Commun.* **4** 1744

[291] Coissard A, Grushin A G, Repellin C, Veyrat L, Watanabe K, Taniguchi T, Gay F, Courtois H Sellier H and Sacépé B 2023 Absence of edge reconstruction for quantum Hall edge channels in graphene devices *Sci. Adv.* **9** eadf7220

[292] Cui Y-T *et al* 2016 Unconventional correlation between quantum hall transport quantization and bulk state filling in gated graphene devices *Phys. Rev. Lett.* **117** 186601

[293] Seredinski A, Draelos A W, Arnault E G, Wei M-T, Li H, Fleming T, Watanabe K, Taniguchi T, Amet F and Finkelstein G 2019 Quantum hall–based superconducting interference device *Sci. Adv.* **5** eaaw8693

[294] Giuliani C and Vignale G 2005 *Quantum Theory of the Electron Liquid* (Cambridge University Press)

[295] Giamarchi T 2003 *Quantum Physics in One Dimension* (Oxford University Press)

[296] Haldane F D M 1981 Luttinger liquid theory of one-dimensional quantum fluids. I. Properties of the Luttinger model and their extension to the general 1d interacting spinless fermi gas *J. Phys. C: Solid State Phys.* **14** 2585

[297] von Delft J and Schoeller H 1998 Bosonization for beginners—refermionization for experts *Ann. Phys., Lpz.* **510** 225–305

[298] Imambekov A, Schmidt T L and Glazman L I 2012 One-dimensional quantum liquids: Beyond the Luttinger liquid paradigm *Rev. Mod. Phys.* **84** 1253–306

[299] Levchenko A and Micklitz T 2021 Kinetic processes in Fermi-Luttinger liquids *JETP* **132** 675

[300] Ferraro D, Roussel B, Cabart C, Thibierge E, Fève G, Grenier C and Degiovanni P 2014 Real-Time Decoherence of Landau and Levitov Quasiparticles in Quantum Hall Edge Channels *Phys. Rev. Lett.* **113** 166403

[301] Fujisawa T 2022 Nonequilibrium charge dynamics of Tomonaga-Luttinger liquids in quantum hall edge channels *Ann. Phys., Lpz.* **534** 2100354

[302] Förster H, Pilgram S and Büttiker M 2005 Decoherence and full counting statistics in a Mach-Zehnder interferometer *Phys. Rev.* B **72** 075301

[303] Marquardt F 2005 Fermionic Mach-Zehnder interferometer subject to a quantum bath *Europhys. Lett.* **72** 788

[304] Lunde A M, Nigg S E and Büttiker M 2010 Interaction-induced edge channel equilibration *Phys. Rev.* B **81** 041311

[305] Chalker J T, Gefen Y and Veillette M Y 2007 Decoherence and interactions in an electronic Mach-Zehnder interferometer *Phys. Rev.* B **76** 085320

[306] Feldman D E and Halperin B I 2022 Robustness of quantum Hall interferometry *Phys. Rev.* B **105** 165310

[307] Levkivskyi I P and Sukhorukov E V 2008 Dephasing in the electronic Mach-Zehnder interferometer at filling factor $\nu = 2$ *Phys. Rev.* B **78** 045322

[308] Neder I, Heiblum M, Levinson Y, Mahalu D and Umansky V 2023 Unexpected behavior in a two-path electron interferometer *Phys. Rev. Lett.* **9** 016804

[309] Roulleau P, Portier F, Glattli D, Roche P, Cavanna A, Faini G, Gennser U and Mailly D 2007 Finite bias visibility of the electronic Mach-Zehnder interferometer *Phys. Rev.* B **76** 161309

[310] Roulleau P, Portier F, Roche P, Cavanna A, Faini G, Gennser U and Mailly D 2008 Direct measurement of the coherence length of edge states in the integer quantum Hall regime *Phys. Rev. Lett.* **100** 126802

[311] Altimiras C, le Sueur H, Gennser U, Cavanna A, Mailly D and Pierre F 2010 Tuning energy relaxation along quantum hall channels *Phys. Rev. Lett.* **105** 226804

[312] le Sueur H, Altimiras C, Gennser U, Cavanna A, Mailly D and Pierre F 2010 Energy Relaxation in the Integer Quantum Hall Regime *Phys. Rev. Lett.* **105** 056803

[313] Zurek W H 2003 Decoherence, einselection and the quantum origins of the classical *Rev. Mod. Phys.* **75** 715–75

[314] Safi I and Saleur H 2004 One-channel conductor in an ohmic environment: Mapping to a Tomonaga-Luttinger liquid and full counting statistics *Phys. Rev. Lett.* **93** 126602

[315] Degiovanni P, Grenier C and Fève G 2009 Decoherence and relaxation of single-electron excitations in quantum Hall edge channels *Phys. Rev.* B **80** 241307

[316] Neuenhahn C and Marquardt F 2009 universal dephasing in a chiral 1d interacting fermion system *Phys. Rev. Lett.* **102** 046806

[317] Komiyama S, Hirai H, Sasa S and Hiyamizu S 1989 Violation of the integral quantum hall effect: influence of backscattering and the role of voltage contacts *Phys. Rev.* B **40** 12566–9

[318] Chirolli L, Taddei F, Fazio R and Giovannetti V 2013 Interactions in electronic Mach-Zehnder interferometers with copropagating edge channels *Phys. Rev. Lett.* **111** 036801

[319] Büttiker M 1986 Role of quantum coherence in series resistors *Phys. Rev.* B **33** 3020–6

[320] Jo M *et al* 2022 Scaling behavior of electron decoherence in a graphene Mach-Zehnder interferometer *Nat. Commun.* **13** 5473

[321] Morikawa S, Masubuchi S, Moriya R, Watanabe K, Taniguchi T and Machida T 2015 Edge-channel interferometer at the graphene quantum Hall pn junction *Appl. Phys. Lett.* **106** 183101

[322] Wei D S, van der Sar T, Sanchez-Yamagishi J D, Watanabe K, Taniguchi T, Jarillo-Herrero P, Halperin B I and Yacoby A 2017 Mach-Zehnder interferometry using spin- and valley-polarized quantum Hall edge states in graphene *Sci. Adv.* **3** e1700600

[323] Handschin C, Makk P Rickhaus P , Maurand R, Watanabe K, Taniguchi T, Richter K, Liu M-H and Schönenberger C 2017 Giant valley-isospin conductance oscillations in ballistic graphene *Nano Lett.* **17** 5389–93

[324] Jo M *et al* 2021 Quantum Hall valley splitters and a tunable Mach-Zehnder interferometer in graphene *Phys. Rev. Lett.* **126** 146803

[325] Tworzydło J, Snyman I, Akhmerov A R and Beenakker C W J 2007 Valley-isospin dependence of the quantum Hall effect in a graphene *p-n* junction *Phys. Rev.* B **76** 035411

[326] Trifunovic L and Brouwer P W 2019 Valley isospin of interface states in a graphene *pn* junction in the quantum Hall regime *Phys. Rev.* B **99** 205431

[327] Rehmann M K *et al* 2019 Characterization of hydrogen plasma defined graphene edges *Carbon* **150** 417–24

[328] Wei D S, van der Sar T, Lee S H, Watanabe K, Taniguchi T, Halperin B I and Yacoby A 2018 Electrical generation and detection of spin waves in a quantum Hall ferromagnet *Science* **362** 229–33

[329] Assouline A *et al* 2023 Emission and coherent control of levitons in graphene *Science* **382** 1260–4

[330] Seelig G and Büttiker M 2001 Charge-fluctuation-induced dephasing in a gated mesoscopic interferometer *Phys. Rev.* B **64** 245313

[331] Youn S-C, Lee H-W and Sim H-S 2008 Nonequilibrium dephasing in an electronic Mach-Zehnder interferometer *Phys. Rev. Lett.* **100** 196807

[332] Roulleau P, Portier F, Roche P, Cavanna A, Faini G, Gennser U and Mailly D 2008 Noise dephasing in edge states of the integer quantum Hall regime *Phys. Rev. Lett.* **101** 186803

[333] Bocquillon E, Freulon V, Berroir J-M, Degiovanni P, Plaçais B, Cavanna A, Jin Y and Fève G 2013 Separation of neutral and charge modes in one-dimensional chiral edge channels *Nat. Commun.* **4** 1839

[334] Sukhorukov E and Cheianov V 2007 Resonant Dephasing in the Electronic Mach-Zehnder Interferometer *Phys. Rev. Lett.* **99** 156801

[335] Litvin L V, Helzel A, Tranitz H-P, Wegscheider W and Strunk C 2008 Edge-channel interference controlled by Landau level filling *Phys. Rev.* B **78** 075303

[336] Altimiras C, le Sueur H, Gennser U, Cavanna A, Mailly D and Pierre F 2009 Non-equilibrium edge-channel spectroscopy in the integer quantum Hall regime *Nat. Phys.* **6** 34–39

[337] Degiovanni P, Grenier C, Fève G, Altimiras C, le Sueur H and Pierre F 2010 Plasmon scattering approach to energy exchange and high-frequency noise in $\nu = 2$ quantum Hall edge channels *Phys. Rev.* B **81** 121302

[338] Huynh P-A, Portier F, le Sueur H, Faini G, Gennser U, Mailly D, Pierre F, Wegscheider W and Roche P 2012 Quantum coherence engineering in the integer quantum hall regime *Phys. Rev. Lett.* **108** 256802

[339] Freulon V, Marguerite A, Berroir J-M, Plaçais B, Cavanna A, Jin Y and Fève G 2015 Hong-Ou-Mandel experiment for temporal investigation of single-electron fractionalization *Nat. Commun.* **6** 1–6

[340] Lunde A M and Nigg S E 2016 Statistical theory of relaxation of high-energy electrons in quantum Hall edge states *Phys. Rev.* B **94** 045409

[341] Marguerite A *et al* 2016 Decoherence and relaxation of a single electron in a one-dimensional conductor *Phys. Rev.* B **94** 115311

[342] Gurman I, Sabo R, Heiblum M, Umansky V and Mahalu D 2016 Dephasing of an electronic two-path interferometer *Phys. Rev.* B **93** 121412

[343] Tewari S, Roulleau P, Grenier C, Portier F, Cavanna A, Gennser U, Mailly D and Roche P 2016 Robust quantum coherence above the Fermi sea *Phys. Rev.* B **93** 035420

[344] Marguerite A, Bocquillon E, Berroir J-M, Plaçais B, Cavanna A, Jin Y, Degiovanni P and Fève G 2017 Two-particle interferometry in quantum Hall edge channels *Phys. Status Solidi* b **254** 1600618

[345] Itoh K, Nakazawa R, Ota T, Hashisaka M, Muraki K and Fujisawa T 2018 Signatures of a nonthermal metastable state in copropagating quantum hall edge channels *Phys. Rev. Lett.* **120** 197701

[346] Cabart C, Roussel B, Fève G and Degiovanni P 2018 Taming electronic decoherence in one-dimensional chiral ballistic quantum conductors *Phys. Rev.* B **98** 155302

[347] Duprez H, Sivre E, Anthore A Aassime A Cavanna A Ouerghi A, Gennser U and Pierre F 2019 Macroscopic electron quantum coherence in a solid-state circuit *Phys. Rev.* X **9** 021030

[348] Rodriguez R H, Parmentier F D, Ferraro D, Roulleau P, Gennser U, Cavanna A, Sassetti M, Portier F, Mailly D and Roche P 2020 Relaxation and revival of quasiparticles injected in an interacting quantum Hall liquid *Nat. Commun.* **11** 1–8

[349] Assouline A *et al* 2021 Excitonic nature of magnons in a quantum hall ferromagnet *Nat. Phys.* **17** 1369–74

[350] Nakaharai S, Williams J R and Marcus C M 2011 Gate-defined graphene quantum point contact in the quantum Hall regime *Phys. Rev. Lett.* **107** 036602

[351] Zimmermann K, Jordan A, Gay F, Watanabe K, Taniguchi T, Han Z, Bouchiat V, Sellier H and Sacépé B 2017 Tunable transmission of quantum Hall edge channels with full degeneracy lifting in split-gated graphene devices *Nat. Commun.* **8** 1–7

[352] Cohen L A, Samuelson N L, Wang T, Klocke K, Reeves C C, Taniguchi T, Watanabe K, Vijay S, Zaletel M P and Young A F 2023 Nanoscale electrostatic control in ultraclean van der Waals heterostructures by local anodic oxidation of graphite gates *Nat. Phys.* **19** 1502–8

[353] Liu X, Farahi G, Chiu C L, Papic Z, Watanabe K, Taniguchi T and Yazdani A 2022 Visualizing broken symmetry and topological defects in a quantum Hall ferromagnet *Science* **375** 321–6

[354] Ahmad N F *et al* 2019 Effect of gap width on electron transport through quantum point contact in hBN/graphene/hBN in the quantum Hall regime *Appl. Phys. Lett.* **114** 023101

[355] Ronen Y *et al* 2021 Aharonov–bohm effect in graphene-based Fabry–Pérot quantum Hall interferometers *Nat. Nanotechnol.* **16** 563–9

[356] Cohen L A, Samuelson N L, Wang T Taniguchi T, Watanabe K, Zaletel M P and Young A F 2023 universal chiral Luttinger liquid behavior in a graphene fractional quantum Hall point contact *Science* **382** 542–7

[357] Li J, Wen H, Watanabe K, Taniguchi T and Zhu J 2018 Gate-controlled transmission of quantum Hall edge states in bilayer graphene *Phys. Rev. Lett.* **120** 057701

[358] Déprez C, Veyrat L, Vignaud H, Nayak G, Watanabe K, Taniguchi T, Gay F, Sellier H and Sacépé B 2021 A tunable Fabry–Pérot quantum Hall interferometer in graphene *Nat. Nanotechnol.* **16** 555–62

[359] Biswas S, Bhattacharyya R, Kundu H K, Das A, Heiblum M, Umansky V, Goldstein M and Gefen Y 2022 Shot noise does not always provide the quasiparticle charge *Nat. Phys.* **18** 1476–81
[360] Nakamura J, Liang S, Gardner G C and Manfra M J 2023 Half-integer conductance plateau at the $\nu = 2/3$ fractional quantum Hall state in a quantum point contact *Phys. Rev. Lett.* **130** 076205
[361] Schiller N, Oreg Y and Snizhko K 2022 Extracting the scaling dimension of quantum Hall quasiparticles from current correlations *Phys. Rev.* B **105** 165150
[362] Zhao L, Arnault E G, Larson T F, Iftikhar Z, Seredinski A, Fleming T, Watanabe K, Taniguchi T, Amet F and Finkelstein G 2022 Graphene-based quantum hall interferometer with self-aligned side gates *Nano Lett.* **22** 9645–51
[363] Feldman D E and Halperin B I 2021 Fractional charge and fractional statistics in the quantum Hall effects *Rep. Prog. Phys.* **84** 076501
[364] Halperin B I, Stern A, Neder I and Rosenow B 2011 Theory of the Fabry-Perot quantum Hall interferometer *Phys. Rev.* B **83** 155440
[365] Van Wees B, Kouwenhoven L P, Harmans C, Williamson J, Timmering C, Broekaart M, Foxon C and Harris J 1989 Observation of zero-dimensional states in a one-dimensional electron interferometer *Phys. Rev. Lett.* **62** 2523
[366] Ofek N, Bid A, Heiblum M, Stern A, Umansky V and Mahalu D 2010 Role of interactions in an electronic Fabry–Perot interferometer operating in the quantum Hall effect regime *Proc. Natl Acad. Sci.* **107** 5276–81
[367] McClure D, Chang W, Marcus C M, Pfeiffer L and West K 2012 Fabry-Perot interferometry with fractional charges *Phys. Rev. Lett.* **108** 256804
[368] Sivan I, Bhattacharyya R, Choi H, Heiblum M, Feldman D Mahalu D and Umansky V 2018 Interaction-induced interference in the integer quantum Hall effect *Phys. Rev.* B **97** 125405
[369] Nakamura J, Fallahi S, Sahasrabudhe H, Rahman R, Liang S, Gardner G C and Manfra M J 2019 Aharonov–Bohm interference of fractional quantum Hall edge modes *Nat. Phys.* **15** 563–9
[370] Choi H, Sivan I, Rosenblatt A, Heiblum M, Umansky V and Mahalu D 2015 Robust electron pairing in the integer quantum Hall effect regime *Nat. Commun.* **6** 7435
[371] Nakamura J, Liang S, Gardner G C and Manfra M J 2023 Fabry-Perot interferometry at the $\nu = 2/5$ fractional quantum Hall state *Phys. Rev.* X **13** 041012
[372] de C Chamon C, Freed D E, Kivelson S A, Sondhi S L and Wen X G 1997 Two point-contact interferometer for quantum Hall systems *Phys. Rev.* B **55** 2331–43
[373] Li J, Tan C, Chen S, Zeng Y, Taniguchi T, Watanabe K, Hone J and Dean C 2017 Even-denominator fractional quantum Hall states in bilayer graphene *Science* **358** 648–52
[374] Werkmeister T et al 2023 Strongly coupled edge states in a graphene quantum Hall interferometer (arXiv:2312.03150)
[375] Yang W et al 2023 Evidence for correlated electron pairs and triplets in quantum hall interferometers (arXiv:2312.14767)
[376] Biswas S, Kundu H K, Umansky V and Heiblum M 2023 Electron Pairing of Interfering Interface-Based Edge Modes *Phys. Rev. Lett.* **131** 096302
[377] Frigeri G A and Rosenow B 2020 Electron pairing in the quantum Hall regime due to neutralon exchange *Phys. Rev. Res.* **2** 043396
[378] Blumenthal M D, Kaestner B, Li L, Giblin S, Janssen T, Pepper M, Anderson D, Jones G and Ritchie D 2007 Gigahertz quantized charge pumping *Nat. Phys.* **3** 343–7
[379] Yamahata G, Ryu S, Johnson N, Sim H-S, Fujiwara A and Kataoka M 2019 Picosecond coherent electron motion in a silicon single-electron source *Nat. Nanotechnol.* **14** 1019–23
[380] Wang J *et al* 2023 Coulomb-mediated antibunching of an electron pair surfing on sound *Nat. Nanotechnol.* **18** 1–6
[381] Fletcher J, Park W, Ryu S, See P, Griffiths J, Jones G, Farrer I, Ritchie D, Sim H-S and Kataoka M 2023 Time-resolved coulomb collision of single electrons *Nat. Nanotechnol.* **18** 1–6
[382] Ubbelohde N *et al* 2023 Two electrons interacting at a mesoscopic beam splitter *Nat. Nanotechnol.* **18** 1–8
[383] Edlbauer H *et al* 2022 Semiconductor-based electron flying qubits: review on recent progress accelerated by numerical modelling *EPJ Quantum Technol.* **9** 21